Dissertation
submitted to the
Combined Faculties for the Natural Sciences and for Mathematics
of the Ruperto-Carola University of Heidelberg, Germany
for the degree of
Doctor of Natural Sciences

presented by

Huayu Hu
born in Sichuan, China

Oral examination: April 27$^{\text{th}}$, 2011

Multi-photon creation and single-photon annihilation of electron-positron pairs

Referees: **PD. Dr. Dr. Carsten Müller**
Prof. Dr. Hans-Jürgen Pirner

Zusammenfassung

In dieser Arbeit werden die quantenelektrodynamischen Prozesse der e^+e^- Paarerzeugung durch Multiphotonen-Absorption und der e^+e^- Annihilierung in ein einzelnes Photon untersucht. Die Paarproduktion erfolgt in der Kollision eines relativistischen Elektrons mit einem intensiven Laserstrahl und wird im Rahmen der Quantenelektrodynamik in externen Laserfeldern beschrieben. Für die in diesem Prozess auftretenden Resonanzen wird auf systematische Weise eine Regularisierungsmethode entwickelt. Wir berechnen totale Produktionsraten, Positronenspektren und die relativen Beiträge der relevanten Reaktionskanäle in verschiedenen Wechselwirkungsbereichen. Unsere Ergebnisse stimmen gut mit vorliegenden experimentellen Daten vom SLAC überein und erlauben eine tiefergehende Interpretation der Messergebnisse. Außerdem untersuchen wir den Paarproduktionsprozess in einem manifest nichtperturbativen Regime, welches in zukünftigen Experimenten auf der Basis von Laserbeschleunigung realisiert werden könnte.

Die e^+e^- Annihilierung in ein einzelnes Photon geschieht in Anwesenheit eines zweiten Zuschauer-Elektrons, das den Rückstoß aufnimmt. Verschiedene kinematische Konfigurationen der drei Teilchen im Anfangszustand werden detailliert untersucht. Unter bestimmten Bedingungen besitzt das emittierte Photon charakteristische Winkelverteilungen und Polarisationseigenschaften, welche die Beobachtung des Effekts erleichtern können. Für ein relativistisches e^+e^- Plasma im thermischen Gleichgewicht zeigen wir, dass die Zerstrahlung in ein Photon bei Plasma-Temperaturen oberhalb 3 MeV zu dominieren beginnt. Derartige Mehrteilchen-Korrelationseffekte sind somit für die Dynamik sehr dichter e^+e^- Plasmen von wesentlicher Bedeutung.

Abstract

In this thesis we study multi-photon e^+e^- pair production in a trident process, and single-photon e^+e^- pair annihilation in a triple interaction. The pair production is considered in the collision of a relativistic electron with a strong laser beam, and calculated within the theory of laser-dressed quantum electrodynamics. A regularization method is developed systematically for the resonance problem arising in the multi-photon process. Total production rates, positron spectra, and relative contributions of different reaction channels are obtained in various interaction regimes. Our calculation shows good agreement with existing experimental data from SLAC, and adds further insights into the experimental findings. Besides, we study the process in a manifestly nonperturbative domain, whose accessibility to future all-optical experiments based on laser acceleration is shown.

In the single-photon e^+e^- pair annihilation, the recoil momentum is absorbed by a spectator particle. Various kinematic configurations of the three incoming particles are examined. Under certain conditions, the emitted photon exhibits distinct angular and polarization distributions which could facilitate the detection of the process. Considering an equilibrium relativistic e^+e^- plasma, it is found that the single-photon process becomes the dominant annihilation channel for plasma temperatures above 3 MeV. Multi-particle correlation effects are therefore essential for the e^+e^- dynamics at very high density.

In connection with the work on this thesis, the following article was published in a refereed journal:

- H. Hu, C. Müller, and C. H. Keitel: *Complete QED theory of multiphoton trident pair production in strong laser fields.* Phys. Rev. Lett. **105**, 080401 (2010).

Articles in preparation:

- H. Hu, C. Müller, and C. H. Keitel: *Strong-field trident pair production in high-energy electron-laser collisions.*
- H. Hu, C. Müller: *Single-photon annihilation in dense electron-positron plasmas.*
- H. Hu, C. Müller, and Jianmin Yuan: *Higher-order QED processes in a dense electron-positron plasma.*

Unrefereed publication:

- H. Hu, M. Ruf, S. Müller, E. Lötstedt, A. Di Piazza, K. Z. Hatsagortsyan, C. Müller, and C. H. Keitel: *Electron-positron pair production in very intense laser fields.* contribution to the annual report 2009/10 of the MPIK.

Contents

Chapter 1

Introduction

Quantum mechanics started with the investigation of photon-electron interactions. To understand the emission and absorption spectra of the atoms, it was found that the atomic electron can be described as a wave-function governed by the Schrödinger equation, named after its inventor [1]. Not only the particle-wave duality, but also the non-commutative operations, first pointed out by Heisenberg [2], gave the theory a novel look from everyday experiences. In the 1930s, the relativistic wave equation as a Lorentz invariant generalization of the Schrödinger equation was discovered by Dirac [3]. The theory has obtained great achievements in explaining our world, and is the foundation of many research fields, such as atomic and molecular physics, solid state physics, physical chemistry, and so on.

Successful though the theory is, a tiny shift in the spectrum of the hydrogen atom—bearing the name of Lamb who first measured it [4]—heralded the discovery of a whole new landscape of modern quantum electrodynamics (QED). Charged particles, such as electrons and muons, are described in a unified way with photons in the language of fields. And their interactions are associated with the generation and annihilation of virtual particles or photons. It is the interaction of the hydrogen electron with the virtual particle and anti-particle pairs instantaneously appearing in the vacuum that results in the energy split between the $2s_{\frac{1}{2}}$ and $2p_{\frac{1}{2}}$ levels. Finalized by Feynman, Tomonaga and Schwinger in the 1950s, QED is one of the most precise theories ever, achieving agreement with experiments with up to 12 significant figures [5].

For the analytically solvable examples given in text books, the particle-photon interaction is usually addressed in a perturbation scheme. For example, in the (relativistic) wave equation of an atom in a weak electromagnetic field, the interaction results in perturbative shifts of the energy levels and distortion of the original wave-functions, while the whole structure of the atomic levels maintains. In ordinary QED, the photon field is assumed to be weak so that only the first term in the perturbation series of the amplitude needs to be kept. The next-order term is expected to be smaller by the order of the expansion parameter, that is the fine-structure constant $\alpha \approx \frac{1}{137.036}$. For example, in studying the scattering of a free electron in a photon field, known as Compton scattering, the one-photon channel plays the dominant role.

Naturally, one would like to ask what happens if a strong electromagnetic field is applied.

A prominent prediction of QED is that real particle and anti-particle pairs can be produced in very intense fields. The first studied by Sauter [6] in 1931 is the electron-positron pair as the lightest massive fundamental particles. In 1951, Schwinger derived the electron-positron pair production rate in a static electric field [7], and introduced the concept of critical electric field

$$E_c = \frac{m^2c^3}{e\hbar} \approx 1.3 \times 10^{16}\, V/cm\,, \tag{1.1}$$

where c is the speed of light in vacuum, $\hbar$ is the reduced Planck constant, m and e are the electron's mass and absolute value of charge, respectively. It corresponds to the field intensity $I_c \approx 2.3 \times 10^{29}\,\mathrm{W/cm^2}$. The amount of work exerted on an electron by the electric force eE_c over a Compton wavelength $\frac{\hbar}{mc}$ is mc^2, just enough to produce a positron at rest, intuitively speaking. The rate of electron-positron pair production in an electric field E is

$$R \propto \exp\left[-\pi\frac{E_c}{E}\right]. \tag{1.2}$$

E_c sets the natural scale, above which the vacuum becomes instable and spontaneously decays into real electron-positron pairs. It is interesting to mention that such an effect of strong fields was also encountered in 1929 in the form of the Klein paradox [8] in the calculation of electron scattering from a potential barrier using the Dirac equation. Contrary to the familiar case that the electron tunnels into the barrier with exponential damping, Klein found that if the potential height is on the order of the electron rest energy, $eV \sim mc^2$, the barrier is nearly transparent and becomes completely transparent when the potential approaches infinity. Today this is explained as the electron-positron pair production at the threshold of the barrier [9].

Besides the theoreticians' interests, a significant stimulus from the experimental side has been provided by the invention of the laser in 1960. With the favorable features like monochromaticity, coherence and high luminosity, it has become an indispensable part of nearly every physics laboratory. Further technological breakthroughs, for example, the chirp-pulse amplification (CPA) [10] in the late 1980s, have paved the way to ultra-short, ultra-intense laser pulses. Nowadays it is not difficult to get access to a table-top laser device producing $10^{18}\,\mathrm{W/cm^2}$ radiation, which is two orders of magnitude stronger than the internal electric field in a hydrogen atom. A variety of nonlinear and multi-photon processes were discovered in atomic and molecular physics, such as high-order harmonic generation [11], non-sequential and above threshold ionization [12], and so on. Based on these studies, coherent light pulses of attosecond duration ($\sim 10^{-18}\,\mathrm{s}$) can be produced [13] as one application, which attracts intense research efforts, since the time scale allows to probe the electron movement inside atoms and molecules. At even higher intensities, nuclear reactions [14] and QED effects [15] can be observed.

The parameters of some state-of-the-art and near-future laser systems are listed in Table 1.1. For optical lasers, a record intensity of $I \approx 2 \times 10^{22}\,\mathrm{W/cm^2}$ has been produced by the Hercules laser at the University of Michigan (Ann Arbor, USA) [16]. HiPER [17] and ELI [18] are two pan-European projects to establish large-scale laser research facilities. They are aimed to deliver ns and even shorter pulses of kJ-scale energy at multi-Hz repetition rates. The laser intensity level of $10^{25} \sim 10^{26}\,\mathrm{W/cm^2}$ is achievable if the beam is focused to a spot with radius $\sim 1\,\mu$m. In addition, there is a new trend towards

higher laser frequencies. Free-electron laser (FEL) technology produces coherent photon sources at VUV frequencies ($\hbar\omega \sim 10-100\,\mathrm{eV}$) by the FLASH facility at DESY (Hamburg, Germany) [19], and 10 keV laser radiation with peak intensity on the order of $10^{20}\,\mathrm{W/cm^2}$ is the aim of X-ray free electron lasers (XFEL) being improved at DESY (as an upgrade of the FLASH beamline) and SLAC (Stanford, USA). The Linac Coherent Light Source (LCLS at SLAC) has recently been commissioned [20]. Currently it produces 1-keV radiation with up to $10^{18}\,\mathrm{W/cm^2}$ intensity. Besides these large-scale facilities, table-top XFEL devices aiming at comparable operation parameters are under development at MPQ (Garching, Germany) [21], by taking advantage of the high quality of the laser-accelerated electron beam.

Table 1.1: Parameters of intense laser facilities.

Facility	Frequency domain [eV]	Maximum intensity [W/cm^2]	ξ	Availability
Hercules	$\sim$1	10^{22}	~ 70	operational
HiPER, ELI	$\sim$1	$10^{25} - 10^{26}$	$\sim 2000 - 7000$	~ 2020
FLASH	$\sim 10 - 10^2$	10^{16}	$\sim 0.001 - 0.01$	operational
LCLS & European XFEL	$\sim 10^3 - 10^4$	10^{20}	$\sim 0.001 - 0.01$	operational

In table 1.1 we have introduced a dimensionless intensity parameter ξ, defined as

$$\xi = \frac{e\bar{A}}{mc^2}\,, \tag{1.3}$$

where $\bar{A}$ is the root-mean-square value of the vector potential of the laser field. ξ measures the strength of the electron-laser interaction and plays the role of an expansion parameter in a perturbation series with respect to the external photon field. As a result, the probability for an n-photon process generally scales as ξ^{2n} in the perturbative domain. If $\xi \gtrsim 1$, however, as is the case in modern intense laser fields, the perturbative expansion method would break down and the laser-matter coupling becomes manifestly nonperturbative.

The modification of the perturbative QED in strong electromagnetic fields was initiated soon after the invention of the laser, leading to the theory of laser-dressed QED, also known as strong-field QED. The creation of electron-positron pairs in very strong laser fields was investigated by theoreticians already in the 1960s and 1970s. They studied pair creation by a high-energy non-laser photon propagating in a strong laser field [22, 23], by a nuclear Coulomb field in the presence of a strong laser field [24], and by two counterpropagating laser beams forming a standing light wave [25, 26]. In all cases an additional field is required to induce the pair creation, because a single electromagnetic plane wave cannot extract pairs from the QED vacuum [7], due to energy-momentum conservation constraints. However, the strong-field QED effects could not be verified experimentally at that time, since the laser intensity available was too low compared to the critical value I_c.

The interest in laser-induced pair creation processes has been strongly revived in recent years due to the ongoing increase in the available laser intensities and, particularly,

due to the experiment E-144 performed at SLAC [27] which for the first time provided the laboratory proof of multi-photon particle anti-particle pair production. There the electron-positron pairs were produced by bombarding a nearly 50 GeV electron beam with a counter-propagating $10^{18}\,\mathrm{W/cm^2}$ optical laser pulse. The pairs were produced via the reaction chain

$$e + n\omega \to e' + n'\omega + \gamma \to e' + e^+e^- \,, \tag{1.4}$$

where a two-step process was formed: first the generation of a γ photon via multi-photon Compton scattering, and then the electron-positron pair production via the scattering of the γ photon and laser photons. It is a strong-field version [22, 23] of the Breit-Wheeler process [28]. In this sense, it is also the first experiment displaying inelastic light-by-light scattering involving real photons. In the experiment the laser intensity is Doppler-enhanced in the rest frame of the colliding electron by a factor of $(2\gamma)^2$ with $\gamma \approx 10^5$, to $\sim 10^{28}\,\mathrm{W/cm^2}$, this way approaching the critical value I_c. It is worthy to mention that the pair production can also be realized via a competing process

$$e + n\omega \to e' + e^+e^- \,, \tag{1.5}$$

where the pairs are produced in a direct manner with the intermediate photon staying off-shell. It is a reaction of Bethe-Heitler type [29] in strong fields.

In the SLAC experiment, the laser photons participated directly in the production of the pair. Besides, prolific electron-positron pairs can also be produced with the strong laser playing an indirect role. If shooting a strong laser pulse at a solid target, a plasma can be formed in which the laser-produced hot electrons can generate high-energy bremsstrahlung photons. These photons have a probability to interact with the nuclei and convert to electron-positron pairs. The present record is $10^{16}\mathrm{cm^{-3}}$ positron density [30] by using $\sim 10^{20}\mathrm{W/cm^2}$ laser. Higher densities are proposed with the application of more intense lasers [31]. The high-density electron-positron plasmas have special interests in astrophysics [32], electron-positron γ-ray source [33], electron-positron Bose-Einstein condensates [34], and so on. As the density increases, the multi-particle correlation effects can become prominent. An example is the single-photon triple annihilation

$$e^+e^- + e \to e' + \gamma \,. \tag{1.6}$$

Here a single photon is produced by electron-positron annihilation, with the recoiled momentum (virtual photon) absorbed by a nearby electron (positron). Such higher-order processes may be significant in the dynamics of high-density electron-positron plasmas.

Structure of the thesis and main results

In this thesis, we investigate the nonperturbative nonlinear QED effect of multi-photon trident electron-positron pair production in strong laser fields, and the related topic of single-photon pair annihilation in high-density electron-positron samples. For the nonperturbative treatment of the pair production, the theories of Volkov states and laser-dressed QED are described in **chapter 2**, showing how the ordinary QED is modified to include the laser-particle interaction to all-orders. In **chapter 3**, a unified theory of multi-photon

pair production is developed, treating the various pair production channels—(1.4) and (1.5)— on the same footing. Special emphasis is placed on the technique of dealing with the resonances. The resonance problem, which takes place when an intermediate particle (photon) goes on shell, is generally encountered in multi-photon processes. The detailed analytical derivations are given in Appendices C, D, and E. Complete nonperturbative QED calculations are performed from the few-photon perturbative regime to the quasi-static regime, where hundreds of laser photons are involved. Appendix A gives the threshold condition for the pair production process to take place, and Appendix B provides the detailed information on the implementation of the calculation. **Chapter 4** presents the theory and numerical calculations for the single-photon electron-positron annihilation (1.6). Interesting features are identified in the polarization and angular distribution of the emitted photon, as the kinetic parameters of the three incoming particles are examined carefully. Finally, the total single-photon annihilation rate is calculated for equilibrium high-density relativistic plasmas, and comparisons are drawn with the more well-known two-photon annihilation process ($e^+e^- \to \gamma' + \gamma$). The relevant calculation techniques are presented in Appendix F.

Our theory explains the results of the SLAC E-144 experiment very well. The power law dependence with ξ^{10} of the total pair production rate is obtained and the measured positron momentum spectrum is reproduced. Our calculations moreover allow us to obtain further insights into the experimental results. We show that an average ~ 6.4 photons participate in the process and demonstrate that the experiment observed the onset of nonperturbative signatures. Furthermore, in view of future experimental studies, a parameter range is determined in which the direct process (1.5) dominates, and the experimental verification can be made by combining the relativistic electrons from an XFEL beamline and a VUV laser pulse. It is shown that future experiments of electron-positron pair production can also be realized by all-optical setups, with the high-energy electron produced by laser acceleration.

As substantial efforts are devoted to increase the density of electron-positron plasmas available in the lab, we identify the temperature of an equilibrium electron-positron plasma, above which the single-photon annihilation overrides the usual two-photon process. Also, the distinctive features of the radiation found in special parameter regimes can benefit the designs of the experiments.

Notation and conventions

Relativistic units with $\hbar = c = 1$ are used through the thesis. The electron mass is $m = 0.511\,\mathrm{MeV}$. The relation $e = \sqrt{\alpha}$ of the Gaussian system is adopted as the absolute value of electron charge. The metric used is

$$g^{\mu\nu} = \begin{pmatrix} 1 & 0 & 0 & 0 \\ 0 & -1 & 0 & 0 \\ 0 & 0 & -1 & 0 \\ 0 & 0 & 0 & -1 \end{pmatrix}, \tag{1.7}$$

and the four-vector product is $a \cdot b = a^\mu b_\mu = a^0 b^0 - \mathbf{a} \cdot \mathbf{b}$. The 'slash' is used to denote

$$\not{a} = \gamma^\mu a_\mu \,,$$

where γ^μ is the Dirac representation of gamma matrices. The bar-conjugated spinor and matrix are defined as

$$\bar{\Psi} = \Psi^\dagger \gamma^0 \,, \tag{1.8}$$

and

$$\bar{\Gamma} = \gamma^0 \Gamma^\dagger \gamma^0 \,. \tag{1.9}$$

Chapter 2

Volkov states and laser-dressed QED

2.1 Introduction to intense laser-matter interactions

Quantum electrodynamics (QED) is one of the most accurate theories possessing a high consistency between the experimental measurements and the theoretical calculations. In the ordinary QED approach, a particle state is represented by a plane wave, and the coupling of a particle and an electromagnetic field is taken into account in a perturbative way. This treatment works remarkably well when the particle-light interaction is weak, so that the perturbation method can be applied properly.

The situation changes in high-intensity laser fields already accessible nowadays, noting that modern state-of-the-art laser systems can achieve $\sim 10^{22}\,\mathrm{W/cm^2}$ field intensity [16]. A charged particle like an electron is driven into oscillations by the electromagnetic force of the laser field, and acquires a mean kinetic energy known as ponderomotive energy [35]

$$U_p = \frac{\pi e^2 I}{m\omega^2}\,, \tag{2.1}$$

where I and ω are the field intensity and frequency. In high-intensity laser fields, this energy absorbed from the laser field can be very large, $U_p \gtrsim m$. It indicates that the particle-photon interaction can not be considered small anymore, and the perturbative QED method needs modification.

Previous work in atomic and molecular physics regarding strong field problems has proposed a powerful idea for dealing with the non-perturbative interactions [36]. The idea is to absorb the coupling term of the strong external field into the free particle's Hamiltonian, and based on the eigenstates of the new Hamiltonian, solve the Schrödinger equation whose remaining interaction Hamiltonian now includes weak perturbations only. By this means, the perturbative approach with respect to the weak interactions retrieves the feasibility, with the new eigenstates containing all the information of the non-perturbative interaction.

Similar ideas have been developed for strong-field QED or laser-dressed QED, since a strong laser field is often in concern. The eigenstates known as Volkov states [37, 38]

of an electron (positron) in a plane electromagnetic wave are applied. As the free particle state is dressed by the external field, this approach is more generally known as a Furry picture [39]. The properties of the Volkov states are shown in section 2.2. In section 2.3 some characteristics of laser-dressed QED are discussed. This method has been used generally in studying many QED processes with strong laser field involved, such as laser-dressed Compton scattering [23, 38, 40], laser-dressed Møller scattering [41, 42], laser-dressed bremsstrahlung [43, 44], and so on.

Several dimensionless Lorentz-invariant parameters [45] are often encountered in laser-dressed QED. The first has been mentioned in table 1.1:

$$\xi = \frac{e\sqrt{-\langle A_\mu A^\mu \rangle}}{m} = \frac{e\bar{E}}{m\omega}\,, \tag{2.2}$$

where A is the four-vector potential of the laser field, $\bar{E}$ is the root-mean-square value of the electric field component, ω is the laser photon energy, and $\langle\,\rangle$ represents time averaging. ξ characterizes the work, referred to the electron rest energy, that the laser field exerts to a particle over a wavelength. It is related to the probability of the multi-photon effects. The higher ξ is, the more laser photons participate in a process. If an electron with momentum p is under study, another parameter is

$$\chi = \frac{e\sqrt{-\langle (F_{\mu\nu}p_\nu)^2 \rangle}}{m^3} = \gamma(1+\beta)\frac{\bar{E}}{E_c} = \xi\frac{\omega_b}{m}\,, \tag{2.3}$$

where $F_{\mu\nu}$ is the electromagnetic field tensor of the laser, E_c is the critical field given by Eq. (1.1), and $\omega_b = \gamma(1+\beta)\omega$ is the photon energy in the rest frame of the electron. The last two expressions are derived assuming the electron collides with the laser head-on with $\gamma = \frac{p^0}{m}$ and $\beta = \frac{|\mathbf{p}|}{p^0}$. The parameter χ describes the ratio of the energy that a particle absorbs from the laser field along a Compton wavelength over the electron rest energy. It is found to be responsible for the quantum nonlinear effects [45]. When $\chi \sim 1$, the electric field strength in the electron rest frame is of the order of the critical value E_c. If the colliding particle is a photon with momentum k', a similar parameter is

$$\kappa = \frac{e\sqrt{-\langle (F_{\mu\nu}k'_\nu)^2 \rangle}}{m^3} = 2\frac{\omega'}{m}\frac{\bar{E}}{E_{cr}}\,, \tag{2.4}$$

with $\omega' = k'^0$ being the colliding photon's energy. The equation is again valid when a head-on collision is assumed. As will be addressed in section 2.3, κ is responsible for the magnitude of radiative corrections to the photon propagator in a laser field.

2.2 Volkov states

The exact solutions of the Dirac equation of a free electron or positron in a plane electromagnetic wave were obtained in [37, 38]. The four-vector potential of a plane-wave field can in general be written as $A(k\cdot x)$ with $k^2 = 0$. In the following the gauge is chosen so that $k \cdot A = 0$. Despite the requirement of a unique propagation direction of

the electromagnetic wave, there is still large room for the possible forms the field can take with arbitrary compositions of the frequency and polarization of the components.

The Dirac equation of an electron or a positron in an external laser field is

$$(\gamma^\mu(\hat{p}_\mu - eA_\mu) - m)\Psi = 0\,, \tag{2.5}$$

with the initial condition for an electron

$$\Psi(x) \sim e^{-ip_-\cdot x}u_{p_-,s_-}\ \text{, as } x^0 \to -\infty\,,$$

and the initial condition for a positron

$$\Psi(x) \sim e^{ip_+\cdot x}u_{p_+,s_+}\ \text{, as } x^0 \to -\infty\,,$$

where $u_{p_\pm,s_\pm}$ is the free Dirac spinor. The solution of Eq. (2.5) is given by [38]

$$\Psi_{p_\pm,s_\pm}(x) = \sqrt{\frac{m}{q_\pm^0 V}}(1 \pm \frac{e\not{k}\not{A}}{2k\cdot p_\pm})u_{p_\pm,s_\pm}e^{if_\pm(x)}\,, \tag{2.6}$$

where $_\pm$ corresponds to the particle being an electron($_-$) or a positron ($_+$) respectively, which we will refer to in the following only if ambiguity could arise otherwise, V is the normalization volume, $q_\pm^0$ is the time-averaged energy of the particle in the field which will be explained below, and the phase term is

$$f_\pm(x) = \pm p_\pm\cdot x - \int_{-\infty}^{y} dy' \frac{1}{2k\cdot p_\pm}(2ep_\pm\cdot A(y') \pm e^2A^2(y'))\,, \tag{2.7}$$

with the denotation $y = k\cdot x$ in the integral. Usually in Eq. (2.7), a time-averaged term can be extracted from the integration, and thus

$$\begin{aligned} f_\pm(x) &= \pm\,(p_\pm + \frac{e^2\langle -A^2\rangle}{2k\cdot p_\pm}k)\cdot x - \int_{-\infty}^{y} dy' \frac{1}{2k\cdot p_\pm}[2ep_\pm\cdot A(y') \pm e^2(A^2(y') - \langle A^2\rangle)] \\ &= \pm\, q_\pm\cdot x - \int_{-\infty}^{y} dy' \frac{1}{2k\cdot p_\pm}[2ep_\pm\cdot A(y') \pm e^2(A^2(y') - \langle A^2\rangle)]\,. \end{aligned} \tag{2.8}$$

The quantity

$$q_\pm = p_\pm + \frac{e^2\langle -A^2\rangle}{2k\cdot p_\pm}k \tag{2.9}$$

possesses the physical meaning of the time-averaged momentum of the particle oscillating in the plane-wave field. This claim can be strictly proven, see Appendix C of [38]. Therefore, $q_\pm^0 = p_\pm^0 + \frac{e^2\langle -A^2\rangle}{2k\cdot p_\pm}k^0$ in Eq. (2.6) leads to the normalization condition for the wave function of a particle submitted to a field as

$$\int d^3x \Psi^\dagger_{q,s}(x)\Psi_{q',s'}(x) = (2\pi)^3\delta(\mathbf{q}-\mathbf{q}')\delta_{ss'}\,. \tag{2.10}$$

A general feature of the laser-dressed particle is a heavier effective mass $m_*^2 = q_\pm^2 = m^2(1+\xi^2)$ with ξ given by Eq. (2.2). In a strong laser field, the change of the particle mass can be large enough to notably change the kinematic relations.

The four-potential of a monochromatic circularly polarized plane-wave laser field can in general be written as [46]

$$A(x) = a_1 \cos(k \cdot x) + a_2 \sin(k \cdot x)\,, \tag{2.11}$$

where $a_{1,2}$ are constant four-vectors chosen as $a_1 = (0, a, 0, 0)$ and $a_2 = (0, 0, a, 0)$, with a denoting the amplitude of the vector potential, and the wave four-vector k can be chosen as $k = \omega(1, 0, 0, 1)$. The integration in Eq. (2.8) can be carried out as

$$f_\pm = \pm q_\pm \cdot x + \frac{e p_\pm \cdot a_1}{k \cdot p_\pm} \sin(k \cdot x) - \frac{e p_\pm \cdot a_2}{k \cdot p_\pm} \cos(k \cdot x)\,, \tag{2.12}$$

with

$$q_\pm = p_\pm + \frac{e^2 a^2}{2 k \cdot p_\pm} k\,. \tag{2.13}$$

For a monochromatic linearly polarized plane-wave laser field, the four-potential can in general be written as [47]

$$A(x) = \epsilon a \cos(k \cdot x)\,, \tag{2.14}$$

where a indicates the amplitude of the vector potential, the polarization is chosen as $\epsilon = (0, 1, 0, 0)$, and the wave four-vector is chosen to be $k = \omega(1, 0, 0, 1)$. In this case,

$$f_\pm = \pm q_\pm \cdot x + \frac{e a \epsilon \cdot p_\pm}{k \cdot p_\pm} \sin(k \cdot x) \pm \frac{e^2 a^2}{8 k \cdot p_\pm} \sin(2 k \cdot x)\,, \tag{2.15}$$

with

$$q_\pm = p_\pm + \frac{e^2 a^2}{4 k \cdot p_\pm} k\,. \tag{2.16}$$

Since in this thesis we mainly consider the particle interacting with linearly polarized fields, it is worthy to take a closer look at the Volkov solutions in this case. The oscillating part of the phase term of the Volkov state as shown in Eq. (2.15) can be decomposed into a sum in form of a Fourier series with the coefficients being the generalized Bessel functions [38, 45]. Therefore, the Volkov state is transformed to be

$$\begin{aligned}
\Psi_{p_\pm, s_\pm} =& \sqrt{\frac{m_e}{q_\pm^0 V}} \Big(1 \pm \frac{e \not{k} \not{A}}{2 k \cdot p_\pm}\Big) u_{p_\pm, s_\pm} e^{\pm i q_\pm \cdot x} \sum_{n=-\infty}^{\infty} J_n\Big(\frac{e a \epsilon \cdot p_\pm}{k \cdot p_\pm}, \mp \frac{e^2 a^2}{8 k \cdot p_\pm}\Big) e^{i n k \cdot x} \\
=& \sqrt{\frac{m_e}{q_\pm^0 V}} u_{p_\pm, s_\pm} e^{\pm i q_\pm \cdot x} \sum_{n=-\infty}^{\infty} \Big(B_n(\alpha, \beta) \pm \frac{e a \not{k} \not{\epsilon}}{2 k \cdot p_\pm} C_n(\alpha, \beta)\Big) e^{i n k \cdot x}\,,
\end{aligned} \tag{2.17}$$

with $\alpha = \frac{e a \epsilon \cdot p_\pm}{k \cdot p_\pm}$, $\beta = \mp \frac{e^2 a^2}{8 k \cdot p_\pm}$, $B_n(\alpha, \beta) = J_n(\alpha, \beta)$ and

$$C_n(\alpha, \beta) = \frac{1}{2}\big(J_{n-1}(\alpha, \beta) + J_{n+1}(\alpha, \beta)\big)\,,$$

where the generalized Bessel function $J_n(\alpha, \beta)$ is defined by the integral representation [22, 48]

$$J_n(\alpha, \beta) = \frac{1}{2\pi} \int_{-\pi}^{\pi} \exp[-i n \theta + i \alpha \sin(\theta) - i \beta \sin(2\theta)] d\theta\,.$$

It can also be expressed as an infinite sum over products of ordinary Bessel functions

$$J_n(\alpha,\beta)=\sum_{l=-\infty}^{\infty}J_{n-2l}(\alpha)J_l(\beta)\,.$$

Eq. (2.17) suggests that the Volkov state can be seen as a superposition of infinitely many states of well-defined four-momentum in the form of $q_\pm+nk$, $n\in\mathbb{Z}$. Sometimes it is pictured that a Volkov state occupies a ladder of uniformly spaced energy levels, with the energy difference between subsequent levels being the energy of the laser photon [49]. It has an indicative application in explaining laser-atom interactions, where the high-order harmonic generation is interpreted as Coulomb-field-induced transition between these energy levels [50, 51].

The normalization and orthogonality of the Volkov states are proven, see [38, 45]. Therefore they are well justified to serve as a basis of continuous functions for laser-related problems.

A similar expansion like Eq. (2.17) can be obtained for the case of a circularly polarized plane-wave laser [46], where the Fourier coefficients are ordinary Bessel functions, making it relatively simpler in the calculation.

2.3 Laser-dressed QED

Laser-dressed QED uses Volkov functions instead of plane-wave functions to represent the particles' initial and final states, as well as to construct the particle propagator. In an external plane-wave field $A(k\cdot x)$, the free electron propagator [52]

$$G_{\mathtt{free}}(x_1,x_0)=\frac{1}{(2\pi)^4}\int d^4p\frac{\not p+m}{p^2-m^2+i\epsilon}e^{-ip(x_1-x_0)}\,,$$

is transformed to the so-called Dirac-Volkov propagator $G(x_1,x_0)$ [45], which satisfies

$$(\gamma_\mu(\hat p^\mu-eA^\mu)-m)G(x_1,x_0)=\delta(x_1-x_0)\,.$$

It is found to take the form

$$G(x_1,x_0)=\frac{1}{(2\pi)^4}\int d^4p(1-\frac{e\not k\not A}{2k\cdot p})e^{if(x_1)}\frac{\not p+m}{p^2-m^2+i\epsilon}(1-\frac{e\not A\not k}{2k\cdot p})e^{-if(x_0)}\,,\tag{2.18}$$

where the phase term $f(x)$ is given by Eq. (2.7). For the case of a linearly polarized plane-wave laser field [see Eq. (2.14)], $f(x)$ adopts the form of Eq. (2.15), and $G(x_1,x_0)$ can be expanded by using the generalized Bessel functions

$$\begin{aligned}G(x_1,x_0)=&\frac{1}{(2\pi)^4}\int d^4p\sum_{n,n'}(B_n(\alpha,\beta)-\frac{ea\not k\not\epsilon}{2k\cdot p}C_n(\alpha,\beta))\frac{\not p+m}{p^2-m^2+i\epsilon}\\&\times(B_{n'}(\alpha,\beta)-\frac{ea\not\epsilon\not k}{2k\cdot p}C_{n'}(\alpha,\beta))e^{-iq(x_1-x_0)+ik\cdot(nx_1-n'x_0)}\,,\end{aligned}\tag{2.19}$$

with the denotations as for Eq. (2.17).

In principle the free photon propagator should also be replaced by the full photon propagator, which contains the effects of laser-photon interactions. The lowest order Feynman diagram in the fine-structure constant beyond the free photon propagator is the vacuum polarization, with the laser-dressed electron loop. It has been found [53, 54] that this radiative correction is on the order of $\alpha\,\kappa^{\frac{2}{3}}$ and assigns a complex mass to the photon. For the parameter regime investigated in our study, the following condition is fulfilled

$$\alpha\kappa^{\frac{2}{3}} \sim \alpha(2\frac{\omega'}{m}\frac{E}{E_c})^{\frac{2}{3}} \lesssim \alpha\,. \tag{2.20}$$

Therefore, the free photon propagator is always used as a very good approximation. As will be discussed in section 3.2.3, the radiative corrections can be relevant at the pole of the propagator, where the imaginary mass correction can contribute to regulate the divergence. Nevertheless, it is so small compared to other corrections that it can always be neglected in the cases we consider. However, when $\alpha\,\kappa^{\frac{2}{3}} \sim 1$, the photon mass reaches the same order of magnitude as the electron mass, and perturbation theory in α is not applicable anymore since all orders in the perturbative expansion need to be taken into account [53, 54].

Due to the use of the Volkov states which are the 'overgrown' eigen wave-functions of the particles in the laser field, the theory of laser-dressed QED takes into account to all orders the particle-laser interaction in a scattering process, and still adopts a similar formalism like that of the ordinary QED. The remaining interaction between the laser-dressed particle and the QED vacuum is weak, and the perturbative expansion in the fine-structure constant α is resorted to as in the ordinary QED. Accordingly, Feynman techniques can be used to picturise the theory, and laser-dressed Furry-Feynman diagrams follow almost the same rules of the conventional Feynman diagrams, except that the appearing particles are in Volkov states and the particle propagators are Dirac-Volkov propagators.

In the next chapter, we deal with the multi-photon pair production. We will see there that the power of the laser-dressed QED formalism manifests itself, for example, in Furry-Feynman diagrams which include the information of a large number of corresponding ordinary Feynman diagrams regarding multi-photon absorption, shown in Fig. 3.1.

Chapter 3

Multi-photon trident pair production in intense laser fields

3.1 General remarks on laser-induced pair production

Lepton pair production in external fields has attracted physicists' attention since the dawn of the quantum field theory, and stands out as one of its novel predictions. First studied by Sauter as early as 1931 [6], then reconsidered by Schwinger who derived an exact formula for the probability of pair creation in a static electric field [7], it is predicted that in an intense electric field with the critical field intensity $I_c \sim 10^{29}\,\mathrm{W/cm^2}$ electron-positron pairs would arise spontaneously from the instable vacuum. Substantial theoretical efforts have been devoted to e^+e^- pair creation, taking into account a crossed static field [23], high-Z nuclei [55], or a time-varying electric field [56].

Pair production has also been considered in a trident process in a photon field [57],

$$e + \gamma \to e' + e^+e^- \,, \tag{3.1}$$

where one electron scatters by a colliding photon and emits a virtual photon, which subsequently transforms into an e^+e^- pair. When the photon source is a laser field, the electron may couple nonlinearly to the field, giving rise to multi-photon processes. Theoreticians started to consider multi-photon e^+e^- pair production soon after the invention of the laser [22, 23], as well as other nonlinear QED phenomena such as multi-photon Compton scattering [40], bremsstrahlung [43], and photon splitting [58]. The corresponding experimental observation, however, has long been cumbered by the low probability of the processes due to the difficulty in achieving sufficiently high field intensities.

With remarkable technical breakthroughs, the laser intensity has been tremendously increased since the late 1980s. State-of-the-art intense lasers can nowadays reach an intensity as high as $10^{22}\,\mathrm{W/cm^2}$ [16]. Although the Schwinger limit (I_c) seems still out of reach in the lab frame in the near future, with a smart combination of laser technology and particle accelerator technology, multi-photon e^+e^- pair creation can be observed even by

currently available laser fields. In the mid-1990s pioneering studies at SLAC (Stanford, California) revealed nonlinear QED effects in the E-144 experiment [27]. In particular, the first and so far unique observation of multi-photon pair production was accomplished in collisions of a ≈ 50 GeV electron beam from SLAC's linear accelerator with an intense laser pulse. The laser frequency and field strength were largely Doppler-enhanced in the rest frame of the high energetic projectile, this way approaching the Schwinger limit.

Inspired by the SLAC E-144 experiment several theory groups have considered pair production in highly energetic laser-particle collisions. Motivated by the advent of the powerful ion accelerator LHC at CERN, the focus has mostly been laid on pair creation by relativistic nuclei colliding with intense laser beams. Here the strong-field variant of the Bethe-Heitler process [29] can be probed: $Z + N\omega \to Z + e^+e^-$, with the atomic number Z. It has been investigated in great detail. Total production rates have been calculated in various interaction regimes [59–62]. Energy spectra and angular distributions of the produced particles were obtained [59,61,63,64]. The influence of bound atomic states [65], an additional high-frequency photon [66], and the nuclear recoil [67,68] have been studied as well. Besides, it was also proposed that pair production can take place in counter-propagating laser beams (e.g., [69–74]). Meanwhile, theoreticians are already considering more refined aspects of the process such as final-state pair correlations [75], the influence of the electron spin [76], and the creation of heavier particles such as $\mu^+\mu^-$ pairs [77].

Nevertheless, despite all these efforts, no complete QED calculation of the SLAC E-144 experiment has existed as yet. Until now, the complete theory of strong-field trident pair production was only developed in constant crossed fields [78]. This case corresponds to the low-frequency limit $\omega \to 0$, which does not apply to the SLAC study. In comparison with multi-photon pair creation in laser-proton collisions, the theoretical consideration of laser-electron collisions is more involved in several respects. One needs to take into account (i) the dressing of the projectile electron by the laser field, (ii) the recoil the projectile suffers during the collision, (iii) the indistinguishability of the scattered projectile with the created electron of the pair (Pauli principle), and (iv) the possibility of real photon emission by the projectile in the field (Compton scattering). The inclusion of all these aspects represents a rather challenging task.

In laser-electron collisions, two pair creation processes are usually distinguished. The first is of Bethe-Heitler type [29]; the pair is produced by the absorption of N laser photons in the Coulomb field of the incoming electron:

$$e + N\omega \to e' + e^+e^-. \tag{3.2}$$

The second is a two-step process; first a high-energy γ-photon is generated by Compton backscattering off the electron beam, and afterwards it participates in a photon-multi-photon collision to create the pair (nonlinear Breit-Wheeler process [22, 23]):

$$\gamma + N\omega \to e^+e^-. \tag{3.3}$$

The analysis of SLAC's experimental data [27] relied on separate simulations of both processes and led to the conclusion that the two-step mechanism dominated the pair production by far. However, while for the Breit-Wheeler reaction (3.3) a sophisticated

theory was available [22, 23], the contribution from the Bethe-Heitler process (3.2) was estimated in a rather approximate manner [79,80] since a formal theory did not exist. The applicability of the Weizsäcker-Williams method previously employed conflicts, however, with the large projectile recoil, as noted in [80].

One purpose of our present study is to fill this gap in the theory of strong-field phenomena, since a unified description, covering both the nonlinear Breit-Wheeler channel and nonlinear Bethe-Heitler channel on the same footing, is required for a reliable full investigation of the process under different conditions. This becomes relevant as nonlinear pair creation nowadays is becoming accessible to all-optical setups involving laser acceleration devices.

In this chapter we provide a nonperturbative laser-dressed QED calculation of multi-photon trident pair creation in laser-electron collisions. Our approach treats the Bethe-Heitler and Breit-Wheeler processes in a unified way and opens deeper insights into the SLAC measurements. Furthermore, we evaluate the creation rates in the fully nonperturbative regime which could be probed by future experiments employing upcoming technologies.

Before we continue, it is worth mentioning that lasers can also be applied for abundant generation of e^+e^- pairs [30]. When a solid target is irradiated by an intense laser pulse, a plasma is formed and electrons are accelerated to high energies. They may emit bremsstrahlung which efficiently converts into e^+e^- pairs through the ordinary (single-photon) Bethe-Heitler effect. We stress that the laser field plays an indirect role in the pair production here solely as a particle accelerator. The prolific amounts of antimatter generated this way may allow for interesting applications in various fields of science.

3.2 Theoretical approach to trident pair production

In this section we derive the matrix element and the rate for the pair production in a head-on collision of an electron and a linearly polarized plane-wave laser field. The equivalence between the laser-dressed formalism in the limit of low field intensity and the usual external-field-free QED formalism is given explicitly. We provide a detailed analysis of the resonance problem which arises in the multi-photon pair production process when the intermediate photon gets on-shell. To treat the relevant formally divergent integrals, a regularization method is developed in a systematic way, based on the comparison with the cascade theory, which considers the case that a process is composed of successive sub-processes with the output of the previous step being the input of the next.

The Furry-Feynman diagrams of the trident pair production are shown in Fig. 3.1. For e^+e^- pair production, due to the indistinguishability of the two electrons in the final state, the two diagrams have to be added up coherently to get the total amplitude. The eight Feynman diagrams of the documented single-photon trident pair production are shown in Fig. 3.2, both to give an example of the perturbative expansion of the Furry-Feynman diagrams to the first order in the electron-laser interaction in the weak-field limit, and for their historical significance [57].

3.2.1 Matrix element and production rate for linear polarization

The laser-dressed Furry-Feynman diagrams of multi-photon trident pair creation are depicted in Fig. 3.1. The lepton lines in the Furry-Feynman diagrams are described by Dirac-Volkov states [37, 38] which fully account for their interaction with the external plane-wave laser field (Furry picture).

A linearly polarized laser is considered here, the four-vector potential of which is described in Eq. (2.14). The Dirac-Volkov state in this field is presented in Eq. (2.17), in the Fourier-expanded form with the coefficients being the generalized Bessel functions. As illustrated in section 2.2, a particle with momentum p submitted to this field acquires a laser-dressed mass $m_* = m\sqrt{1+\xi^2}$, and a laser-dressed four-momentum $q = p^\mu + \frac{m^2\xi^2}{2k\cdot p}k^\mu$, where $\xi = \frac{e}{m}\bar{A}$ with the root-mean-square value of the laser vector potential $\bar{A} = a/\sqrt{2}$.

To leading order in the QED fine-structure constant α, the amplitude for the process reads

$$S_{fi} = \mathcal{M}(q, q', q_+, q_-) - \mathcal{M}(q, q_-, q_+, q')\,, \tag{3.4}$$

where

$$\mathcal{M}(q, q', q_+, q_-) = -i\alpha \int d^4x \int d^4y \bar{\Psi}_{q'}(x)\gamma_\mu \Psi_q(x) D^{\mu\nu}(x-y)\bar{\Psi}_{q_-}(y)\gamma_\nu \Psi_{q_+}(y)\,, \tag{3.5}$$

and the exchange term $\mathcal{M}(q, q_-, q_+, q')$ correspond to the left and right diagrams in Fig. 3.1, respectively. Here, $\Psi_q, \Psi_{q'}, \Psi_{q_+}, \Psi_{q_-}$ denote the laser-dressed lepton states and

$$D^{\mu\nu}(x-y) = \int \frac{d^4k'}{(2\pi)^4} \frac{-i4\pi g^{\mu\nu}}{k'^2 + i\epsilon} e^{ik'\cdot(x-y)} \tag{3.6}$$

is the free photon propagator. The infinitely small imaginary part $i\epsilon$ in the denominator of the photon propagator will be dropped for notational simplicity in the following. We will come back to this issue in section 3.2.3. As discussed in section 2.3, the laser-dressed propagator should be used in a more sophisticated treatment in super-intense laser fields when $\alpha\,\kappa^{\frac{2}{3}} \sim 1$. For the numerical results shown in this chapter, the relation $\alpha\,\kappa^{\frac{2}{3}} \lesssim 10^{-2}$ always holds, so that the free photon propagator represents a good approximation.

Substituting the Fourier-expanded form of the Dirac-Volkov states (2.17) into Eq. (3.5), the space-time integrations can be performed. The amplitude adopts the form

$$\begin{aligned}\mathcal{M}(q, q', q_+, q_-) = -\alpha \frac{2(2\pi)^5 m^2}{V^2\sqrt{q^0 q'^0 q_+^0 q_-^0}} \sum_{N\geq N_0} \sum_{n=-\infty}^{\infty} \frac{\delta^{(4)}(q + Nk - q' - q_+ - q_-)}{(q - q' + nk)^2} \\ \times M^\mu(q, q'|n) M_\mu(q_+, q_-|N-n)\,,\end{aligned} \tag{3.7}$$

where N is the total number of photons absorbed, n is the number of photons absorbed at the first vertex (see Fig. 3.1) with a negative n meaning $|n|$ photons emitted, and $M^\mu(q, q'|n)$, $M_\mu(q_+, q_-|N-n)$ are complex functions of the particle momenta and laser

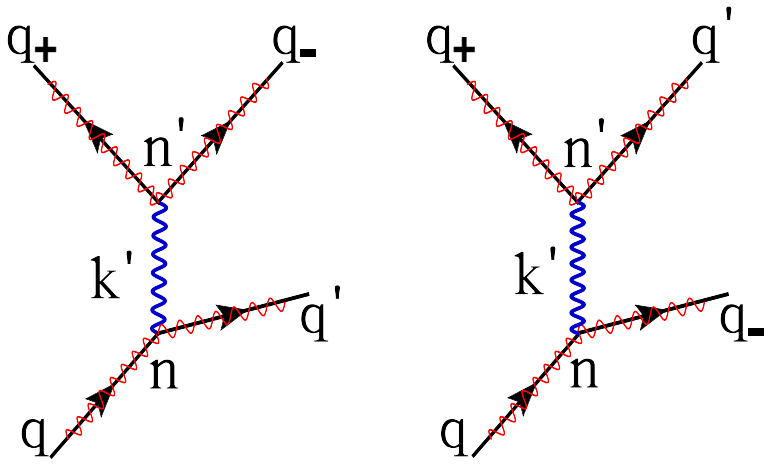

Figure 3.1: Furry-Feynman diagrams of multi-photon trident pair production in electron-laser collisions. The zigzag-lines represent the exact lepton wave-functions in the laser field (Dirac-Volkov states [37]) and are labeled by the laser-dressed particle momenta. In the left diagram, the incoming electron scatters from a state of dressed momentum q to q' by absorbing n laser photons and emitting an intermediate photon, which afterwards decays into an e^+e^- pair upon absorption of n' laser photons. The corresponding exchange diagram is shown on the right. In the weak-field limit ($\xi \ll 1$), the diagrams can be expanded in ordinary Feynman diagrams of external-field-free QED. For a total number of $N = n + n' = 1$ absorbed photons, eight leading-order diagrams arise this way [57], shown in Fig. 3.2. Note that the case $N = 6$ (see section 3.3.1) corresponds to 168 ordinary Feynman diagrams.

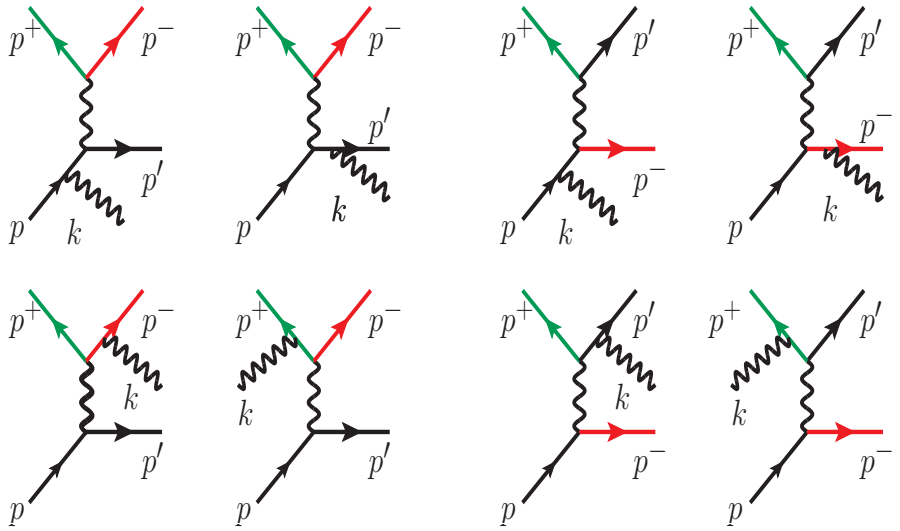

Figure 3.2: Feynman diagrams of trident e^+e^- pair production from the collision of an electron and a photon. The left (right) four diagrams correspond to the lowest order expansion in the laser-electron coupling parameter ξ of the left (right) Furry-Feynman diagram in Fig. 3.1, in weak laser fields $\xi \ll 1$. The particle are marked by their momenta in free space.

parameters, containing spinor-matrix products:

$$\begin{aligned} M^{\mu}(q,q'|n) =& \bar{u}_{p',s'}\{b_n\gamma^{\mu} - (\frac{ea\not{\epsilon}\not{k}\gamma^{\mu}}{2k\cdot p'} + \frac{ea\gamma^{\mu}\not{k}\not{\epsilon}}{2k\cdot p})c_n + \frac{e^2a^2k^{\mu}\not{k}}{2(k\cdot p')(k\cdot p)}d_n\}u_{p,s}\,, \\ M_{\mu}(q_+,q_-|n') =& \bar{u}_{p_-,s_-}\{B_{n'}\gamma_{\mu} - (\frac{ea\not{\epsilon}\not{k}\gamma_{\mu}}{2k\cdot p_-} - \frac{ea\gamma_{\mu}\not{k}\not{\epsilon}}{2k\cdot p_+})C_{n'} - \frac{e^2a^2k_{\mu}\not{k}}{2(k\cdot p_+)(k\cdot p_-)}D_{n'}\} \\ & \times u_{p_+,s_+}\,, \end{aligned} \tag{3.8}$$

where $n' = N - n$, and the coefficients are linear combinations of the generalized Bessel functions

$$\begin{aligned} b_n =& J_n(\theta_1,\theta_2)\,, \\ c_n =& \frac{1}{2}[J_{n-1}(\theta_1,\theta_2) + J_{n+1}(\theta_1,\theta_2)]\,, \\ d_n =& \frac{1}{4}[J_{n-2}(\theta_1,\theta_2) + 2J_n(\theta_1,\theta_2) + J_{n+2}(\theta_1,\theta_2)]\,, \end{aligned} \tag{3.9}$$

with the arguments

$$\begin{aligned} \theta_1 =& \frac{ea(\epsilon\cdot p')}{k\cdot p'} - \frac{ea(\epsilon\cdot p)}{k\cdot p}\,, \\ \theta_2 =& \frac{e^2a^2}{8}\left[\frac{1}{k\cdot p} - \frac{1}{k\cdot p'}\right]\,. \end{aligned} \tag{3.10}$$

Similarly,

$$\begin{aligned} B_{n'} =& J_{n'}(\Theta_1,\Theta_2)\,, \\ C_{n'} =& \frac{1}{2}[J_{n'-1}(\Theta_1,\Theta_2) + J_{n'+1}(\Theta_1,\Theta_2)]\,, \\ D_{n'} =& \frac{1}{4}[J_{n'-2}(\Theta_1,\Theta_2) + 2J_{n'}(\Theta_1,\Theta_2) + J_{n'+2}(\Theta_1,\Theta_2)]\,, \end{aligned} \tag{3.11}$$

with the arguments

$$\begin{aligned} \Theta_1 =& \frac{ea(\epsilon\cdot p_-)}{k\cdot p_-} - \frac{ea(\epsilon\cdot p_+)}{k\cdot p_+}\,, \\ \Theta_2 =& -\frac{e^2a^2}{8}\left[\frac{1}{k\cdot p_-} + \frac{1}{k\cdot p_+}\right]\,. \end{aligned} \tag{3.12}$$

In Eq. (3.7), $\delta(q + Nk - q' - q_+ - q_-)$ guarantees the four-momentum conservation of the process in which $|N|$ laser photons are absorbed ($N > 0$), or emitted ($N < 0$). This leads to the threshold condition for the participating photon number

$$N\omega' \geq 4m_*\,, \tag{3.13}$$

where ω' is the laser photon energy in the average rest frame of the projectile. This frame is defined by the vanishing of the laser-dressed three-momentum, $\mathbf{q} = 0$. The intensity

dependence of the dressed mass $m_* = m\sqrt{1+\xi^2}$ influences the threshold; for example, $N \geq 6$ for the SLAC parameters $p^0 = 46.6\,\mathrm{GeV}$, $\omega = 2.35\,\mathrm{eV}$ and $\xi \approx 0.3$ [27], whereas $N \geq 5$ photons would suffice in a weaker field ($\xi < 0.22$). The proof of Eq. (3.13) is given in Appendix A.

The total rate is obtained as

$$R = \frac{1}{T}\int \frac{Vd^3q_+}{(2\pi)^3}\int \frac{Vd^3q_-}{(2\pi)^3}\int \frac{Vd^3q'}{(2\pi)^3}\frac{1}{4}\sum_{\text{spins}}|S_{fi}|^2\,, \tag{3.14}$$

with the interaction time T, and a statistical factor $1/4$ due to initial spin averaging and the two identical final-state electrons. Further derivation is carried out with the formal replacement rule [81] of $[\delta(q+Nk-q'-q_+-q_-)]^2 = \frac{VT}{(2\pi)^4}\delta(q+Nk-q'-q_+-q_-)$, and the conversion of the spin sum into voluminous trace products:

$$\begin{aligned}
R =& \frac{1}{T}\int \frac{Vd^3\mathbf{q}'}{(2\pi)^3}\int \frac{Vd^3\mathbf{q}_+}{(2\pi)^3}\int \frac{Vd^3\mathbf{q}_-}{(2\pi)^3}(\alpha\frac{2(2\pi)^5m^2}{V^2\sqrt{q^0q'^0q_+^0q_-^0}})^2\\
&\times\frac{1}{4}\sum_{s_0,s',s_+,s_-}\frac{VT}{(2\pi)^4}\sum_N\delta(q+Nk-q'-q_+-q_-)\\
&\times\sum_{n_1}\sum_{n_2}(\widetilde{M}^{qq'}_{n_1n_2}+\widetilde{M}^{qq_-}_{n_1n_2}-2\widetilde{M}^{\mathtt{ex}}_{n_1n_2})\\
=&\frac{\alpha^2m^4}{(2\pi)^3q^0}\int\frac{d^3\mathbf{q}'}{q'^0}\int\frac{d^3\mathbf{q}_+}{q_+^0}\int\frac{d^3\mathbf{q}_-}{q_-^0}\sum_N\delta(q+Nk-q'-q_+-q_-)\\
&\times\sum_{n_1}\sum_{n_2}\sum_{s_0,s',s_+,s_-}(\widetilde{M}^{qq'}_{n_1n_2}+\widetilde{M}^{qq_-}_{n_1n_2}-2\widetilde{M}^{\mathtt{ex}}_{n_1n_2})\,,
\end{aligned}\tag{3.15}$$

where $\sum_{s_0,s',s_+,s_-}\widetilde{M}^{qq'}_{n_1n_2}$ and $\sum_{s_0,s',s_+,s_-}\widetilde{M}^{qq_-}_{n_1n_2}$ are matrix trace products:

$$\begin{aligned}
\sum_{s_0,s',s_+,s_-}\widetilde{M}^{qq'}_{n_1n_2} =& \frac{1}{(q-q'+n_1k)^2}\frac{1}{(q-q'+n_2k)^2}\\
&\times Tr[\frac{\not{p}_-+m}{2m}\Gamma_{\mu n_1}(q_-,q_+)\frac{\not{p}_+-m}{2m}\bar{\Gamma}_{\nu n_2}(q_-,q_+)]\\
&\times Tr[\frac{\not{p}'+m}{2m}\Gamma^{\mu}_{n_1}(q,q')\frac{\not{p}+m}{2m}\bar{\Gamma}^{\nu}_{n_2}(q,q')]\,,
\end{aligned}\tag{3.16}$$

with

$$\Gamma^{\mu}_{n_1}(q,q') = b_{n_1}\gamma^{\mu} - (\frac{ea\not{\epsilon}\not{k}\gamma^{\mu}}{2kp'}+\frac{ea\gamma^{\mu}\not{k}\not{\epsilon}}{2kp})c_{n_1}+\frac{e^2a^2k^{\mu}\not{k}}{2(kp')(kp)}d_{n_1}\,, \tag{3.17a}$$

$$\Gamma_{\mu n_1}(q_-,q_+) = B_{N-n_1}\gamma_{\mu} - (\frac{ea\not{\epsilon}\not{k}\gamma_{\mu}}{2kp_-}-\frac{ea\gamma_{\mu}\not{k}\not{\epsilon}}{2kp_+})C_{N-n_1}-\frac{e^2a^2k_{\mu}\not{k}}{2(kp_+)(kp_-)}D_{N-n_1}\,, \tag{3.17b}$$

and $\bar{\Gamma} = \gamma^0\Gamma^{\dagger}\gamma^0$. $\sum_{s_0s's_+s_-}\widetilde{M}^{qq_-}_{n_1n_2}$ can be obtained from $\sum_{s_0s's_+s_-}\widetilde{M}^{qq'}_{n_1n_2}$ by the exchanges of $q' \rightleftarrows q_-$ as well as $p' \rightleftarrows p_-$ in Eq. (3.16). $\sum_{s_0s's_+s_-}\widetilde{M}^{\mathtt{ex}}_{n_1n_2}$ accounts for the interference of

diagrams with exchanged electrons in the final state:

$$\sum_{s_0 s' s_+ s_-} \widetilde{M}^{\mathtt{ex}}_{n_1 n_2} = \frac{1}{(q-q'+n_1 k)^2}\frac{1}{(q-q_-+n_2 k)^2} \times Tr[\frac{\not{p}_- + m}{2m}\Gamma_{\mu n_1}(q_-,q_+)\frac{\not{p}_+ - m}{2m}\bar{\Gamma}_{\nu n_2}(q',q_+) \times \frac{\not{p}' + m}{2m}\Gamma^{\mu}_{n_1}(q,q')\frac{\not{p} + m}{2m}\bar{\Gamma}^{\nu}_{n_2}(q,q_-)] \,. \tag{3.18}$$

The 9-dimensional integration for the total rate (3.14) is first reduced to a 5-dimensional one by the δ-function. Still, the remaining multi-dimensional integration is time consuming, and we apply an appropriate Monte Carlo method to speed up the computation. The coordinate system used for the integration is described in Appendix B (see also [57]).

As mentioned before, the limit $\omega \to 0$ corresponds to the trident pair production in constant-crossed fields [78]. It is manifested in the next section that in the weak-field, one-photon limit ($\xi \ll 1$, $N = 1$), our approach reproduces the well-known cross section for pair creation by a single γ-photon on an electron, the Feynman diagrams of which are shown in Fig. 3.2. Therefore, the documented results of single-photon trident pair production [57] are as important as useful for checking the creditability of our program for numerical calculations.

3.2.2 Low-intensity limit and single-photon trident pair production

In the derivation of the Volkov states and the laser-dressed QED, the laser field enters as a classical field. Notably, quantum features appear automatically when the phase term of the Volkov solution, or the scattering amplitude, is Fourier-expanded, leading to the interpretation of photon absorption. In the weak-field limit ($\xi \ll 1$), the Volkov states naturally reduces to the free particle solution of the Dirac equation, and it is relevant to expect the exact consistency of the laser-dressed QED with the conventional perturbative theory where the electromagnetic wave is treated as a quantized field from the beginning. We show below that this is indeed the case, by comparing the amplitudes of the corresponding Feynman diagrams and Furry-Feynman diagrams in the low-intensity limit.

The amplitude (3.7) accounts for the left diagram in Fig. 3.1, which is to be compared with the sum of amplitudes of the first four diagrams in Fig. 3.2. If their equivalence is established, the amplitudes of the respective diagrams with exchanged momentum are plainly equal.

Note that in the limit $a \to 0$, the spinor-matrix product term in Eq. (3.7) is at least proportional to a^N. Therefore, only the channel $N = 1$ matters as long as energy-momentum conservation is fulfilled. The threshold condition is the same as for the single-photon trident pair production process [57], since both the laser-dressed momenta and the laser-dressed masses approach their free-field values.

For the left diagram in Fig. 3.1 with that $N = 1$, let's first look at the part with $n = 1$. It indicates in the Furry-Feynman diagram that the laser photon is absorbed at the vertex which connects the initial and final states of the projectile electron. Naturally, it is expected to be related with the sum of the first two diagrams in Fig. 3.2, where the photon is absorbed by the projectile electron in its initial or final state. Using the ordinary Feynman rules of the external-field-free QED theory, the matrix element of the process can be written as

$$\begin{aligned}
\mathcal{M}^{\texttt{single-photon}}(q, q', q_+, q_-, k) =& \alpha e \frac{2(2\pi)^5\sqrt{2\pi}m^2}{V^2\sqrt{p^0p'^0p_+^0p_-^0\omega V}} \frac{\delta^{(4)}(p + k - p' - p_+ - p_-)}{(p - p' + k)^2} \\
&\times [\bar{u}_{p',s'} \not{\epsilon} \frac{(\not{p}' - \not{k}) + m}{(p' - k)^2 - m^2} \gamma_\mu u_{p,s} \bar{u}_{p_-,s_-} \gamma^\mu u_{p_+,s_+} \\
&+ \bar{u}_{p',s'} \gamma_\mu \frac{(\not{p} + \not{k}) + m}{(p + k)^2 - m^2} \not{\epsilon} u_{p,s} \bar{u}_{p_-,s_-} \gamma^\mu u_{p_+,s_+}] \\
=& \alpha e \frac{2(2\pi)^5\sqrt{2\pi}m^2}{V^2\sqrt{p^0p'^0p_+^0p_-^0\omega V}} \frac{\delta^{(4)}(p + k - p' - p_+ - p_-)}{(p - p' + k)^2} \\
&\times \bar{u}_{p',s'} [\not{\epsilon} \frac{-\not{k} + \not{p}' + m}{-2k \cdot p'} \gamma_\mu + \gamma_\mu \frac{\not{k} + \not{p} + m}{2k \cdot p} \not{\epsilon}] u_{p,s} \\
&\times \bar{u}_{p_-,s_-} \gamma^\mu u_{p_+,s_+} \,. \qquad (3.19)
\end{aligned}$$

On the other hand, the Furry-Feynman diagram corresponds to Eq. (3.7) with $N = n = 1$. Its coefficients of generalized Bessel functions take the asymptotic form or vanish as $a \to 0$. To the leading order, the coefficients are

$$\begin{aligned}
b_1 =& J_1(\theta_1, \theta_2) = \frac{\theta_1}{2} \,, \\
c_1 =& \frac{1}{2}[J_0(\theta_1, \theta_2) + J_2(\theta_1, \theta_2)] = \frac{1}{2} \,, \\
d_1 =& \frac{1}{4}[J_{-1}(\theta_1, \theta_2) + 2J_1(\theta_1, \theta_2) + J_3(\theta_1, \theta_2)] = -\frac{\theta_1}{8} \,, \qquad (3.20)
\end{aligned}$$

with the arguments θ_1 of Eq. (3.10), and

$$\begin{aligned}
B_0 =& J_0(\Theta_1, \Theta_2) = 1 \,, \\
C_0 =& \frac{1}{2}[J_{-1}(\Theta_1, \Theta_2) + J_1(\Theta_1, \Theta_2)] = 0 \,, \\
D_0 =& \frac{1}{4}[J_{-2}(\Theta_1, \Theta_2) + 2J_0(\Theta_1, \Theta_2) + J_2(\Theta_1, \Theta_2)] = \frac{1}{2} \,. \qquad (3.21)
\end{aligned}$$

Therefore, to the lowest order in a, the amplitude (3.7) reads

$$\begin{aligned}
\mathcal{M}(q,q',q_+,q_-) =& -\alpha\frac{2(2\pi)^5m^2}{V^2\sqrt{p^0p'^0p_+^0p_-^0}}\frac{\delta^{(4)}(p+k-p'-p_+-p_-)}{(p-p'+k)^2}\\
&\times\bar{u}_{p',s'}\{(\frac{ea(\epsilon\cdot p')}{2k\cdot p'}-\frac{ea(\epsilon\cdot p)}{2k\cdot p})\gamma^\mu-(\frac{ea\not{\epsilon}\not{k}\gamma^\mu}{4k\cdot p'}+\frac{ea\gamma^\mu\not{k}\not{\epsilon}}{4k\cdot p})\}u_{p,s}\bar{u}_{p_-,s_-}\gamma_\mu u_{p_+,s_+}\\
=&\alpha e\frac{a}{2}\frac{2(2\pi)^5m^2}{V^2\sqrt{p^0p'^0p_+^0p_-^0}}\frac{\delta^{(4)}(p+k-p'-p_+-p_-)}{(p-p'+k)^2}\\
&\times\bar{u}_{p',s'}\{\frac{\not{\epsilon}\not{k}-\not{\epsilon}\not{p}'-\not{p}'\not{\epsilon}}{2k\cdot p'}\gamma^\mu+\gamma^\mu\frac{\not{k}\not{\epsilon}+\not{p}\not{\epsilon}+\not{\epsilon}\not{p}}{2k\cdot p}\}u_{p,s}\bar{u}_{p_-,s_-}\gamma_\mu u_{p_+,s_+}\\
=&\alpha e\frac{\bar{A}}{\sqrt{2}}\frac{2(2\pi)^5m^2}{V^2\sqrt{p^0p'^0p_+^0p_-^0}}\frac{\delta^{(4)}(p+k-p'-p_+-p_-)}{(p-p'+k)^2}\\
&\times\bar{u}_{p',s'}\{\not{\epsilon}\frac{-\not{k}+\not{p}'+m}{-2k\cdot p'}\gamma_\mu+\gamma_\mu\frac{\not{k}+\not{p}+m}{2k\cdot p}\not{\epsilon}\}u_{p,s}\bar{u}_{p_-,s_-}\gamma^\mu u_{p_+,s_+}\\
=&\bar{A}\sqrt{\frac{\omega V}{4\pi}}\mathcal{M}^{\texttt{single-photon}}(q,q',q_+,q_-,k)\,,
\end{aligned}\tag{3.22}$$

where the factor $\bar{A}\sqrt{\frac{\omega V}{4\pi}}$ equals to the square root of the number of laser photons in the volume V. Since the energy density of the electromagnetic field in Gaussian units is given by [81],

$$I_{\texttt{field}}=\frac{1}{8\pi}\int\langle\mathbf{E}^2+\mathbf{B}^2\rangle=\frac{1}{4\pi}\int\langle\mathbf{E}^2\rangle\,,\tag{3.23}$$

where $\mathbf{E}$ and $\mathbf{B}$ are the electric field vector and the magnetic field vector, respectively, with $\langle\mathbf{E}^2\rangle=\langle\mathbf{B}^2\rangle$ on average being applied, and $\langle\mathbf{E}^2\rangle=\langle(-\partial\mathbf{A}/\partial t)^2\rangle=\omega^2\langle\mathbf{A}^2\rangle=\omega^2\bar{A}^2$, the total number of photons in the volume V is

$$N^{\texttt{photon}}=\frac{I_{\texttt{field}}V}{\omega}=\frac{\omega\bar{A}^2}{4\pi}V=\frac{\omega m^2}{4\pi\alpha}\xi^2V\,.\tag{3.24}$$

The same relation as shown in Eq. (3.22) can be proved for the case $n=0$ as well, where the laser photon is absorbed by the produced pair. The channels with $n<0$ or $N-n<0$ are negligible, since then the amplitude is of higher order in a. The above proof works naturally also for the matrix element of the exchange diagrams. Therefore, we have proved in the weak-field limiting case, the equivalence of the laser-dressed amplitude and its external-field-free correspondence up to a factor $\sqrt{N^{\texttt{photon}}}$, which means nothing else but the normalization of the field

$$R^{\texttt{laser-dressed}}_{\xi\ll1}=N^{\texttt{photon}}R^{\texttt{external-field-free}}\,.\tag{3.25}$$

This consistency facilitates the check of our theoretical derivation and numerical calculation, by referring to the documented numerical results obtained for the single-photon trident pair production process [57]. The match of the numbers adds confidence to our program, shown in Table 3.1.

Table 3.1: Total cross section of the single-photon trident pair production (in mb) as functions of the photon energy ω which refers to the electron rest frame. The σ_T^M are Mork's results from Ref. [57]. The $\sigma_T^{1,2,3}$ show our results from several runnings of the Monte Carlo program.

ω/m	σ_T^M	σ_T^1	σ_T^2	σ_T^3
4.4	0.0011	0.0011	0.0011	0.0011
6.0	0.0462	0.0461	0.0459	0.0460
8.0	0.176	0.175	0.175	0.176
12.0	0.518	0.520	0.518	0.519

3.2.3 Theory of the resonance

I. The resonance condition

In the case $N > 1$ in Eq. (3.15), more than one photon participates in the process. An important feature arises that the intermediate photon can reach the mass shell to become a real photon. It happens in the multi-photon regime, where the energy-momentum conservation could allow certain combinations of the kinematic parameters to satisfy

$$\begin{aligned} k'^2 &= (q - q' + nk)^2 = 0\,, \text{ or} \\ k'^2 &= (q - q_- + nk)^2 = 0\,, \end{aligned} \tag{3.26}$$

for the left and right diagram in Fig. 3.1. $k'^2 = 0$ is a pole of the propagator, around which the integration in Eq. (3.15) should be treated carefully. The channels with poles in the propagator often possess a large enhancement compared to the pole-free situation. The case where the intermediate photon becomes 'real' is usually referred to as a resonance [42].

According to the derivation in Appendix C, a resonance can happen only if n, the number of photons absorbed at the first vertex in Fig. 3.1, adopts a value in the interval $[n_{min}, n_{max}]$, where

$$n_{min} = \text{Ceiling}[(\frac{\sqrt{N}}{2} - \sqrt{\frac{N}{4} - \frac{m_*^2}{k\cdot q}})^2]\,, \tag{3.27a}$$

$$n_{max} = \text{Floor}[(\frac{\sqrt{N}}{2} + \sqrt{\frac{N}{4} - \frac{m_*^2}{k\cdot q}})^2]\,, \tag{3.27b}$$

with Ceiling (Floor) denoting the smallest (largest) integer being larger (smaller) than the argument. Notice that $N\,k\cdot q \geq 4m_*^2$ always holds as can be seen from the threshold condition (3.13). If the interval $[n_{min}, n_{max}]$ does not cover any integer, the intermediate photon is always off shell.

For any integer $n \in [n_{min}, n_{max}]$, there always exists a related section $[c_1, c_2]$ of electron energies. If a resonance takes place for the left (right) diagram in Fig. 3.1, it requires that $q'^0 \in [c_1, c_2]$ ($q_-^0 \in [c_1, c_2]$). The explicit expressions for the boundaries are given in

the center of inertial frame, defined as $\mathbf{q} + N\mathbf{k} = 0$, by:

$$c_1 = \frac{1}{\sqrt{m_*^2 + 2Nk\cdot q}}[(N + n - \frac{n(m_*^2 + 2Nk\cdot q)}{m_*^2 + 2nk\cdot q})k\cdot q + m_*^2]\,, \tag{3.28a}$$

$$c_2 = 2|\mathbf{q}| - q^0. \tag{3.28b}$$

The detailed proof is presented in Appendix C.

The physical meaning of the resonance is that since the intermediate photon goes on shell, the whole process is divided into two subsequent processes: at the first step, the (multi-photon) Compton scattering produces a highly energetic photon, and at the second step, a nonlinear Breit-Wheeler process (3.3) takes place where this energetic photon collides further with the laser photons to generate an e^+e^- pair. Channels without resonances, where either n is outside $[n_{min}, n_{max}]$ or q'^0 (q_-^0) is not in the region $[c_1, c_2]$, have the intermediate photon off shell, and the process is of nonlinear Bethe-Heitler type (3.2).

II. Formal divergence of integrations in a resonance process

We now discuss in detail the treatment of resonances in our calculation. For the benefits of discussing the poles, we consider Eq. (3.15) in the form

$$\begin{aligned}
R =&\frac{\alpha^2 m^4}{(2\pi)^3 q^0}\int\frac{d^3\mathbf{q}'}{q'^0}\int\frac{d^3\mathbf{q}_+}{q_+^0}\int\frac{d^3\mathbf{q}_-}{q_-^0}\sum_N\delta(q+Nk-q'-q_+-q_-)\\
&\times\sum_{n_1}\sum_{n_2}\sum_{s_0 s' s_+ s_-}(\widetilde{M}^{qq'}_{n_1n_2}+\widetilde{M}^{qq_-}_{n_1n_2}-2\widetilde{M}^{\mathtt{ex}}_{n_1n_2})\\
=&\frac{\alpha^2 m^4}{(2\pi)^3 q^0}\int\frac{d^3\mathbf{q}'}{q'^0}\int\frac{d^3\mathbf{q}_+}{q_+^0}\int\frac{d^3\mathbf{q}_-}{q_-^0}\sum_N\delta(q+Nk-q'-q_+-q_-)\sum_{n_1}\sum_{n_2}\\
&\left[\frac{\widetilde{f}^{qq'}_{n_1n_2}}{((q-q'+n_1k)^2+i\epsilon)((q-q'+n_2k)^2+i\epsilon)^*}\right.\\
&+\frac{\widetilde{f}^{qq_-}_{n_1n_2}}{((q-q_-+n_1k)^2+i\epsilon)((q-q_-+n_2k)^2+i\epsilon)^*}\\
&-\frac{\widetilde{f}^{\mathtt{ex}}_{n_1n_2}}{((q-q'+n_1k)^2+i\epsilon)((q-q_-+n_2k)^2+i\epsilon)^*}\\
&\left.-\frac{\widetilde{f}^{\mathtt{ex}}_{n_1n_2}}{((q-q'+n_1k)^2+i\epsilon)^*((q-q_-+n_2k)^2+i\epsilon)}\right],
\end{aligned}\tag{3.29}$$

where the $\widetilde{f}$ represents the trace or the trace product part of the function $\widetilde{M}$. They are well-defined continuous real functions without poles, as can be seen, e. g., in Eq. (3.16) and (3.18). In Eq. (3.29) the Feynman prescription with the small $i\epsilon$ in the propagator is included explicitly, since it plays a crucial role in integrating around the poles.

The poles in the propagators do not always cause problems, such as in

$$\frac{1}{((q-q'+n_1k)^2+i\epsilon)((q-q'+n_2k)^2+i\epsilon)^*}\,,\ \text{with } n_1\neq n_2\,, \tag{3.30}$$

and in

$$\frac{1}{((q-q'+n_1k)^2+i\epsilon)((q-q_-+n_2k)^2+i\epsilon)^*}\,. \tag{3.31}$$

In the above cases, only first-order poles appear, and thus the contour integrals are convergent with the standard application of the residue theorem. However, the integration of the term

$$\frac{1}{((q-q'+nk)^2+i\epsilon)((q-q'+nk)^2+i\epsilon)^*} = \left|\frac{1}{(q-q'+nk)^2+i\epsilon}\right|^2 \tag{3.32}$$

is not defined. The poles which appear here have a divergence order of two, and formally lead to unphysical infinities (see also Appendix D). Compared to this 'infinite' part, the finite integration about (3.31) is negligible. This is consistent with an intuitive argument: the term (3.31) is related to the exchange effect, and physically speaking, at the resonance the exchange effect should only give a small contribution, because the two outgoing electrons gain their 'distinguishability' as they are coming out separately from two subsequent processes instead of one.

Generally speaking, for the divergent integration of (3.32) it is required to apply either a cut-off in the integration space, for example, by making use of the real vector potential of a finite laser pulse instead of the monochromatic plane-wave approximation, or a certain regularization of the propagator, for example, by introducing an imaginary energy (mass) correction in the propagator to account for the decay of the particle states in the laser field. The fact that a particle state has a finite lifetime in a laser field is attributed both to the Volkov state's decay into a field-free state as it propagates out of a finite laser pulse, and to the laser-particle reactions, such as (multi-photon) Compton scattering.

One version of the regularization method can be found in nonrelativistic quantum mechanics about the treatment of the resonance scattering containing an unstable atomic state [52]. There, the atomic level broadening should be taken into account, which can be caused by various mechanisms, such as natural broadening due to spontaneous emission, impact pressure broadening due to particle collision, and so on. These reactions define the decay rate of the state

$$\Gamma = \frac{\text{Number of decays per unit time}}{\text{Number of unstable particles}} = \sum_{\texttt{decay channels}} \Gamma_i\,. \tag{3.33}$$

The lifetime of the particle is the reciprocal of the total decay rate Γ. By Heisenberg uncertainty principle, it leads to an energy uncertainty

$$\Delta E \gtrsim \Gamma\,, \tag{3.34}$$

and results in an imaginary correction to the eigenenergy E_0 of the atomic state

$$E' = E_0 - i\Gamma\,. \tag{3.35}$$

Accordingly, the Fourier transform of the scattering amplitude takes the Breit-Wigner form

$$S \propto \frac{1}{E - E_0 + i\Gamma}\,, \tag{3.36}$$

and the scattering cross section is rendered finite

$$\sigma \propto \frac{1}{(E-E_0)^2+\Gamma^2}\,, \tag{3.37}$$

which possesses a resonance peak at $E = E_0$.

In laser-dressed QED, the Breit-Wigner procedure, which modifies the propagator in a resonance scattering amplitude with a finite imaginary term in the denominator, is widely applied, for example, in laser-assisted Møller scattering [41,42,82], Bhabha scattering [83], and bremsstrahlung emission [44, 84, 85]. However, due to the multi-particle nature of the QED theory, more care is required to assign this imaginary correction, since several particle energies and masses can be involved. In the following we discuss the regularization of the electron propagator, which has been extensively studied, to get an impression and retrieve important information for the next section, where the resonance case with the photon propagator of our interest is addressed.

Consider a laser-dressed electron propagator in a Furry-Feynman diagram, as it appears in laser-assisted bremsstrahlung,

$$\frac{1}{q^2-m_*^2} = \frac{1}{(q_i-k)^2-m_*^2}\,, \tag{3.38}$$

where q_i is the momentum of the incoming laser-dressed electron, k is the momentum of the bremsstrahlung photon, and q is the momentum of the intermediate laser-dressed electron. The resonance takes place when the intermediate electron reaches the mass shell, $q^2 = m_*^2$. According to the Breit-Wigner treatment, at resonance the propagator acquires a finite imaginary term

$$\frac{1}{q^2-m_*^2+i\Gamma'} = \frac{1}{(q_i-k)^2-m_*^2+i\Gamma'}\,, \tag{3.39}$$

where the notation Γ' is used to distinguish it from Γ in Eq. (3.33-3.35), that defines the decay rate of an atomic system.

In an infinitely-extended laser field, an electron in a Volkov state is still not stable, due to laser-dressed spontaneous radiation. In a weak laser field ($\xi \ll 1$), the Furry-Feynman diagram of the spontaneous radiation can be expanded in the laser-electron coupling parameter ξ into infinitely many ordinary Feynman diagrams, illustrated in Fig. 3.3. In this way, it can be viewed as the sum of various laser-induced (multi-photon) Compton scattering processes. It is established by the Cutkosky rules [52] that the imaginary part of the mass operator is related with the sum of the spontaneous decay rates of the intermediate electron over all possible final states, illustrated in Fig. 3.4. Therefore, this radiative correction results in an imaginary term in the electron's mass $m_* \to m_* - i\delta m$, which appears in the denominator of the propagator [52, 84, 85]

$$\frac{1}{q^2-(m_*-i\delta m)^2} = \frac{1}{q^2-m_*^2+2im_*\delta m}\,. \tag{3.40}$$

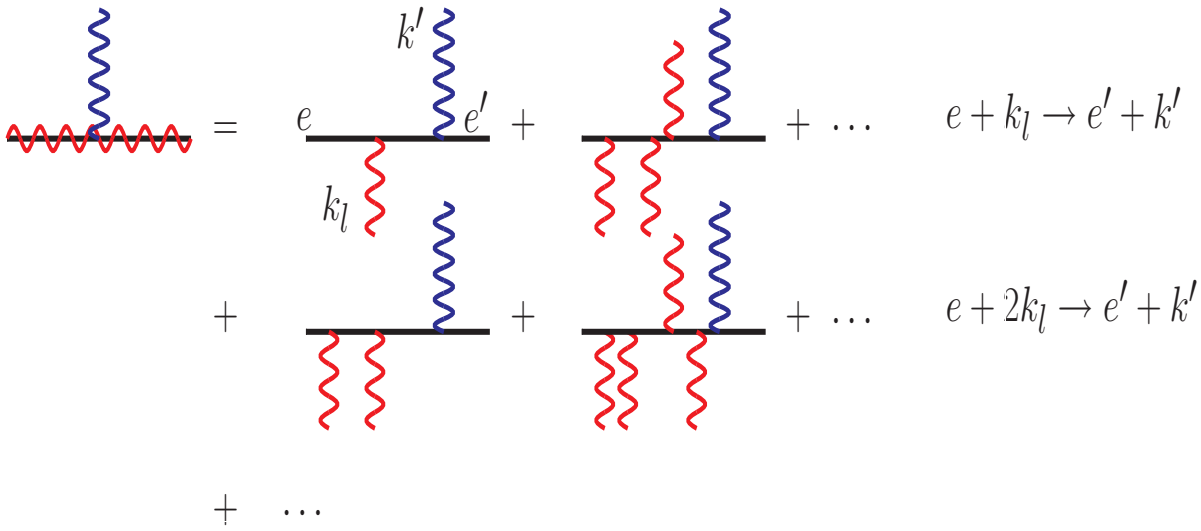

Figure 3.3: The expansion of the amplitude for laser-dressed spontaneous emission into infinitely many laser-induced (multi-photon) Compton scattering processes in a weak laser field ($\xi \ll 1$). Here k_l denotes the laser mode, while k' denotes the spontaneous radiation mode. e and e' designate the electron before and after the scattering. The photon lines above (below) the particle line represents emitted (absorbed) photons. Each multi-photon Compton scattering with a specific net number of laser photons absorbed contains infinitely many processes of different conditions with respect to the number of laser photons absorbed and emitted transiently, as indicated.

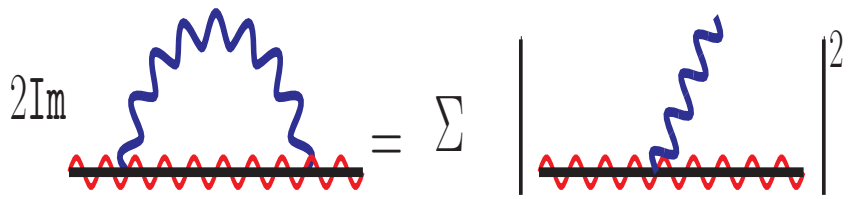

Figure 3.4: The equivalence of the double imaginary part of the mass operator of an electron in a laser field and the sum of the total rates of all possible laser-dressed spontaneous radiations. $\sum$ denotes the operation of sum (integration) over all possible final states of the electron and photon.

Moreover, not only the insertion of an imaginary mass, but also an imaginary energy correction is required, which arises as the incoming electron also decays via the laser-dressed spontaneous radiation. It is noted in [85] that, if this imaginary energy correction is omitted, the total cross section would be overestimated by several orders of magnitude in the laser-dressed bremsstrahlung process studied there.

The necessity to take into account the finite lifetime of the incoming electron has an intuitive physical explanation. Since the intermediate electron is produced within the incoming electron's lifetime, it naturally possesses an energy uncertainty according to Heisenberg uncertainty principle, which is directly 'inherited' from the 'mother' electron, and is independent of the imaginary mass correction originating from its own decay. Therefore, the regulator $i\Gamma'$ in Eq. (3.39) is attributed to two sources, the decay of the incoming electron, and the intermediate electron's own decay. The complete propagator is

$$\begin{aligned}&\frac{1}{(q_i-k+i\Gamma(q_i)\hat{n})^2-(m_*-i\delta m)^2}\\=&\frac{1}{(q_i-k)^2-m_*^2+2i(m_*\delta m+(q_i^0-k^0)\Gamma(q_i))}\,,\end{aligned}\tag{3.41}$$

where $i\Gamma(q_i)$ denotes the incoming-electron-induced imaginary energy correction, and $\hat{n}$ is a time-like vector, $\hat{n}=(1,0,0,0)$.

In the next section, we apply the regularization method to treat the resonance problem with the photon propagator. The regulator of a finite imaginary term in the propagator is first introduced by an intuitive application of the Breit-Wigner procedure. It is then confirmed in a systematic way based on a comparison with the cascade theory. In our case, the finite duration of the laser pulse is also taken into account, which sets a time scale for an electron staying in a Volkov state.

III. Regularization method

Without loss of generality, in the following we discuss the squared propagator (3.32) and its related integral. The conclusions obtained are applicable for the integral with q' exchanged by q_- as well.

Before specifying the regulator, we can follow some steps like in a parameter-independent method used in Ref. [86], where the propagator is split into two terms

$$\begin{aligned}&\left|\frac{1}{(q-q'+nk)^2+i\epsilon}\right|^2\\=&\left|\frac{(q-q'+nk)^2}{(q-q'+nk)^4+\epsilon^2}+\frac{-i\epsilon}{(q-q'+nk)^4+\epsilon^2}\right|^2\\=&\left(\frac{(q-q'+nk)^2}{(q-q'+nk)^4+\epsilon^2}\right)^2+\left(\frac{\epsilon}{(q-q'+nk)^4+\epsilon^2}\right)^2.\end{aligned}\tag{3.42}$$

Accordingly, the integration in Eq. (3.29) can be divided into two parts according to the two terms in Eq. (3.42). This formal propagator splitting turns out to facilitate

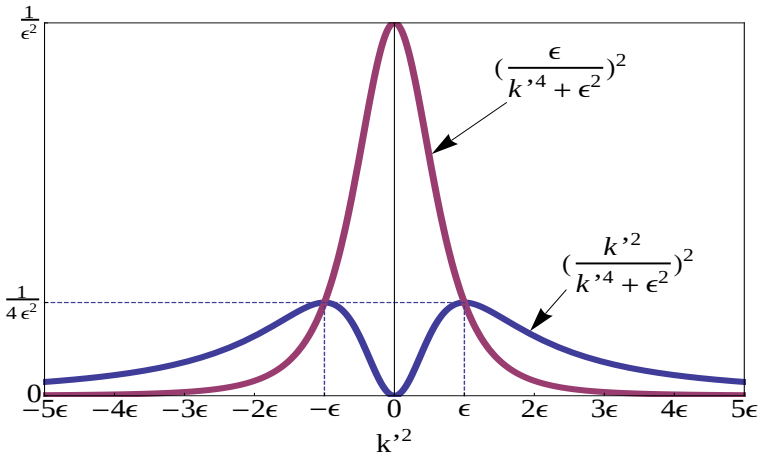

Figure 3.5: Sketch of the two terms of the squared propagator given by Eq. (3.42). The quantity $k' = q - q' + nk$ is the momentum of the intermediate photon.

the subsequent analytical derivations. For example, it is demonstrated in Appendix D that, in the limit $\epsilon \to 0$, the amplitude corresponding to the second term takes the same form as the amplitude of a cascade process (see Eq. (D.7)) up to a factor $\frac{1}{2}$. It lays the basis for the derivations in Appendix E, where the regulator is determined via a manifest connection with the cascade theory.

As shown in Fig. 3.5, where we denote the intermediate photon's four-momentum by k', the second term of the squared propagator, that $(\frac{\epsilon}{k'^4+\epsilon^2})^2$, peaks at $k'^2 = 0$ where the on-shell condition is exactly fulfilled, and has dominant contribution in $|k'^2| \leq \epsilon$. On the other hand, the first term $(\frac{k'^2}{k'^4+\epsilon^2})^2$ vanishes at $k'^2 = 0$, and has a maximum at $|k'^2| = \epsilon$. Since ϵ scales as the energy uncertainty, it is reasonable to consider $|k'^2| \lesssim \epsilon$ as the criterion for a real photon produced in this process. Due to the fact that both integrations regarding the two terms of the squared propagator are mainly determined by the vicinity of $|k'^2| \sim \epsilon$, both of them contain contributions from real photons. It is worthy to note that, for a direct process where the intermediate photon is off-shell, the second term of the propagator is negligible for small ϵ, and the first term reduces to the ordinary photon propagator $\frac{1}{(q-q'+nk)^2}$.

Except for the splitting of the propagator displayed in Eq. (3.42), we will not apply the parameter-independent treatment further, and discussions can be found in Appendix E.

Similarly to the cases discussed in the previous section, in an infinitely extended laser field, a finite ϵ can be attributed to the decays of the particle states via the laser-dressed spontaneous radiation [41,82]. Denoting the lifetime of the intermediate electron state by τ_1, the propagator can be regularized via the Breit-Wigner procedure as

$$\frac{1}{(q-q'+nk+i\frac{1}{\tau_1}\hat{n})^2} = \frac{1}{(q-q'+nk)^2 + i(q^0-q'^0+nk^0)\frac{2}{\tau_1}}\,, \tag{3.43}$$

with $\epsilon = (q^0 - q'^0 + nk^0)\frac{2}{\tau_1}$. Notice that, if the duration τ_2 of the laser pulse seen by the electron is even shorter than τ_1, the Volkov states experience a shorter lifetime due to their decay into free states, and τ_2 should be used in the regulator.

The Breit-Wigner procedure is not an ab-initio treatment, and more discussions in detail about the assignment of the regulator are addressed in Appendix E. There ϵ is derived from another point of view, with a closer look at the area $\epsilon \sim 0$. By the requirement that the squared amplitude $|S_{fi}|^2$ containing only the second term of the propagator $(\frac{\epsilon}{(q-q'+nk)^4+\epsilon^2})^2$ should take the form of the square of the amplitude of the corresponding cascade process, it will be shown in a systematic way that

$$\epsilon = \frac{2(q^0 - q'^0 + nk^0)}{T}\,, \tag{3.44}$$

where T is the characteristic time of the process within which it takes place. It is natural that the lifetime of the particle state τ_1 , and the duration time τ_2 that the particle spends in the laser pulse, are appropriate candidates. This verifies the assignment of ϵ in Eq. (3.43).

Besides, the radiative corrections also lead to an imaginary modification of the propagator. As discussed in chapter 2, in external laser fields, the free photon propagator should be replaced by the full photon propagator [42, 53], including the laser-photon interaction via spontaneous laser-dressed e^+e^- production and annihilation, or the laser-dressed fermion loops in the language of Feynman diagrams. The vacuum polarization in external laser fields shifts the pole and regularizes the divergence by an imaginary mass correction to the photon. However, it turns out to be small in the cases we consider. For example, for the parameter set of the SLAC experiment, the correction is of the order of $\alpha\kappa^{\frac{2}{3}} \sim 10^{-3}$. That this term is negligible can also be argued intuitively. As revealed by the Cutkosky rules shown in Fig. 3.6, the double value of the imaginary mass correction equals the sum of the laser-dressed pair production rates over all the possible final states, which in our study is nevertheless much smaller than that of the competing processes, for example, the laser-dressed spontaneous radiation [41, 82].

We emphasize that our laser-dressed QED approach to multi-photon trident pair creation incorporates the direct process (the nonlinear Bethe-Heitler type) and the two-step process (the nonlinear Breit-Wheeler type) in a unified way. This is a general advantage of taking the Breit-Wigner procedure.

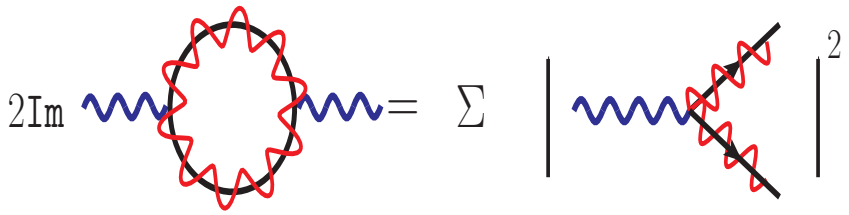

Figure 3.6: The equivalence of the double imaginary part of the vacuum polarization operator and the sum of the rates of all possible laser-dressed one-photon decays into an e^+e^- pair. $\sum$ denotes the sum (integration) over all possible final states of the electron and positron.

3.3 Numerical results on e^+e^- pair production in relativistic electron-laser collisions

3.3.1 Calculation for SLAC parameters

In the SLAC E-144 experiment, the electron beam and the laser beam were colliding under crossing angle of 17°. The laser focal waist size was about $4\,\mu$m. Hence, the electron passed through the laser focus in roughly $T_0 \approx 40\,$fs, which corresponds to a decay rate of the Volkov states being about $0.025\ \text{fs}^{-1}$.

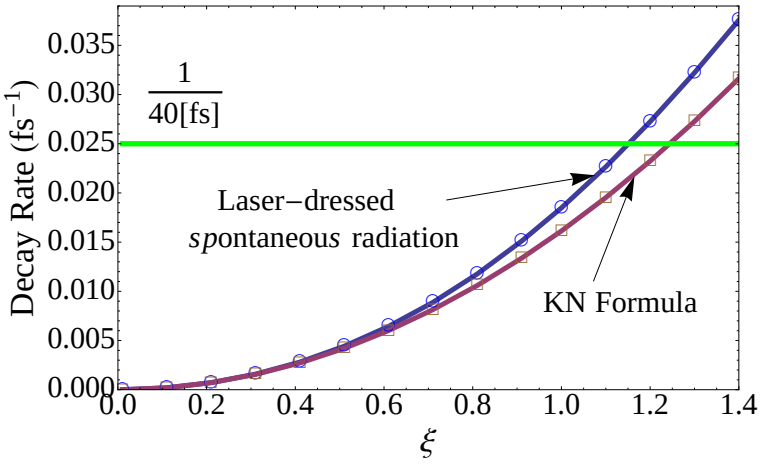

Figure 3.7: Decay rate (in the laboratory frame) dependence on ξ in the head-on collision of a 46.6 GeV electron with a linearly polarized 527 nm laser wave. The purple line shows the calculation via the Klein-Nishina formula for (single-photon) Compton scattering. The blue line shows the laser-dressed spontaneous decay, via the calculation of Volkov states, and contains the contributions from multi-photon Compton scattering. The green line shows the decay rate corresponding to the lifetime of a Volkov state in a pulsed laser field with duration 40 fs, which is the time the electron spends in the laser field in the SLAC experiment. For the SLAC experiment ($\xi \lesssim 0.3$), the decay rate is mainly determined by the 40 fs laser duration the electron experienced. Notice also that the nonlinear quantum effect, such as multi-photon Compton scattering, becomes significant as $\xi \gtrsim 1$.

As depicted in Fig. 3.7, it is much larger than the laser-dressed spontaneous decay rate for $\xi \leq 0.3$ in the experiment. The two rates become comparable when $\xi \sim 1$. Therefore, this (lab-frame) interaction time will be used as the characteristic time in the following. For comparison, the rate of (external-field-free) Compton scattering with one photon is also shown in Fig. 3.7. It is calculated from the differential cross-section $\frac{d\sigma_{\rm KN}}{d\Omega}$ given by the Klein-Nishina formula [81] as

$$R = N^{\texttt{photon}} \int d\Omega \frac{m}{Vp^0} \frac{d\sigma_{\rm KN}}{d\Omega} = \frac{\omega m^3}{4\pi\alpha p^0} \xi^2 \int d\sigma_{\rm KN}\,, \tag{3.45}$$

where $N^{\texttt{photon}} = \frac{\omega m^2}{4\pi\alpha}\xi^2 V$ is the number of laser photons in the volume V, as derived in

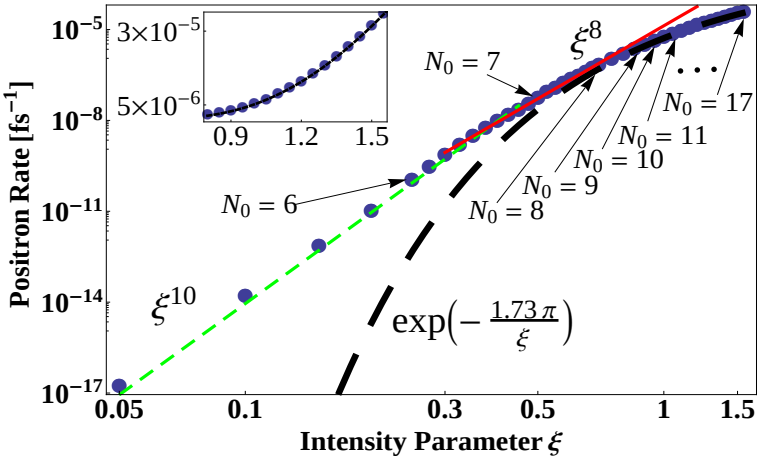

Figure 3.8: Positron rate dependence on ξ in the head-on collision of a 46.6 GeV electron with a linearly polarized 527 nm laser wave. The blue dots denote our numerical results from Eq. (4.8). The green short-dashed and red solid lines, respectively, are ξ^{10} and ξ^{8} power-law fits to the data, and the black long-dashed line is an exponential fit of the form $\exp[-\theta\pi/\xi]$ with $\theta = 1.73$. The numbers $N_0 = 6, \ldots, 17$ indicate the minimum numbers of laser photons that must be absorbed for the generation of an e^+e^- pair in different ξ regimes. The inset shows an enlargement of the nonperturbative $\xi \sim 1$ domain on a linear scale.

section 3.2.2, and the factor m/p^0 transforms the decay rate from the electron rest frame to the lab frame.

It is worthy to mention that, in implementing the calculation, T in Eq. (3.44) should be the lifetime (here T_0 in the lab frame) measured in the center of inertial frame (where $\mathbf{q} + N\mathbf{k} = 0$) which is the calculation frame always adopted in this chapter (see also Appendix B).

Fig. 3.8 shows the trident pair production rate as a function of the laser intensity parameter ξ. For the electron momentum and laser frequency chosen, the ξ dependence gradually changes from a ξ^{10} behavior ($\xi \lesssim 0.3$) to a flatter ξ^{8} increase ($\xi \sim 0.5$), and eventually leads into an exponential dependence ($\xi \sim 1$) similar to the famous Schwinger rate [87], see Eq. (1.2), and marking the transition into the fully nonperturbative regime. Here, photon orders up to $N \approx 50$ give significant contributions to the total rate.

The SLAC experiment found a rate scaling of $R \sim \xi^{10}$ around $\xi \approx 0.3$ [27], appearing indicative of the typical ξ^{2N_0} dependence in the perturbative domain. However, as mentioned in connection with Eq. (3.13), it is $N_0 = 6$ in the SLAC case. In fact, our simulation for $\xi = 0.3$ reveals that, on average, 6.44 photons are absorbed in total, with 1.62 (4.82) photons being absorbed at the first (second) vertex in Fig. 3.1. Hence, in contrast to the common interpretation, the SLAC experiment did not operate in the perturbative ξ^{2N_0}-domain but rather observed the onset of nonperturbative effects which would become more pronounced for $\xi \approx 1$ (see Fig. 3.8). The continuation of the ξ^{2N_0} behavior at $\xi \ll 1$ into the intensity domain where this N_0-th order channel has already closed was discussed in [88] and shown for the example of strong-field atomic ionization.

From Fig. 3.8 a total lab-frame positron rate per projectile of $R \approx 4 \times 10^4\,\mathrm{s}^{-1}$ results by averaging over a Gaussian laser focus peaked at $\xi = 0.3$. It is in reasonable agreement with the experimental result, where about 100 positrons were created in 22,000 shots from 10^7 electrons in the interaction region [27]. The corresponding rate is slightly smaller, $R_{\mathrm{exp}} \approx 10^4\,\mathrm{s}^{-1}$, which is mainly attributable to shot-to-shot intensity variations ($0.2 \lesssim \xi_{\mathrm{peak}} \lesssim 0.3$).

3.3.2 Positron spectrum and non-perturbative parameters

The energy distribution of the positrons is displayed in Fig. 3.9. Our calculations for the SLAC parameters [27] reproduce the measurements very well (apart from the data point at $q_0^+ \approx 15\,\mathrm{GeV}$), see Fig. 3.9(a). In addition we find that the spectral maximum remains at $q_0^+ \approx 13\,\mathrm{GeV}$ when the energy of the colliding electron is tuned in the calculation to correspond to various impact angles from 0° to 28°. This explains why the peak position in the experiment is not blurred by averaging over the laser focus and electron beam profile. We note besides, that the mean energy of the recoiled electron after head-on collision is 16.8 GeV, corresponding to an energy loss of 64%.

The fully nonperturbative regime could be probed, e. g., by utilizing 17.5 GeV electrons from the upcoming European XFEL beamline at DESY (Hamburg, Germany) [19] combined with a table-top 10 TW laser system. Here, the contributions from many photon orders form the positron spectrum, see Fig. 3.9(b). Such an experiment would represent a non-standard application of the XFEL electron beam, usually serving to generate x-ray light.

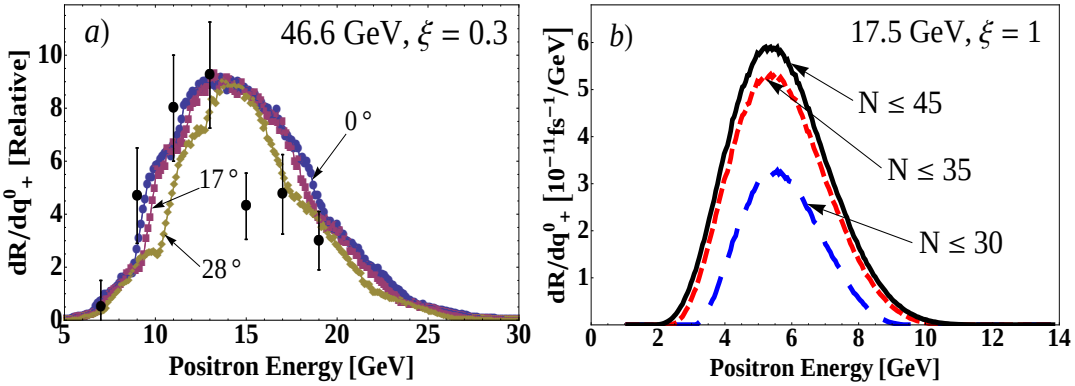

Figure 3.9: Positron energy spectra in electron collisions with a 527 nm laser beam. (a) $\xi = 0.3$ and $p^0 = 46.6\,\mathrm{GeV}$; the dots with an error bar are the experimental data from [27]. The three calculated curves refer to different center-of-mass energies, corresponding to different beam crossing angles as indicated, and have been normalized to the same height to facilitate their comparison. (b) Nonperturbative domain at $\xi = 1$ and $p^0 = 17.5\,\mathrm{GeV}$; the blue long-dashed (red short-dashed) line refers to the partial spectrum including up to 30 (35) absorbed photons. The black solid line shows the full spectrum ($N \leq 45$).

3.3.3 Accessability of the direct process

As discussed in Appendix E, in a resonance problem with a small ϵ, the rate is mainly determined by the region $|k'^2| \ll 1$ (see the discussion after Eq. (E.11)), and the total rate is proportional to the interaction time. Since $\frac{R_{\rm resonance}}{R_{\rm non-resonance}} \sim T$, the two-step process can always play a dominant role over the direct process as long as ϵ is small enough, or the interaction time T is long enough. Besides, although the two terms of the propagator shown in Eq. (3.42) have distinct behaviors in the non-resonance case, as one diminishes and the other reproduces the ordinary photon propagator, the conclusion can not be drawn that one corresponds to the two-step process and the other corresponds to the direct process in a resonance. This is due to the fact that for a finite T or ϵ, a strict distinction between off-shell and on-shell intermediate photons is not possible.

For the parameter set of the SLAC experiment, it has been found that the two-step process was dominant. The direct process has thus not been seen in experiment yet. It is studied intensively by theoreticians in laser-proton collisions [59–68], where Compton scattering is suppressed due to the large proton mass.

Here we identify a range of parameters where the direct process dominates also for the laser-electron collision. In the laboratory frame, the threshold for the direct process with N-photon absorption is found to be $\omega_{\rm BH} \gtrsim \frac{2}{N}\frac{m_*}{\gamma}$, which lies below the corresponding two-step mechanism threshold $\omega_{\rm BW} \gtrsim \frac{1}{2(\sqrt{N}-1)}\frac{m_*}{\gamma}$, with γ being the projectile Lorentz factor. An example is shown in Fig. 3.10, where a 17.5 GeV electron [19] collides with an intense soft VUV pulse [89]. Below $\omega_{\rm BW} \approx 18\,\text{eV}$, two-photon pair creation is possible via the direct mechanism only, which can be measured separately at VUV intensities $\sim 10^{13}\,\text{W/cm}^2$ ($\xi = 10^{-4}$). In this region, the two-step mechanism requiring an additional photon is strongly suppressed, rendering the direct process accessible to observation. Above $\omega \approx 18\,\text{eV}$, the resonance condition can be fulfilled by the $N = 2$ channel, and it becomes a two-step process.

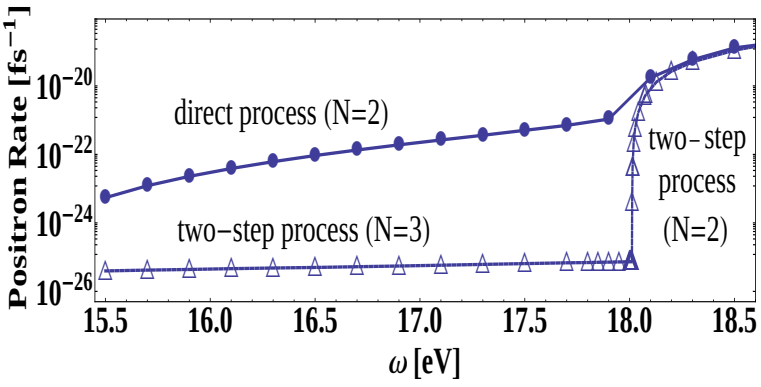

Figure 3.10: Laser frequency dependence of the pair creation rate in the head-on collision of a VUV pulse ($\xi = 10^{-4}$) with a 17.5 GeV electron. Shown are the separate contributions from the direct (circles) and two-step (triangles) processes whose sum yields the total rate.

3.3.4 Overall picture and all-optical setup

The SLAC experiment relied on the high-energy electron beam from a large-scale linear accelerator. Nowadays, corresponding pair creation studies could be performed with compact laser wakefield accelerators producing few-GeV electron beams [90]. Assuming a laser-accelerated 5 GeV electron colliding with a second optical laser pulse of intensity $\sim 10^{20}\,\mathrm{W/cm^2}$, an observable pair creation rate of $\sim 10^5\,\mathrm{s}^{-1}$ in the nonperturbative regime $\xi \approx 3$ results [91]. A similar rate can be achieved by combining a 2 GeV electron beam and a $\sim 10^{21}\,\mathrm{W/cm^2}$ laser in a quasi-static regime $\xi \approx 8$. At the envisaged high-power ($\sim 10^{25}\,\mathrm{W/cm^2}$) facility ELI [18], comparable Schwinger tunneling rates can be expected for $p^0 \sim 10\,\mathrm{MeV}$ already. Another all-optical scheme for pair creation in two laser beams employs a seed electron being accelerated directly by the fields [72]. Fig. 3.11 provides an overview of our results on the total pair production rates in various interaction regimes.

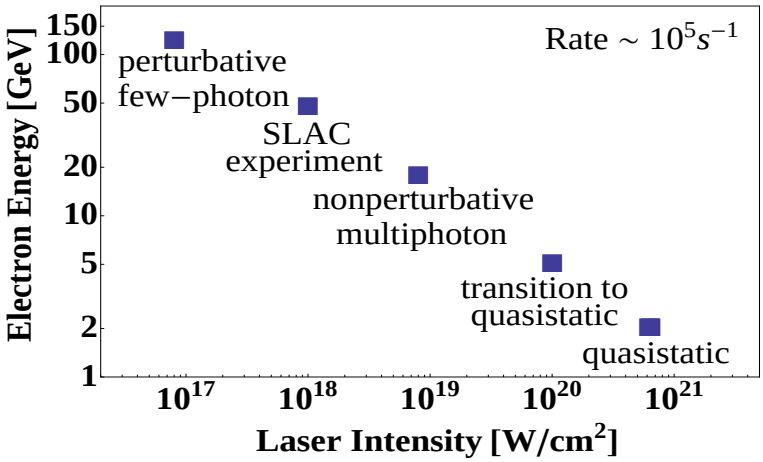

Figure 3.11: Relation of the optical (527 nm) laser intensity and the electron energy to give an observable positron rate $\sim 10^5\,\mathrm{s}^{-1}$ in the lab frame. The pair creation mechanism is changing from the perturbative few-photon to the nonperturbative quasistatic regime, as indicated.

3.4 Conclusions

In this chapter, a complete QED treatment of multi-photon trident pair creation in electron-laser collisions was presented. A regularization method was developed for the resonance problem. Based on that, the direct process and the two-step process could be treated in a unified manner. Numerical calculations have reproduced the results of the SLAC experiment [27], and furthermore identified nonperturbative QED signatures in the intensity dependence of the total rate. An experimental condition was proposed for a clean separation of the underlying production processes in the perturbative regime. Further experiments probing the transition to the fully nonperturbative (quasi-static) domain, could make use of the relativistic electrons from XFEL beamlines, or compact laser accelerators.

Chapter 4

Single-photon pair annihilation in high-density environments

4.1 Introduction to pair annihilation into photons

Electron-positron annihilation is a fundamental process. When an electron and a positron collide in free space, the energy-momentum conservation requires that the annihilation takes place with the emission of at least two photons. Typically, the two-photon process is the main annihilation channel, that reads

$$e^+ + e^- \to \gamma + \gamma' \,. \tag{4.1}$$

The rate of (4.1) in the low and high energy limit are [81]

$$R = \begin{cases} \frac{\pi\alpha^2}{m^2 V} \,, & \text{for } E - m \ll m \,, \\ \frac{\pi\alpha^2}{mEV}(\ln\frac{2E}{m} - 1) \,, & \text{for } E \gg m \,, \end{cases} \tag{4.2}$$

where E is the energy of the electron in the positron rest frame, and V denotes the interaction volume. Nevertheless, higher-order processes can become important in some cases. For example, in an ortho-positronium ($S = 1$), where the electron and positron have parallel spins, the leading mode of decay is via three-photon emission [92]. As a result, it has a lifetime three orders longer than a para-positronium ($S = 0$) [93], which allows the two-photon annihilation. The study of these binary annihilations (involving one electron and one positron) lays the foundation for several applications, like Positron Emission Tomography (PET) and Positron annihilation spectroscopy (PAS). It is also used as a method of measuring the Fermi surface and band structure in metals [94].

An e^+e^- annihilation with a single photon emission is possible in the presence of an additional particle or an external field which can absorb the recoil momentum. The field has been taken as a nuclear Coulomb field [95], a magnetic field [96] and a laser field [45]. In this chapter, we consider the e^+e^- single-photon annihilation in the presence of a second (spectator) electron:

$$e^+e^- + e \to e' + \gamma \,. \tag{4.3}$$

The spectator particle could equally well be a positron; the physical observational quantities, such as the interaction rate and the γ photon distribution, are the same. Under conventional conditions, (4.3) is a rather weak process. The calculations for a positronium ion (Ps^-) has found that the rate ratio R_{1to2} of the single-photon process over the two-photon process is of the order of 10^{-10} [97]. This low ratio is mainly due to the low densities of the samples under study.

However, in recent years, extremely dense e^+e^- samples are being investigated, motivated by experimental developments on laser-solid interactions and trapping techniques. By colliding a very intense focused laser pulse on a heavy metal foil, copious amounts of electrons and positrons with MeV energy and high density ($\rho \sim 10^{16}\,\mathrm{cm}^{-3}$) have been produced [30] and a further increase in density has been predicted ($\rho \sim 10^{22}\,\mathrm{cm}^{-3}$) [31]. This will allow laboratory studies on relativistic e^+e^- plasmas which are of intense interest in many aspects of astrophysics, such as the supernova explosion [98], the early universe [99], magnetars [100], gamma-ray bursts [101], and the center of our galaxy [102]. Cold e^+e^- samples of high quality can also be stored in traps, which hold prospects for the generation of a purely leptonic Bose-Einstein condensate [34] and a γ-ray annihilation laser [33]. Meanwhile, theoreticians study also ultrarelativistic e^+e^- plasmas with density higher than $10^{30}\,\mathrm{cm}^{-3}$ [32, 103]. In these high-density environments, the multi-particle correlation effect is prominent, since the neighboring particles can be within a Compton wavelength (λ_c) of each other ($\lambda_c^{-3} \approx 1.7 \times 10^{31}\,\mathrm{cm}^{-3}$). Moreover, it has been found recently that triple interactions such as (4.3) play a crucial role in equilibration dynamics of e^+e^- plasmas [104], but only approximate formula for total triple rates were used in these studies.

Here we present a full QED calculation of reaction (4.3) and discuss its properties in detail. Total single-photon annihilation rates in relativistic e^+e^- plasmas are given in the end.

4.2 Matrix element and rate value for single-photon annihilation

The single-photon electron-positron triple annihilation can be calculated by rules of ordinary QED. However, since eight diagrams need to be included in the leading order, the calculation is rather complicated. For this reason, only four diagrams (channel 1 and channel 2 in Fig. 4.2 were considered in the first studies [105] of the Ps^- decay into a single photon.

Here we develop an alternative approach to the problem by using the methods from laser-dressed QED. The laser field is taken to be very weak, and thus the processes with more than one photon are suppressed. At the end, the amplitude of the field has to be properly normalized by the replacement $a \to \sqrt{\frac{4\pi}{\omega V}}$ to describe a photon mode from the quantized radiation field, as deduced in Eq. (3.22) (see chapter 101 in [106] for a similar connection in the case of Compton scattering). Then the process may be treated by two Furry-Feynman diagrams only. This not only diminishes the number of the diagrams

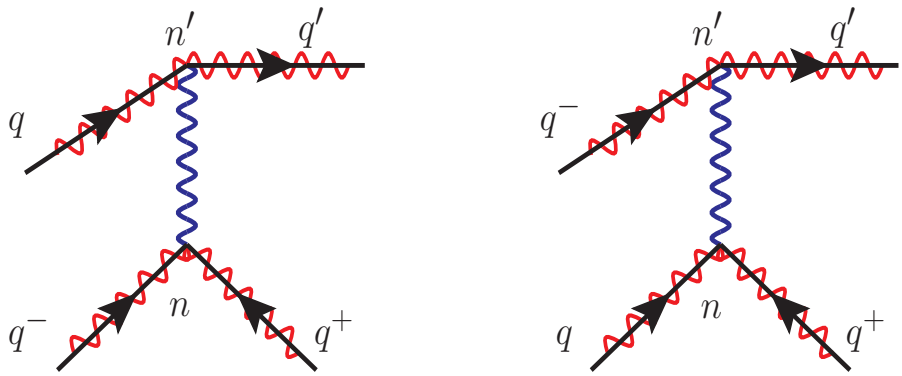

Figure 4.1: Furry-Feynman diagrams of electron-positron triple annihilation. The zigzag-lines represent the exact lepton wave-functions in a laser field (Dirac-Volkov states [37]) and are labeled by the laser-dressed particle momenta. In the left diagram, the electron and the positron with dressed momenta q^- and q^+ annihilate to n photons with the emission of an intermediate photon. It scatters the spectator electron with dressed momentum q to q', which leads to the emission of n' photons. The corresponding exchange diagram is shown on the right. Since the field intensity is taken to be very weak, the laser-dressed momenta are in effect equal to their field-free correspondences, and the processes with more than one photon emission are suppressed. Therefore, there is in total $N = n+n' = 1$ emitted photon, and eight leading-order diagrams arise in the expansion of the ordinary Feynman diagrams of external-field-free QED, shown in Fig. 4.2. Also, since only the single-photon process is taken into account, the intermediate photon is always off-shell.

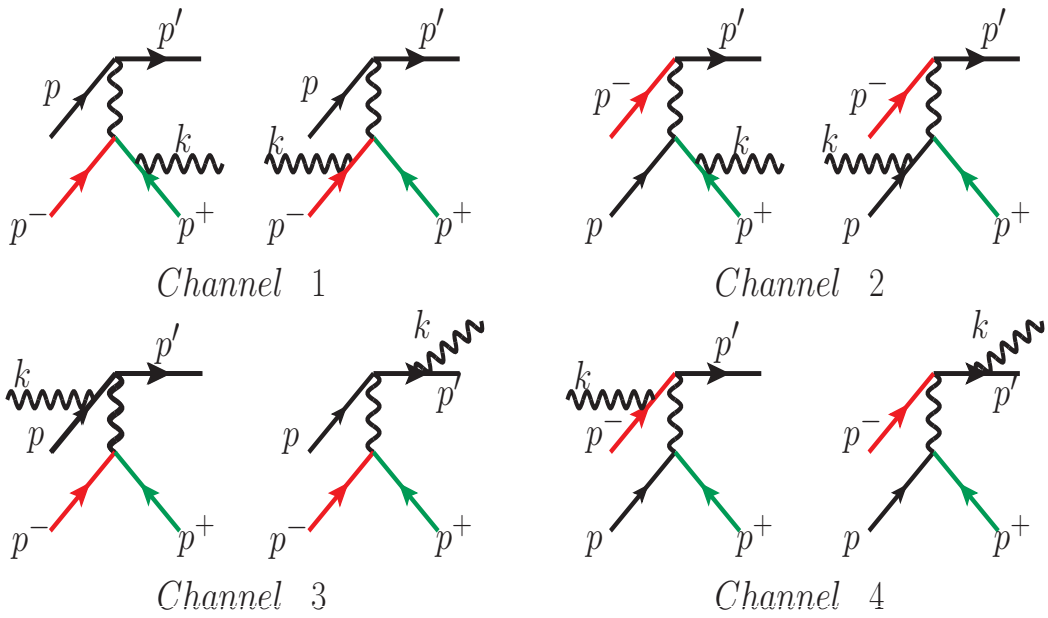

Figure 4.2: Feynman diagrams of single-photon electron-positron triple annihilation $e^+e^- + e \to e' + \gamma$. The external lines are marked by the particle momenta, that are the momentum p^+ of the positron, the two momenta p^-, p of the incoming electrons, the momentum p' of the outgoing electron, and the momentum k of the emitted photon. For the sake of later discussions, the diagrams are grouped into four channels. Channel 1 and channel 2 are different by an exchange of the two identical electrons in the initial state, as well as channel 3 and channel 4. The sum of amplitudes of channel 1 (2) and channel 3 (4) equals the amplitude of the left (right) diagram in Fig. 4.2 when the latter is normalized properly in the low-field-intensity limit.

formally, but actually reduces the work in implementing the analytical derivations and programmings. Moreover, the method also indicates that the eight diagrams can be grouped into four channels. Based on this classification, the contributions from various channels are investigated in detail. It is worthy to mention that, since only a single-photon process is considered in this chapter, there is no resonance problem appearing here.

The Furry-Feynman diagrams of the electron-positron triple annihilation and the ordinary Feynman diagrams of the single-photon electron-positron triple annihilation are depicted in Fig. 4.1 and Fig. 4.2. It is the reverse process of the (single-photon) trident electron-positron pair production, clearly seen as compared with Fig. 3.1 and Fig. 3.2. Here for the sake of clearness, the scattering matrix element and the rate value are presented in a brief manner. Fig. 4.2 accounts for the leading contributions in the usual QED expansion with respect to the fine-structure constant. Accordingly, the total scattering amplitude is

$$\begin{aligned} S_{fi} =& i2(2\pi)^5\alpha\delta^4(p^+ + p^- + p - k - p')\sqrt{\frac{2\pi m^4}{E^+E^-E_pE_{p'}\omega V^5}} \\ & \times \left(\mathcal{M}(p^+, p^-, p, p') - \mathcal{M}(p^+, p, p^-, p')\right), \end{aligned} \tag{4.4}$$

where V represents the interaction volume. The Lorentz covariant quantity $\mathcal{M}(p^+, p^-, p, p')$ corresponds to the sum of channel 1 and channel 3 shown in Fig. 4.2, and adopts the form

$$\mathcal{M}(p^+, p^-, p, p') = \sum_{n=0,1} \frac{1}{(p^+ + p^- - nk)^2} M^\mu(p^+, p^-|n) M_\mu(p, p'|1-n), \tag{4.5}$$

with n being the number of photons emitted by the annihilated pair of particles, and $1-n$ being the number of photons emitted by the spectator particle. Moreover,

$$\begin{aligned} M^\mu(p^+, p^-|n) &= \bar{u}_{p^+,s^+}\{b_n\gamma^\mu - (-\frac{e\not{\epsilon}\not{k}\gamma^\mu}{2k\cdot p^+} + \frac{e\gamma^\mu\not{k}\not{\epsilon}}{2k\cdot p^-})c_n\}u_{p^-,s^-}, \\ M_\mu(p, p'|1-n) &= \bar{u}_{p',s'}\{B_{1-n}\gamma_\mu - (\frac{e\not{\epsilon}\not{k}\gamma_\mu}{2k\cdot p'} + \frac{e\gamma_\mu\not{k}\not{\epsilon}}{2k\cdot p})C_{1-n}\}u_{p,s}, \end{aligned} \tag{4.6}$$

where ϵ is the polarization four-vector of the emitted photon, and

$$\begin{aligned} & b_0 = 1, c_0 = 0, b_1 = \frac{e(\epsilon\cdot p^-)}{k\cdot p^-} - \frac{e(\epsilon\cdot p^+)}{k\cdot p^+}, c_1 = 1, \\ & B_0 = 1, C_0 = 0, B_1 = \frac{e(\epsilon\cdot p)}{k\cdot p} - \frac{e(\epsilon\cdot p')}{k\cdot p'}, C_1 = 1. \end{aligned} \tag{4.7}$$

The quantity $\mathcal{M}(p^+, p, p^-, p')$ differs from $\mathcal{M}(p^+, p^-, p, p')$ by the exchange of (p, p^-), and corresponds to the sum of channel 2 and channel 4, depicted in Fig. 4.2.

Carrying out the final particles' momentum integration and initial particles' spin averaging to the squared amplitude, as well as summing over the polarizations of the emitted photon

and dividing out the interaction time T, leads to the total rate

$$\begin{aligned} R =& \frac{1}{T}\int\frac{Vd^3p'}{(2\pi)^3}\int\frac{Vd^3k}{(2\pi)^3}\frac{1}{8}\sum_{\text{polarizations}}\sum_{\text{spins}}|S_{fi}|^2 \\ =& \frac{\alpha^2\pi m^4}{E^+E^-E_pV^2}\int\frac{d^3p'}{E_{p'}}\delta^4(p^+ + p^- + p - k - p') \\ & \int\frac{d^3k}{\omega}\sum_{\text{polarizations}}\sum_{\text{spins}}|\mathcal{M}(p^+,p^-,p,p') - \mathcal{M}(p^+,p,p^-,p')|^2\,, \end{aligned} \tag{4.8}$$

with the statistical factor $1/8$ due to initial spin averaging. The spin sum can be converted in the usual way to trace products

$$\sum_{\text{spins}}|\mathcal{M}(p^+,p^-,p,p') - \mathcal{M}(p^+,p,p^-,p')|^2 = \sum_{n_1=0,1}\sum_{n_2=0,1}\widetilde{M}^{p^+,p^-}_{n_1n_2} + \widetilde{M}^{p^+,p}_{n_1n_2} - 2\widetilde{M}^{\mathtt{ex}}_{n_1n_2}\,, \tag{4.9}$$

where $\widetilde{M}^{p^+,p^-}_{n_1n_2}$ is a trace product

$$\begin{aligned} \widetilde{M}^{p^+,p^-}_{n_1n_2} =& \frac{1}{(p^+ + p^- - n_1k)^2}\frac{1}{(p^+ + p^- - n_2k)^2} \\ & \times Tr[\frac{\not{p}' + m}{2m}\Gamma_{\mu n_1}(p,p')\frac{\not{p} + m}{2m}\bar{\Gamma}_{\nu n_2}(p,p')] \\ & \times Tr[\frac{\not{p}^+ - m}{2m}\Gamma^{\mu}_{n_1}(p^-,p^+)\frac{\not{p}^- + m}{2m}\bar{\Gamma}^{\nu}_{n_2}(p^-,p^+)]\,, \end{aligned} \tag{4.10}$$

with

$$\begin{aligned} \Gamma^{\mu}_{n_1}(p^-,p^+) &= b_{n_1}\gamma^{\mu} - (-\frac{e\not{\epsilon}\not{k}\gamma^{\mu}}{2k\cdot p^+} + \frac{e\gamma^{\mu}\not{k}\not{\epsilon}}{2k\cdot p^-})c_{n_1}\,, \\ \Gamma_{\mu n_1}(p,p') &= B_{1-n_1}\gamma_{\mu} - (\frac{e\not{\epsilon}\not{k}\gamma_{\mu}}{2k\cdot p'} + \frac{e\gamma_{\mu}\not{k}\not{\epsilon}}{2k\cdot p})C_{1-n_1}\,, \end{aligned} \tag{4.11}$$

and $\bar{\Gamma} = \gamma^0\Gamma^{\dagger}\gamma^0$. $\widetilde{M}^{p^+,p}_{n_1n_2}$ is obtained by exchanging p^- and p in Eq. (4.10). $\widetilde{M}^{\mathtt{ex}}_{n_1n_2}$ results from the interference of the diagrams with exchanged electrons in the initial state

$$\begin{aligned} \widetilde{M}^{\mathtt{ex}}_{n_1n_2} =& \frac{1}{(p^+ + p^- - n_1k)^2}\frac{1}{(p^+ + p - n_2k)^2} \\ & \times Tr[\frac{\not{p}' + m}{2m}\Gamma_{\mu n_1}(p,p')\frac{\not{p} + m}{2m}\bar{\Gamma}_{\nu n_2}(p,p^+) \\ & \times \frac{\not{p}^+ - m}{2m}\Gamma^{\mu}_{n_1}(p^-,p^+)\frac{\not{p}^- + m}{2m}\bar{\Gamma}^{\nu}_{n_2}(p^-,p')]\,. \end{aligned} \tag{4.12}$$

The quantity, that has a direct connection with the measurements, is the number of annihilation events per time in a certain volume V, which is obtained by multiplying R with the numbers of various particles contained in this interaction region:

$$R_{\text{v}} = R\,\rho_{e^+}V\rho_{e^-}V\rho_eV = R_s\rho_{e^+}\rho_{e^-}\rho_eV\,, \tag{4.13}$$

where ρ_{e^+}, ρ_{e^-}, and ρ_e are the densities of the particles, and $R_s = V^2 R$ is a quantity which is free of volume factor. The annihilation rate of one particle, taking the positron for example, is

$$R_{e^+} = \frac{R_{\rm v}}{V\rho_{e^+}} = R_s \rho_e \rho_{e^-} \,. \tag{4.14}$$

In this chapter, we use the rate values of $R_{\rm v}$ (R_s, R_{e^+}) to quantify the single-photon annihilation process (4.3). When a comparison is drawn with the two-photon annihilation process (4.1), superscripts SP for the single-photon process and TP for the two-photon process are taken for the sake of clearness.

Low-energy limit

The relation is often drawn between the single-photon triple annihilation rate and the usual two-photon binary annihilation rate. So far, this relation has been thoroughly studied in the low-energy limit, namely that the three particles are at rest initially. In this limit, one has

$$R^{TP} = \frac{\pi\alpha^2}{m^2 V} = \frac{R_s^{TP}}{V} \,, \tag{4.15}$$

with R_s^{TP} being free of the volume factor. A comparison may be drawn via the dimensionless ratio of the numbers of annihilation events per time in the same region,

$$R_{\rm 1to2} = \frac{R_s^{SP}\rho_{e^+}\rho_{e^-}\rho_e V}{R_s^{TP}\rho_{e^+}\rho_{e^-} V} = \frac{R_s^{SP}}{R_s^{TP}}\rho_e \,. \tag{4.16}$$

In the literature the single-photon process at the low-energy limit was often considered for positronium ions. They have a length scale of the Bohr radius a_0, so that one may define a dimensionless density parameter r_e as in [105]

$$\rho_e = \frac{F^s(r_e)}{\frac{4}{3}\pi(r_e a_0)^3} = 5.185\times 10^{-8}\frac{F^s(r_e)}{\frac{4}{3}\pi r_e^3}\ [\mathrm{MeV}^3] \,, \tag{4.17}$$

where F^s accounts for environment-dependent enhancement. For example, in a negative positronium ion, made of just two electrons and a positron, F^s accounts for the enhancement of the screening cloud density at the positron over its value in the absence of the positron, and an empirical form used for correlated atomic electrons [105] is

$$F^s(r_e) \approx 1 + \frac{r_e^3 + 10}{6} \,. \tag{4.18}$$

Since free electrons (positrons) instead of bound electrons (positrons) will be considered here, we will simply take $F^s = 1$ in the following discussions. Besides, it is also often the case that the annihilation rate is given in $[\mathrm{s}^{-1}]$ [105, 107], and the transformation relation between different units is

$$\begin{aligned} R_{e^+}[\mathrm{s}^{-1}] &= 2.328\times 10^5 \frac{R_s}{(r_e r_{e^-})^3} \,, \\ R_{\rm v}[\mathrm{s}^{-1}] &= 2.328\times 10^5 \frac{R_s V_r}{(r_e r_{e^-} r_{e^+})^3} \,, \end{aligned} \tag{4.19}$$

with R_s being computed in the relativistic unit system, and V_r being a dimensionless volume factor defined by $V_r = \frac{V}{\frac{4\pi}{3}a_0^3}$.

A compact analytical expression of the single-photon annihilation rate involving only channel 1 and channel 2 was found in studying the decay of a positronium ion, assuming all the particles are initially at rest [105],

$$R^{SP} = \frac{8\alpha^3\pi^2}{3m^5V^2}\,. \tag{4.20}$$

Further numerical calculation has shown that the total rate including all the four channels is only $\frac{4}{9}$ times of this value [108], due to the interference among the diagrams. This gives

$$\frac{R_s^{SP}}{R_s^{TP}} = \frac{4}{9}\times\frac{R^{SP}V^2}{R_s^{TP}} = 0.203\ [\mathrm{MeV}^{-3}]\,. \tag{4.21}$$

Therefore,

$$R_{\mathtt{1to2}} = \frac{R_s^{SP}}{R_s^{TP}}\frac{1}{\frac{4}{3}\pi(r_e a_0)^3} = 2.53\times10^{-9}\frac{1}{r_e^3}\,. \tag{4.22}$$

It is indicated in [97] that $r_e \approx 3$ for Ps^-, and thus $R_{\mathtt{1to2}} \sim 10^{-10}$. Taking the density of a Li atom for example [105], that $\rho_e \sim (4.7\times10^{23}, 3.9\times10^{24})[\mathrm{cm}^{-3}]$, it corresponds to the value of $r_e \sim (0.75, 1.5)$, and $R_{\mathtt{1to2}}$ is in the range of $0.8\times10^{-9} \sim 6\times10^{-9}$. The signal is so weak that it is difficult to make use of the single-photon process to study, e.g., particle correlation [105], in ordinary matters.

The single-photon annihilation process beyond the low-energy limit is our interest. In the following we will present further analytical studies on the annihilation rate in various parameter regions along with the results of fully numerical calculations based on Eq. (4.8).

4.3 Beyond the low-energy limit

Without loss of generality, we consider the three leptons' collision in the center of mass frame of the pair of p^+ positron and p^- electron. In the following analytical discussions, we generally assume that this pair possesses the smaller center of mass energy, that is $(p^+ + p^-)^2 \le (p^+ + p)^2$. As shown in Fig. 4.3, the coordinate system is chosen such that the p electron moves along the positive z axis, with $p = (E_p, \mathbf{p}) = (E_p, 0, 0, p_z)$, and the e^+e^- pair collides in the xz plane, with $p^+ = (E^+, \mathbf{p}^+) = (E^+, p_x^+, 0, p_z^+)$, and $p^- = (E^-, \mathbf{p}^-) = (E^+, -p_x^+, 0, -p_z^+)$. After the triple interaction, the p electron is scattered to the final state $p' = (E_{p'}, \mathbf{p}')$, and the emitted photon's momentum is $k = (\omega, \mathbf{k})$.

In this frame, the three kinematic parameters E^+, E_p, and θ which denotes the angle between the directions of movement of the two electrons, fully determine the single-photon process. In the following, we consider first $E_p > m$ while keeping the e^+e^- pair at rest, as a first step beyond the low-energy limit.

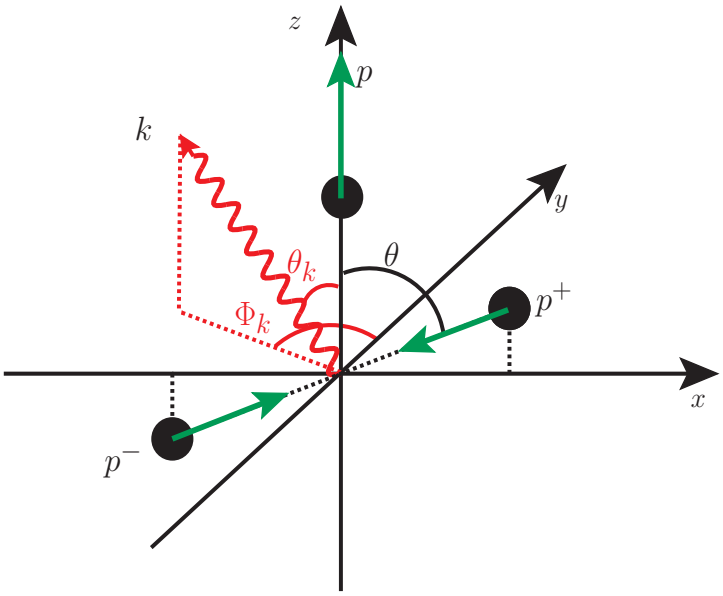

Figure 4.3: The geometry of the single-photon annihilation via electron-positron triple interaction $e^+e^- + e \to e' + \gamma$.

4.3.1 The case $E^+ = E^- = m$ and $E_p > m$

In this case, due to the rotational symmetry, the angle θ does not need to be considered. Fig. 4.4 illustrates the contributions from different reaction channels, following the categories assigned in Fig. 4.2. The dominant contribution from channel 1 as $E_p \gg m$ indicates that the interference effect is suppressed in this regime and the p^- electron is the mainly annihilated electron, which means that the emitted photon mainly comes from the pair annihilation, rather than from the radiation of the spectator electron.

For $E_p > m$ and $p^+ = p^- = (m, 0, 0, 0)$, the analytical derivation for the trace product of channel 1 can be largely simplified. The expression turns out to have a crucial dependence on the polarization of the emitted photon, as shown in the following.

Taking only the contribution from channel 1 into account, the rate is evaluated as

$$R_1 = \frac{\alpha^2 \pi m^4}{E^+ E^- E_p V^2} \int \frac{d^3p'}{E_{p'}} \int \frac{d^3k}{\omega} \delta^4(p^+ + p^- + p - k - p') \sum_{\text{polarizations}} \sum_{\text{spins}} \left| \frac{1}{(p^+ + p^- - k)^2} \bar{u}_{p^+,s^+} \left(\frac{e \not{\epsilon} \not{k} \gamma^\mu}{2m\omega} - \frac{e \gamma^\mu \not{k} \not{\epsilon}}{2m\omega} \right) u_{p^-,s^-} \bar{u}_{p',s'} \gamma_\mu u_{p,s} \right|^2 . \quad (4.23)$$

Since the system has the rotational symmetry around the z axis, the photon emission can be set in the xz plane, that means $k = \omega(1, \sin\theta_k, 0, \cos\theta_k)$, with θ_k the polar angle of the emitted photon. The integration is simplified to be $\int d^3k = 2\pi \int \omega^2 d\omega d\cos\theta_k$. Let ϵ_1 be the polarization vector in the xz plane, $\epsilon_1 = (0, \cos\theta_k, 0, -\sin\theta_k)$, and ϵ_2 orthogonal to the xz plane, $\epsilon_2 = (0, 0, 1, 0)$. We chose these particular polarization vectors for reasons that will become clear below. The sum of spins in Eq. (4.23) leads in a usual way to a

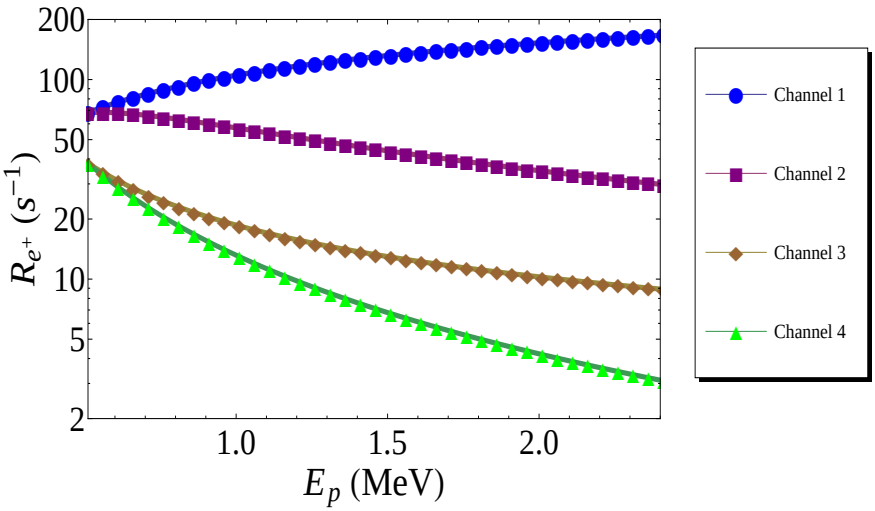

Figure 4.4: The E_p dependence of the contributions from different reaction channels, with $E^+ = E^- = m$, see the designations of channels in Fig. 4.2. The total rate contains interference terms between the various channels. However, for $E_p \gg m$, the emitted photon mainly comes from channel 1, which means that the p^+p^- pair annihilates, with the p electron acting as the spectator.

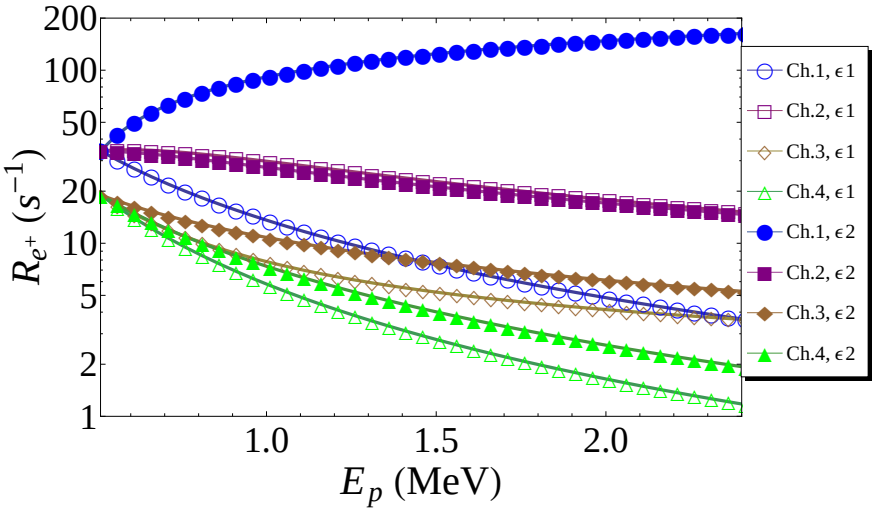

Figure 4.5: Compared to Fig. 4.4, the contribution from each channel is further divided into two parts, one with emission of ϵ_1 photon, denoted by empty plotmarkers, and the other with emission of ϵ_2 photon, denoted by filled plotmarkers of the same type and color. ϵ_1 is the photon polarization vector in the plane spanned by $\mathbf{p}$ and $\mathbf{k}$, while ϵ_2 is orthogonal to this plane. In the regime $E_p \gg m$, the emission of ϵ_2 photon dominates in channel 1, and is comparable to ϵ_1 emission in channel 2. In total, ϵ_2 emission prevails, and the radiation is linearly polarized.

trace product as in Eq. (4.10), into which substituting ϵ_1 gives

$$\mathcal{L}_1^{\epsilon_1} = \frac{2(2mE_p - \omega E_p + \omega p_z \cos\theta_k)}{m^4} \,. \tag{4.24}$$

Therefore, the rate of emitting an ϵ_1 photon is

$$\begin{aligned}
R_1^{\epsilon_1} =& \frac{2\alpha^3\pi^2 m^4}{E^+E^-E_pV^2} \int \frac{d^3p'}{E_{p'}} \int \frac{\omega^2 d\omega d\cos\theta_k}{\omega} \delta^4(p^+ + p^- + p - k - p') \left| \frac{1}{(p^+ + p^- - k)^2} \right|^2 \mathcal{L}_1^{\epsilon_1} \\
=& \frac{4\alpha^3\pi^2}{E^+E^-E_pV^2} \int 2d^4p' \delta(p'^2 - m^2) H(E_{p'}) \int \frac{\omega^2 d\omega d\cos\theta_k}{\omega} \delta^4(p^+ + p^- + p - k - p') \\
& \left| \frac{1}{4m(\omega - m)} \right|^2 (2mE_p - \omega E_p + \omega p_z \cos\theta_k) \\
=& \frac{4\alpha^3\pi^2}{E^+E^-E_pV^2} \int \frac{2\omega^2 d\omega d\cos\theta_k}{\omega} \delta((p^+ + p^- + p - k)^2 - m^2) H(2m + E_p - \omega) \\
& \frac{1}{[4m(\omega - m)]^2} (2mE_p - \omega E_p + \omega p_z \cos\theta_k) \\
=& \frac{4\alpha^3\pi^2}{E^+E^-E_pV^2} \int \frac{2\omega^2 d\omega d\cos\theta_k}{\omega} \frac{\delta(\cos\theta_k - (\frac{2m+E_p}{p_z} - \frac{2m^2+2mE_p}{\omega p_z}))}{2\omega p_z} H(2m + E_p - \omega) \\
& \frac{1}{[4m(\omega - m)]^2} (2mE_p - \omega E_p + \omega p_z \cos\theta_k) \\
=& \frac{-4\alpha^3\pi^2}{E^+E^-E_p p_z V^2} \int_{\Delta_1}^{\Delta_2} d\omega H(2m + E_p - \omega) \frac{2m(\omega - m)}{[4m(\omega - m)]^2} \,,
\end{aligned} \tag{4.25}$$

where $H(x)$ is the Heaviside step function

$$H(x) = \begin{cases} 0 \,, & \text{if } x \le 0 \,, \\ 1 \,, & \text{if } x > 0 \,, \end{cases} \tag{4.26}$$

and the ω integral limits $\Delta_{1,2}$ are determined by

$$|\cos\theta_k| = \left| \frac{2m + E_p}{p_z} - \frac{2m^2 + 2mE_p}{\omega p_z} \right| \le 1 \,, \tag{4.27}$$

which leads to $\Delta_2 \le \omega \le \Delta_1$, with

$$\begin{aligned}
\Delta_1 &= \frac{2m(E_p + m)}{2m + E_p - p_z} \,, \\
\Delta_2 &= \frac{2m(E_p + m)}{2m + E_p + p_z} \,.
\end{aligned} \tag{4.28}$$

Therefore, $m < \omega < E_p + m$ always holds, and $\omega = \frac{4m}{3}$ when $E_p = m$.

Making use of Eq. (4.28) in the integration (4.25), we get

$$R_1^{\epsilon_1} = \frac{\alpha^3\pi^2}{2mE^+E^-E_p p_z V^2} \ln\left[\frac{(E_p + p_z)(2m + E_p + p_z)}{(E_p - p_z)(2m + E_p - p_z)} \right] \,. \tag{4.29}$$

In the low-energy limit, that is $E_p = m$, this gives

$$R_1^{\epsilon_1} = \frac{4\alpha^3\pi^2}{3m^2E^+E^-E_pV^2} = \frac{4\alpha^3\pi^2}{3m^5V^2}\,. \tag{4.30}$$

For the other polarization ϵ_2, we obtain $R_1^{\epsilon_2} = R_1^{\epsilon_1}$ in the low-energy limit [see also Fig. 4.5]. Hence, the sole contribution from channel 1, i. e., $R_1^{\epsilon_1} + R_1^{\epsilon_2}$, gives the same value R^{SP} which was given in Eq. (4.20). The latter represents the contribution from the coherent sum of channels 1 and 2, however. This shows that the interference between the two channels is destructive and reduces the rate by a factor of 2. This is also confirmed by our numerical calculations, which show further that the total rate stemming from the coherent sum of all the four channels agrees with the result of Ref. [108] where an additional reduction by a factor of $\frac{4}{9}$ due to interference was found.

Now we return to channel 1 and consider its high-energy limit, that is $E_p \to \infty$. In this case, Eq. (4.29) yields

$$R_1^{\epsilon_1} \sim \frac{\alpha^3\pi^2}{2mE^+E^-E_p^2V^2}(\ln 4 + 3\ln\frac{E_p}{m})\,, \tag{4.31}$$

which decreases fast with the increase of E_p.

The situation of emitting an ϵ_2 photon is drastically different from the above ϵ_1 photon emission in the high-energy regime. Substituting ϵ_2 into the trace product yields

$$\mathcal{L}_1^{\epsilon_2} = \frac{2[(2mE_p - \omega E_p + \omega p_z\cos\theta_k) + p_z^2(1-\cos(2\theta_k))]}{m^4}\,. \tag{4.32}$$

The corresponding rate is

$$\begin{aligned}
R_1^{\epsilon_2} =& \frac{2\alpha^3\pi^2m^4}{E^+E^-E_pV^2}\int\frac{d^3p'}{E_{p'}}\int\frac{\omega^2\sin\theta_k d\omega d\theta_k}{\omega}\delta^4(p^+ + p^- + p - k - p')\left|\frac{1}{(p^+ + p^- - k)^2}\right|^2\mathcal{L}_1^{\epsilon_2}\\
=& R_1^{\epsilon_1} + \frac{2\alpha^3\pi^2m^4}{E^+E^-E_pV^2}\int\frac{d^3p'}{E_{p'}}\int\frac{\omega^2\sin\theta_k d\omega d\theta_k}{\omega}\delta^4(p^+ + p^- + p - k - p')\\
&\left|\frac{1}{(p^+ + p^- - k)^2}\right|^2\frac{2p_z^2(1-\cos(2\theta_k))}{m^4}\\
=& R_1^{\epsilon_1} + \frac{8\alpha^3\pi^2p_z}{E^+E^-E_pV^2}\int_{\Delta_2}^{\Delta_1}d\omega\frac{(-5m^2-4mE_p) - 4(\frac{m^2(m+E_p)^2}{\omega^2} - \frac{m(2m+E_p)(m+E_p)}{\omega})}{p_z^2[4m(\omega-m)]^2}\\
=& R_1^{\epsilon_1} + \frac{8\alpha^3\pi^2p_z}{E^+E^-E_pV^2}\int_{\Delta_2-m}^{\Delta_1-m}d\delta\omega\frac{(-5m^2-4mE_p) - 4(\frac{m^2(m+E_p)^2}{m^2(1+\delta\omega/m)^2} - \frac{m(2m+E_p)(m+E_p)}{m(1+\delta\omega/m)})}{p_z^2(4m\delta\omega)^2}\\
\cong& R_1^{\epsilon_1} + \frac{8\alpha^3\pi^2p_z}{E^+E^-E_pV^2}\int_{\Delta_2-m}^{\Delta_1-m}d\delta\omega\frac{-m^2 + 4\frac{\delta\omega}{m}E_p(E_p+m)}{p_z^2(4m\delta\omega)^2}\\
=& R_1^{\epsilon_1} + \frac{\alpha^3\pi^2}{2E^+E^-E_pp_zV^2}(\frac{1}{\Delta_1-m} - \frac{1}{\Delta_2-m})\\
&+ \frac{2\alpha^3\pi^2E_p(E_p+m)}{m^3E^+E^-E_pp_zV^2}\ln\frac{\Delta_1-m}{\Delta_2-m}\,,
\end{aligned} \tag{4.33}$$

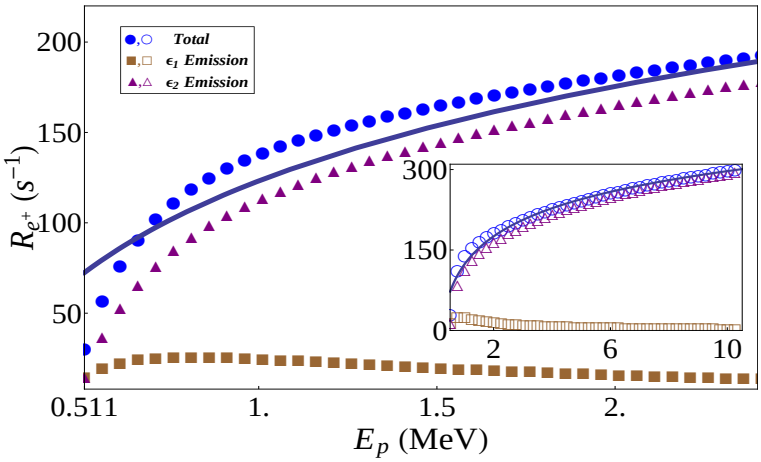

Figure 4.6: The total rate of the single-photon electron-positron annihilation, as well as its two components of the ϵ_1 and the ϵ_2 photon emissions, is shown for different E_p with $E^+ = E^- = m$, calculated by including all the Feynman diagrams in Fig. 4.2. The inset shows a larger region of E_p. The blue line is a logarithmic function fitting to the total rate $R_{e^+} \approx 25.17(3 \ln \frac{E_p}{m} + 2.88)$, which matches the data very well when $E_p > 5\,\mathrm{MeV}$. Due to the interference of diagrams with exchanged electrons in the initial state, the annihilation rate drops notably as $E_p \to m$. It can be clearly seen that, for large E_p, the radiation is linearly polarized along the ϵ_2 direction.

where $\Delta_{1,2}$ are the same as in Eq. (4.28), and an approximation $\delta\omega = \omega - m \ll m$ has been used, since the integrand indicates that the frequency distribution of the emitted photon has a second order divergence at $\delta\omega \sim 0$. In the high-energy limit, Eq. (4.33) takes the form

$$R_1^{\epsilon_2} \sim \frac{\alpha^3\pi^2}{2mE^+E^-E_p^2V^2} \ln\frac{4E_p^3}{m^3} + \frac{2\alpha^3\pi^2}{m^3E^+E^-V^2}(\ln\frac{4E_p^3}{m^3} - 1)\,, \tag{4.34}$$

where the first term is the same as $R_1^{\epsilon_1}$, and the second term presents a logarithmic increase with E_p.

Fig. 4.5 illustrates the numerical calculation of contributions from different channels and different emitted photon polarizations, based on Eq. (4.8). For channel 1, a logarithmic dependence on E_p is found for ϵ_2 polarization, as expected from formula (4.34), in the regime $E_p \gg m$. For channel 2, where the p^+p pair annihilates into one photon with the p^- electron being the spectator, the two polarizations have the same share of weight.

The total rate as well as polarization-resolved rates are plotted in Fig. 4.6. For $E_p \sim m$, the interference of diagrams with exchanged initial electrons becomes important, and the total rate is notably reduced. For $E_p \gg m$, the effect of the interference is suppressed, since the contributions from all channels decrease, except for channel 1 with ϵ_2 photon emission. A logarithmic law describes the total rate very well in this regime.

For large E_p, the frequency distribution of the emitted photon can be attributed to

$$\frac{dR_1^{\epsilon_2}}{d\omega} \cong \frac{8\alpha^3\pi^2 p_z}{E^+E^-E_pV^2}\frac{m^2}{p_z^2[4m(\omega-m)]^2} \propto \frac{1}{E_p^2(\omega-m)^2}\,, \tag{4.35}$$

which has a sharp peak at the smallest possible value of ω,

$$\omega = \Delta_2 \cong m(1+\frac{m^2}{4E_p^2})\,. \tag{4.36}$$

Therefore, instead of emitting a photon with $\omega = \frac{4m}{3}$ as in the low-energy limit, the photon mainly possesses an energy $\sim m$, similar to that from p^+p^- two photon annihilation.

When $E_p \gg m$, the angular distribution function of the emitted photon takes the form

$$\begin{aligned}
\frac{dR_1^{\epsilon_2}}{d\theta_k} =& \frac{2\alpha^3\pi^2m^4}{E^+E^-E_pV^2}\int\frac{d^3p'}{E_{p'}}\int\frac{\omega^2\sin\theta_k d\omega}{\omega}\delta^4(p^+ + p^- + p - k - p') \\
& \left|\frac{1}{(p^+ + p^- - k)^2}\right|^2 \frac{2[(2mE_p - \omega E_p + \omega p_z\cos\theta_k) + p_z^2(1-\cos(2\theta_k))]}{m^4} \\
=& \frac{2\alpha^3\pi^2m^4}{E^+E^-E_pV^2}\int\frac{2\omega^2\sin\theta_k d\omega}{2\omega(2m+E_p-p_z\cos\theta_k)}\delta(\omega - \frac{2m(m+E_p)}{2m+E_p-p_z\cos\theta_k}) \\
& \frac{1}{[4m(\omega-m)]^2}\frac{2[(2mE_p - \omega E_p + \omega p_z\cos\theta_k) + p_z^2(1-\cos(2\theta_k))]}{m^4} \\
\cong& \frac{\alpha^3\pi^2E_p\sin\theta_k(1-\cos\theta_k)(1-\cos^2\theta_k)}{m^3E^+E^-V^2(2m+E_p-p_z\cos\theta_k)(1+\cos\theta_k-\frac{m^2}{2E_p^2}\cos\theta_k)^2}\,,
\end{aligned} \tag{4.37}$$

where only the approximation $p_z \cong E_p(1-\frac{m^2}{2E_p^2})$ was made use of in the last step. The good match of Eq. (4.37) with numerical results is illustrated in Fig. 4.7. It is found that the photon is emitted almost parallel to the counter direction of the spectator electron, but is inhibited along the exact counter direction. This is in contrast with what was found in the low-energy limit, where the photon is isotropically produced.

The peak position of the angular distribution may be derived from Eq. (4.37) by finding its maximum via taking the derivative with respect to θ_k. As can be seen from Fig. 4.8, it gets closer to 180°, that the counter direction of p electron's movement, with larger E_p.

Let us give a brief summary of the photon emission. In the case $E_p \gg m$ and $E^+ = E^- = m$, the wave vectors of the emitted photon hold the rotational symmetry around the direction of the spectator electron's movement, effectively. The radiation is actually linearly polarized, with polarization orthogonal to the plane that the momenta of the spectator electron and the emitted photon span. Besides, the frequency and the angular distribution of the emitted photon are peaked at $\omega \approx m$ and $\theta_k \approx 180°$, with a sharp dip at $\theta_k = 180°$.

As E_p increases, the mass square of the intermediate photon approaches its low boundary

$$mass^2_{virtual} = (p^+ + p^- - k)^2 \cong \frac{m^4}{E_p^2}\,. \tag{4.38}$$

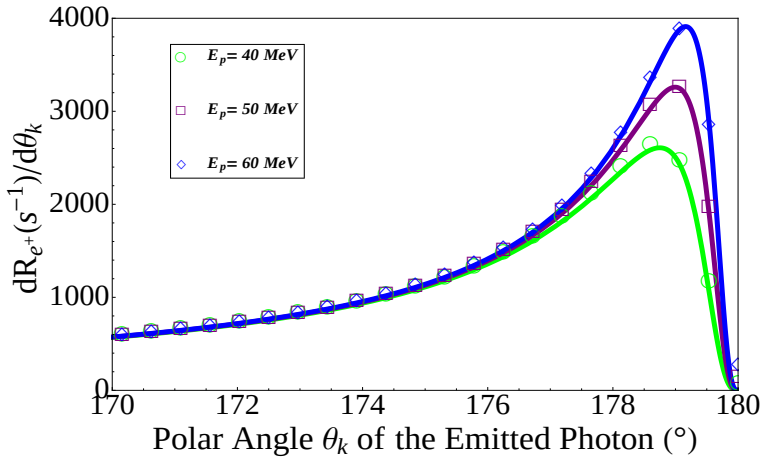

Figure 4.7: The angular distribution of the emitted photon for $E_p \gg m$ and $E^+ = E^- = m$. The emission is peaked closely below $\theta_k = 180°$ with typical energy $\omega \approx m$ in main, but it has a sharp dip exactly at $\theta_k = 180°$ which is the direction parallel to the counter direction of the p electron.

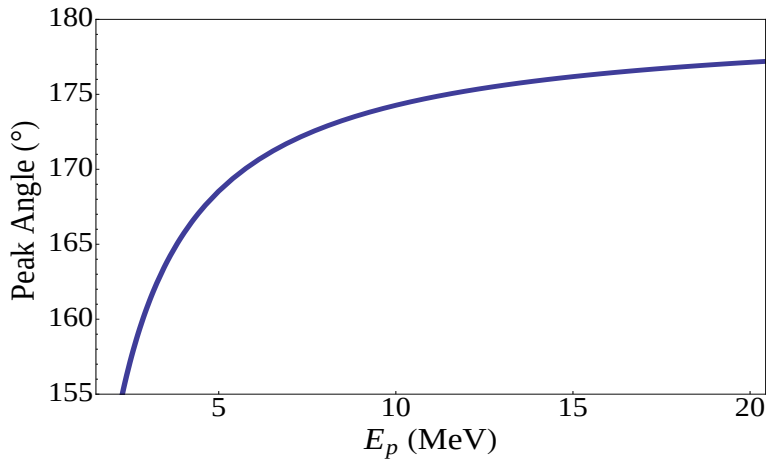

Figure 4.8: The E_p dependence of the polar angle where the peak of the angular distribution of photon emission lies, with $E^+ = E^- = m$. The peak angle increases towards 180° with the increase of E_p.

The larger E_p is, the closer the intermediate photon approaches the mass shell, which means the more 'real' it is. If the process is considered approximately as composed of two successive processes, namely the two-photon binary annihilation followed by the reverse process of electron radiation, then the features related to the emitted photon can have an intuitive explanation. The two-photon annihilation of an electron and a positron at rest suggests naturally that the emitted photon satisfies $\omega \approx m$. The radiation of a relativistic electron is mainly along its movement direction $\hat{\mathbf{p}}$. Therefore, in the reverse process, the electron effectively absorbs the virtual photon with wave vector $\mathbf{k}_{\mathtt{vir}}$ almost parallel to $\hat{\mathbf{p}}$. Due to $\mathbf{k}_{\mathtt{vir}} + \mathbf{k} = 0$ determined by the annihilation process, $\mathbf{k}$ should mainly lie in the direction of $-\hat{\mathbf{p}}$.

The consideration of the low-energy limit with $E^+ = E^- = m$ in this section has allowed us to gain detailed insights and an intuitive understanding of the single-photon annihilation process. However, we should recall that the plane-wave approximation of electron and positron states at very low energies is not a very good description since it ignores Coulomb effects which can be sizeable in this regime [109]. In the next section we therefore consider the more general case of $E^+ = E^- \geq m$. Here the plane-wave description is appropriate for particle velocities $v_\pm \gtrsim 2\pi\alpha$ corresponding to $E^\pm \gtrsim 1.001m$.

4.3.2 The case $E^+ = E^- > m$ and $E_p > E^+$

In the regime $E^+ - m \ll m$, and $E_p \gg E^+$, we can have some preliminary guesses induced from above discussions. For example, the photon is mainly produced by the annihilation of the p^+p^- pair, with the p electron being scattered radiationlessly. This is verified by complete numerical calculations, shown in the left two plots in Fig. 4.9. Further calculations also find that the emitted photon acquires $\omega \sim E^+$, and $\mathbf{k}$ almost parallel to $-\hat{\mathbf{p}}$ with a sharp drop along $-\hat{\mathbf{p}}$. Besides, the rate has only a slight dependence on θ: it is almost isotropic but has a suppression about $\theta = 90°$, as expected from the approximate two-step picture, since the two-photon annihilation has the highest emission along the directions of $\pm\hat{\mathbf{p}}^+$, when $E^+ > m$.

The similarity with the case $E^+ = E^- = m$ implies that some analytical approach can be followed from the previous experience. It was found in Eq. (4.33) that only the term

$$l = \frac{2p_z^2(1 - \cos(2\theta_k))}{m^4} \tag{4.39}$$

from the trace product matters as $E_p \to \infty$, and determines the logarithmic dependence of the rate on E_p. In the regime $E^+ - m \ll m$ and $E_p \gg E^+$, we therefore consider the corresponding term in the trace product which reduces to Eq. (4.39) in the limit $E^+ \to m$ and $\theta \to 0°$. Applying the relativistic approximation $p^2 = p'^2 \approx 0$, this term can be found for the photon emission in the xz plane in a concise form

$$l' = \frac{2E^{+2}p_z^2(1 - \cos(2\theta_k))}{m^4(E^{+2} - \cos^2(\theta \pm \theta_k)\mathbf{p}^{+2})}\,, \tag{4.40}$$

where the minus sign corresponds to $\phi_k = 0°$, and plus corresponds to $\phi_k = 180°$. Since $E^{+2} - \cos^2(\theta \pm \theta_k)\mathbf{p}^{+2} \geq m^2$, this modification on the denominator should not change the

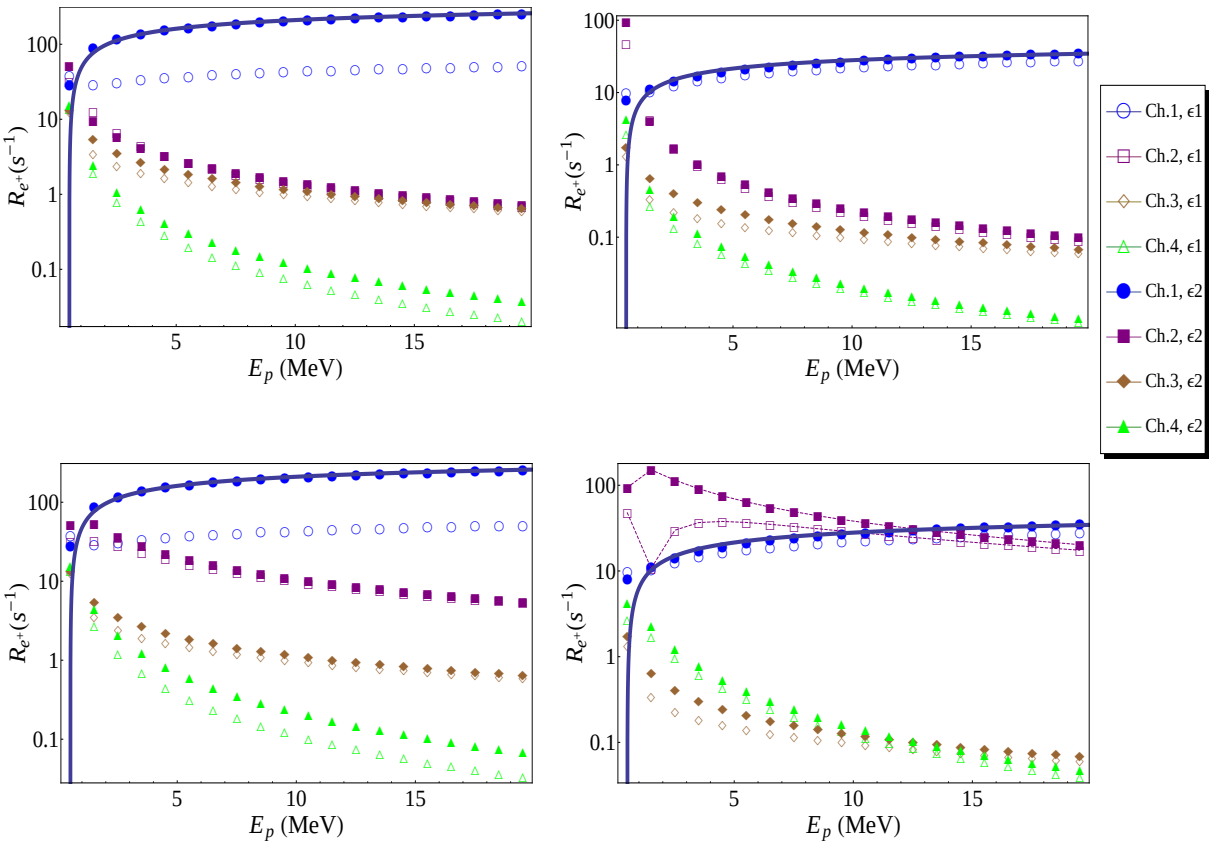

Figure 4.9: E_p dependence of the polarization-resolved rates of various channels for the parameters: (left,up) $E^+ = E^- = 0.561\,\mathrm{MeV}$, $\theta = 0°$; (left,down) $E^+ = E^- = 0.561\,\mathrm{MeV}$, $\theta = 180°$; (right,up) $E^+ = E^- = 1.011\,\mathrm{MeV}$, $\theta = 0°$; (right,down) $E^+ = E^- = 1.011\,\mathrm{MeV}$, $\theta = 180°$. ϵ_1 is the photon polarization vector in the plane spanned by $\mathbf{p}$ and $\mathbf{k}$, while ϵ_2 is orthogonal to this plane. For $E^+ - m \ll m$ in the left figures, the situation is similar to that for $E^+ = m$ (see Fig. 4.5): the ϵ_2 photon emission is still considerably larger than the ϵ_1 emission, and the angle θ between the two electrons does not have notable influence. In contrast, for the case of larger E^+ in the right figures, the ϵ_1 photon emission from channel 1 is not suppressed, and there is a remarkable dependence on θ: for $E^+ = 1.011\,\mathrm{MeV}$, $\theta = 0°$, channel 1 is the main contributor, but for $\theta = 180°$, channel 2 is significantly enhanced. The blue line shows a good match of the logarithmic fitting to the ϵ_2 photon emission of channel 1 when E_p is large, for all the four cases.

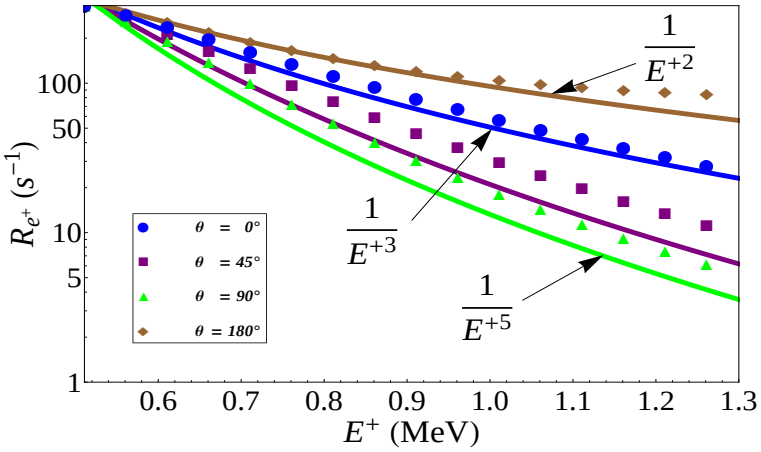

Figure 4.10: E^+ dependence of the total rates including all the channels for a fixed $E_p = 14\,\text{MeV}$ and various θ. The blue curve is the $f(E^+)|_\theta = \beta \frac{1}{E^{+3}(E^{+2}-\cos^2\theta \mathbf{p}^{+2})}$ fitting (see Eq. (4.43)) to the data of $\theta = 0°$, with the fitting parameter β. The purple and green curves are the functions $f(E^+)|_{45°}$ and $f(E^+)|_{90°}$, with the same β value, where it is shown that the function underestimates the total rate. For the data of $\theta = 180°$, a $\frac{1}{E^{+2}}$ dependence is found, which is very different from the $\frac{1}{E^{+3}}$ behavior indicated by Eq. (4.43).

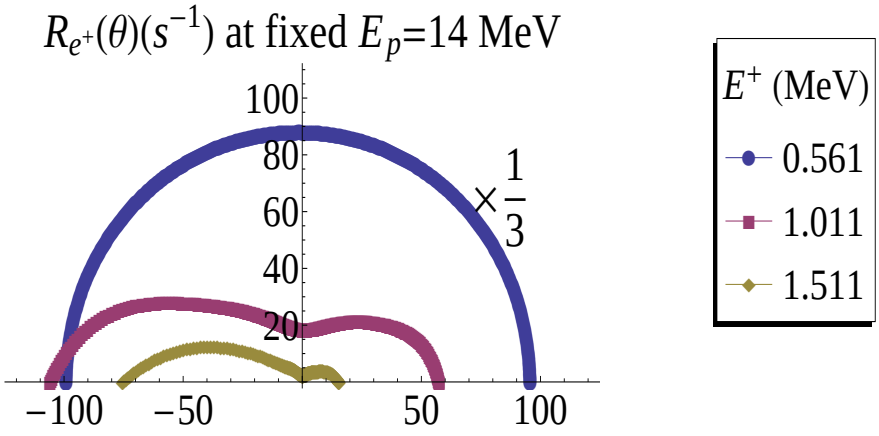

Figure 4.11: The single-photon annihilation rate in a polar plot, that is $(\theta, R_{e^+}(\theta))$, for a fixed $E_p = 14\,\text{MeV}$ and various E^+. For $E^+ = 0.561\text{MeV}$, the rate has been reduced by a factor of 1/3 to make it fit into the plot. In this case, the rate dependence on θ is almost isotropic, with a slight suppression at $\theta \approx 90°$. For larger E^+, the suppression is more notable, and the angular dependence has a significant enhancement as $\theta \to 180°$. Compared with the (right,down) plot in Fig. 4.9, it is clear that for $E_p = 14\text{MeV}$, $E^+ = 1.011\text{MeV}$, the surplus of the rate for $\theta = 180°$ over that for $\theta = 0°$ comes from channel 2, as both channels now have almost the same amount of contribution.

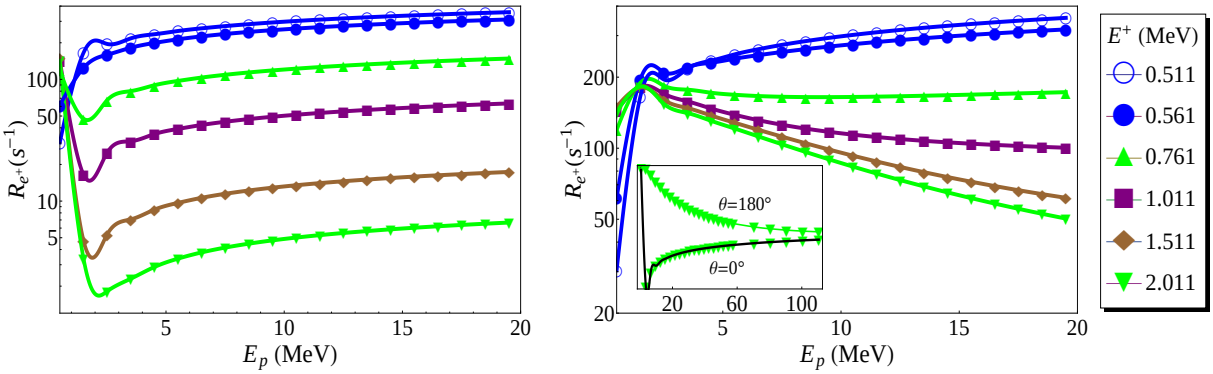

Figure 4.12: The total rate dependence on E_p for various E^+ and (left) $\theta = 0°$, where the rate increases with the increase of E_p; (right) $\theta = 180°$, where for large E^+, the rate is much larger than their $\theta = 0°$ correspondence, and decreases with the increase of E_p. The inset shows that the θ-dependence diminishes as E_p increases. Notice that for $E^+ = 2.011$MeV, the convergence is reached when E_p is as large as 100 MeV.

trend that the photon angular distribution peaks around $\theta_k \sim 180°$. Therefore, it can be simplified to

$$l' \approx \frac{2E^{+2}p_z^2(1-\cos(2\theta_k))}{m^4(E^{+2}-\cos^2\theta\mathbf{p}^{+2})}\,. \tag{4.41}$$

Based on the expression (4.41), we consider the rate dependence on E^+

$$\begin{aligned}
\frac{dR_1^{\epsilon_2}}{d\phi_k}\Big|_{\phi_k=0°,180°} \cong & \frac{\alpha^3\pi m^4}{E^+E^-E_pV^2}\frac{E^{+2}}{(E^{+2}-\cos^2\theta\mathbf{p}^{+2})}\int\frac{d^3p'}{E_{p'}}\int\frac{\omega^2\sin\theta_k d\omega d\theta_k}{\omega} \\
& \delta^4(p^+ + p^- + p - k - p')\frac{1}{(p^+ + p^- - k)^4}\frac{2p_z^2(1-\cos(2\theta_k))}{m^4} \\
= & \frac{\alpha^3\pi m^4}{E^+E^-E_pV^2}\frac{E^{+2}}{(E^{+2}-\cos^2\theta\mathbf{p}^{+2})}\int\frac{2\omega^2\sin\theta_k d\omega d\theta_k}{\omega} \\
& \frac{\delta(\omega-\frac{2E^+(E^++E_p)}{|2E^++E_p-p_z\cos\theta_k|})}{2|2E^++E_p-p_z\cos\theta_k|}\frac{1}{[4E^+(\omega-E^+)]^2}\frac{2p_z^2(1-\cos(2\theta_k))}{m^4} \\
\cong & \frac{\alpha^3\pi m^4}{E^+E^-E_pV^2}\frac{E^{+2}}{(E^{+2}-\cos^2\theta\mathbf{p}^{+2})}\frac{1}{8E^{+3}}\int\frac{\sin\theta_k d\theta_k}{\omega} \\
& \frac{E_p}{(E_p+p_z\cos\theta_k)^2}\frac{2p_z^2(1-\cos(2\theta_k))}{m^4} \\
\propto & \frac{1}{E^{+3}(E^{+2}-\cos^2\theta\mathbf{p}^{+2})}\ln(\frac{E_p}{m})\,, \qquad \text{as } E_p\to\infty\,.
\end{aligned} \tag{4.42}$$

If the rotational symmetry around z axis is adopted approximately, which is the exact case when $\theta = 0°$ or $180°$, we find

$$R \sim R_1^{\epsilon_2} \propto \frac{1}{E^{+3}(E^{+2}-\cos^2\theta\mathbf{p}^{+2})}\ln(\frac{E_p}{m})\,. \tag{4.43}$$

However, Fig. 4.10 shows that Eq. (4.43) underestimates the total rate when E^+ is distinctly larger than m. Moreover, in the case $\theta = 180°$, a $\frac{1}{E^{+2}}$ dependence is found instead of $\frac{1}{E^{+3}}$ as indicated by Eq. (4.43). It is illustrated in the right plots of Fig. 4.9 that, in this regime the suppression of ϵ_1 photon emission from channel 1 is removed, and for $\theta = 180°$ the contribution from channel 2 becomes very important and even exceeds that from channel 1 in a large region.

Fig. 4.11 displays the θ angular dependence of the rate. The asymmetric structure, when E^+ is notably larger than m, mainly comes from the contribution of channel 2. The total rate dependence on E_p is plotted in Fig. 4.12, and it is emphasized that the θ angular dependence is prominent over a wide range of $E_p \gg E^+$.

4.4 Numerical results in relativistic electron-positron plasmas

Relativistic electron-positron plasmas, in which the thermal energy of the particles is on the order of or even larger than the particles' rest mass energy, can be found in astrophysical processes, such as in supernovae explosions [98], and in the strong magnetic fields around magnetars [100]. Also, prolific generation of e^+e^- pairs has been realized in the lab [30], by targeting an intense laser pulse onto a solid film. A positron density of $10^{16}\,\mathrm{cm}^{-3}$ with positron temperature $\sim 2.8\,\mathrm{MeV}$ was reported. A higher density ($\rho \sim 10^{22}\,\mathrm{cm}^{-3}$) [31] is expected to be achieved by applying stronger lasers and improving the design of the target film. Besides the relevance in astrophysics, high-density electron-positron plasmas have applications in forming high density positronium (Ps) samples, and achieving Ps Bose-Einstein condensation [34].

4.4.1 Convolution over Fermi-Dirac distribution

We consider in this section a homogeneous and isotropic relativistic electron-positron plasma in its thermal and chemical equilibrium, with equal electron and positron density (vanishing chemical potential) [32]. The distribution function of the electrons and positrons is given by the Fermi-Dirac distribution

$$n_F(E, T_p) = \frac{1}{e^{\frac{E-m}{T_p}} + 1}\,, \tag{4.44}$$

where $E - m$ gives the kinetic energy of the particle, and T_p is the plasma temperature, with the Boltzmann constant $k_B = 1$. The electron (positron) density can be obtained by

$$\rho(T_p) = g_F \int \frac{d^3p}{(2\pi)^3} n_F(E, T_p)\,, \tag{4.45}$$

where $\frac{d^3p}{(2\pi)^3}$ equals to the number of states in the momentum space d^3p per volume, and $g_F = 2$ is the number of degrees of freedom corresponding to the two spin states. The

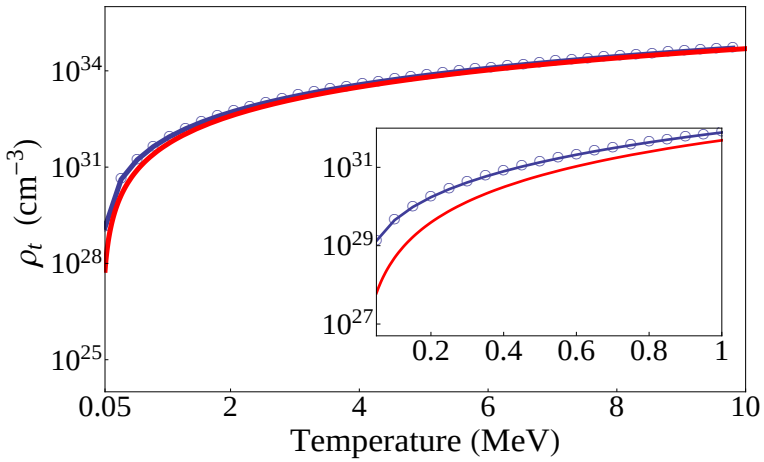

Figure 4.13: The temperature dependence of the total particle density in a relativistic electron-positron plasma. The blue line is the numerical calculation of the integration (4.45), multiplied by a factor 2 according to the 2 species in the plasma. The red line is the function $\rho_t(T_p) = 0.37\, T_p^3$. Their difference decreases fast as the temperature increases beyond the rest energy of the particle.

total particle density is $\rho_t = 2\rho$, accounting for both electrons and positrons. In Fig. 4.13, the total particle density is plotted against the temperature. It is found that for $T_p \gtrsim 1\,\mathrm{MeV}$, it is very well described by the relation

$$\rho_t(T_p) = 0.37\, T_p^3\,, \tag{4.46}$$

as was indicated for the case $E \gg m$ in Ref. [32]. Note that the units are transformed as $1\,[\mathrm{MeV}^3]{=}1.3\times 10^{32}[\mathrm{cm}^{-3}]$.

The single-photon annihilation process can be very important in relativistic electron-positron plasmas due to the high particle density there. As an estimation, let's refer to Eq. (4.16) and the discussion after. There, a density $\rho_e = 3.9\times 10^{24}\,\mathrm{cm}^{-3}$ in

$$R_{1\mathtt{to}2} = \frac{R_s^{SP}}{R_s^{TP}}\rho_e\,, \tag{4.47}$$

gave the ratio $R_{1\mathtt{to}2} = 1.4\times 10^{-8}$. The ratio is enhanced to $R_{1\mathtt{to}2}\sim 1$ in an electron-positron plasma at $T_p \approx 2.3\,\mathrm{MeV}$, where the density is $\rho \approx 3\times 10^{32}\,\mathrm{cm}^{-3}$. For this estimation, we assumed for simplicity that the low-energy limit in Eq. (4.16) still applies approximately. It is worthy to notice that in the relativistic plasmas the distance between neighboring particles can be smaller than a Compton wavelength λ_c, which corresponds to a density $\lambda_c^{-3} \approx 1.7\times 10^{31}\,\mathrm{cm}^{-3}$. Therefore, the correlation effects can be prominent.

The single-photon annihilation rate per volume in the electron-positron plasma can be obtained by substituting the density (4.45) into Eq. (4.13), dividing out the volume factor,

and integrating over the momentum space

$$R_t(T_p) = 2Sg_F^3 \int \frac{d^3p^+}{(2\pi)^3} n_F(E^+, T_p) \int \frac{d^3p^-}{(2\pi)^3} n_F(E^-, T_p) \times \int \frac{d^3p}{(2\pi)^3} n_F(E_p, T_p) R_s(p^+, p^-, p)\,, \tag{4.48}$$

where $S = \frac{1}{2}$ is the statistical factor to avoid double counting of the two electrons involved, and the factor 2 appears because there are two symmetric single-photon processes: $e^+e^- + e \to e' + \gamma$ and $e^+e^- + e^{+'} \to e^{+''} + \gamma$.

It is convenient to integrate over the energy, for example, $\int d^3p = \int |\mathbf{p}|^2 d|\mathbf{p}| d\Omega = \int |\mathbf{p}| E dE d\Omega$. Due to the three-dimensional rotational symmetry of the system, 3 variables can be fixed. We choose that $\mathbf{p}^+ \parallel \hat{z}$, and $\mathbf{p}^- \in (xz)$ plane. Therefore, $\theta^+ = 0$ and $\phi^+ = \phi^- = 0$. The calculation can be performed by

$$R_t(T_p) = 2Sg_F^3 \frac{8\pi^2}{(2\pi)^9} \int |\mathbf{p}^+| E^+ dE^+ n_F(E^+, T_p) \int |\mathbf{p}^-| E^- dE^- \sin\theta^- d\theta^- n_F(E^-, T_p) \times \int |\mathbf{p}| E_p dE_p \sin\theta d\theta d\phi\, n_F(E_p, T_p) R_s(E^+, E^-, \theta^-, E_p, \theta, \phi)\,. \tag{4.49}$$

The computation is time consuming, mainly due to the calculation of R_s. In the following, we discuss how to reduce the calculation work.

4.4.2 Calculational procedures

Instead of doing the calculation of R_s for arbitrary kinematic parameters, it can be done in a fixed reference frame, for example, the positron rest frame.

The Lorentz transformation to boost a positron with momentum $|\mathbf{p}^+|\hat{z}$ to its rest frame is

$$\begin{cases} \gamma(E^+ - \beta|\mathbf{p}^+|) = m\,, \\ \gamma(-\beta E^+ + |\mathbf{p}^+|) = 0\,, \end{cases} \tag{4.50}$$

with $\beta = \frac{|\mathbf{p}^+|}{E^+}$ and $\gamma = \frac{E^+}{m}$. The momenta of p^- and p electrons are transformed accordingly. In the following, the kinematic parameters in the boosted frame (here the positron rest frame) are indicated by the subscript b. For $R_s(E^+, E^-, \theta^-, E_p, \theta, \phi)$ in Eq. (4.49), $R_s(m, E_b^-, \theta_b^-, E_{p,b}, \theta_b, \phi_b)$ is addressed as its counterpart in the positron rest frame. Notice further that the single-photon annihilation rate only depends on three independent parameters, which together determine the kinematic configuration of the process. In the positron rest frame, these parameters are the electrons' energies E_b^-, $E_{p,b}$, and the angle θ_b^r between the directions of the boosted momenta. Therefore, we have

$$R_s(m, E_b^-, \theta_b^-, E_{p,b}, \theta_b, \phi_b) = R_s(m, E_b^-, \theta_b^r, E_{p,b}, 0, 0)\,, \tag{4.51}$$

with

$$\theta_b^r = \arccos(\sin\theta_b^- \sin\theta_b \cos\phi_b + \cos\theta_b^- \cos\theta_b)\,. \tag{4.52}$$

The relevant quantities obtained by the Lorentz transform are

$$\begin{cases} E_b^- = \gamma(E^- - \beta|\mathbf{p}^-|\cos\theta^-)\,, \\ \cos\theta_b^- = \gamma(|\mathbf{p}^-|\cos\theta^- - \beta E^-)/((E_b^-)^2 - m^2)\,, \end{cases} \tag{4.53}$$

with setting $\theta_b^- = 0$ if $E_b^- = m$, and

$$\begin{cases} E_{p,b} = \gamma(E_p - \beta|\mathbf{p}|\cos\theta)\,, \\ \cos\theta_b = \gamma(|\mathbf{p}|\cos\theta - \beta E_p)/((E_{p,b})^2 - m^2)\,, \\ \sin\theta_b\cos\phi_b = |\mathbf{p}|\sin\theta\cos\phi/((E_{p,b})^2 - m^2)\,, \end{cases} \tag{4.54}$$

with setting $\theta_b = \phi_b = 0$ if $E_{p,b} = m$.

On the other hand, R_s is not a Lorentz invariant quantity. In the rate formula (4.8), the squared amplitude, δ function, and phase space integrations

$$\frac{d^3p'}{E_{p'}} = 2d^4p'\delta(p'^2 - m^2)H(E_{p'}) \ \ , \frac{d^3k}{\omega} = 2d^4k\delta(k^2)H(\omega)\,, \tag{4.55}$$

with H being the Heaviside step function, are manifestly Lorentz invariant, while the particles' initial energies and the volume lead to the quantity's dependence on the choice of reference frame. For the quantity $R_s = V^2R$ exempted from the volume factor, only the particles' initial energies cause the Lorentz variance. The direct comparison of the forms of R_s in different frames leads to the relation

$$\begin{aligned} R_s(E^+, E^-, \theta^-, E_p, \theta, \phi) =& \frac{mE_b^-E_{p,b}}{E^+E^-E_p} R_s(m, E_b^-, \theta_b^-, E_{p,b}, \theta_b, \phi_b) \\ =& \frac{mE_b^-E_{p,b}}{E^+E^-E_p} R_s(m, E_b^-, \theta_b^r, E_{p,b}, 0, 0)\,. \end{aligned} \tag{4.56}$$

It indicates that, by calculating the rate for one combination $(E_b^-, \theta_b^r, E_{p,b})$, the rate for a set of combinations of $(E^+, E^-, \theta^-, E_p, \theta, \phi)$ can be obtained. For example, by acquiring the information of $R_s(m, m, 0, E_{p,b}, 0, 0)$ with only one independent variable, that of $R_s(E^+, E^+, 0, E_p, \theta, \phi)$ with four independent variables is found.

In order to make use of Eq. (4.56) and to avoid duplication of effort in calculating the rate value, a good way is to apply the basis method. The detailed procedure is presented in Appendix F.

4.4.3 Total rates and particle lifetimes

In Fig. 4.14, the total annihilation rates per volume of both single-photon and two-photon processes are plotted against the plasma temperature. Both rates are found to have a T_p^a form of dependence on the temperature. For the single-photon annihilation, $R_t^{SP} \sim R_s^{SP}\rho^3$, where $\rho^3 \propto T_p^9$, while R_s^{SP} decreases with the increase of T_p, since particles are more energetic at higher temperatures, but higher energies of the particles lead to lower

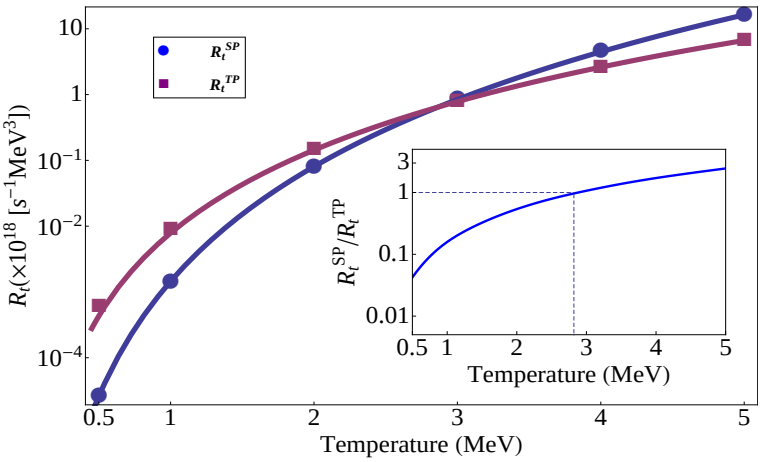

Figure 4.14: Total annihilation rates per volume ($1\,[\mathrm{MeV}^3]$=$1.3 \times 10^{32}[\mathrm{cm}^{-3}]$) for both single-photon process (blue dots) and two-photon process (purple squares) are plotted for various plasma temperatures. The blue line is a fitting law for the single-photon process: $R_t^{SP} = 1.45 \times 10^{-3} T_p^{5.79}$, and the purple line is that for the two-photon process: $R_t^{TP} = 7.87 \times 10^{-3} T_p^{4.19}$. The inset displays the rate ratio of the single-photon process over the two-photon process. R_t^{SP}/R_t^{TP} gets unity at $T_p \approx 2.85\,\mathrm{MeV}$.

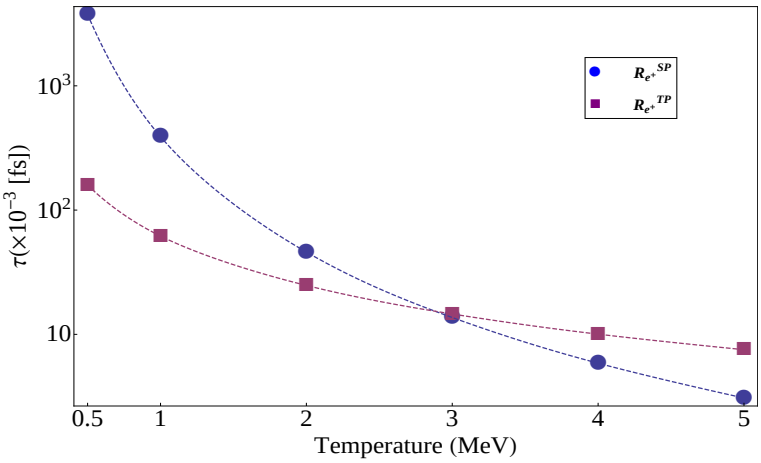

Figure 4.15: The lifetime of a particle in a relativistic electron-positron plasma determined by the single-photon process (blue dots) and two-photon process (purple squares) is shown for various plasma temperatures. For $T_p \geq 3\,\mathrm{MeV}$, the lifetime is mainly determined by the single-photon process. The short lifetime, for example, $\tau \approx 0.003\,\mathrm{fs}$ at $T_p \approx 5\,\mathrm{MeV}$, indicates a time scale of the dynamics in the equilibrium plasma.

annihilation rate, as shown in Table F.1 and Fig. F.2. This reduces the total temperature dependence from 9 to 5.79 orders in the considered temperature region. Similarly, for the two-photon annihilation, the rate value $R_s^{TP}(E)$ in a collision of an E energy electron on a positron at rest also decreases with the particle energy [81]

$$R_s^{TP}(E) = \frac{\alpha^2\pi}{mE}(\ln\frac{2E}{m} - 1)\,, \qquad \text{for } E \gg m\,. \tag{4.57}$$

The integration over $\frac{mE}{p_+^0 p_-^0} R_s^{TP}(E)$ yields a temperature dependence of 4.19, where p_+^0 and p_-^0 are the particles' energies in the lab frame. This order of temperature dependence is less than 6 as would be suggested by the density factor in $R_t^{TP} \sim R_s^{TP}\rho^2$.

It is also shown in Fig. 4.14 that the ratio of the single-photon annihilation rate over the two-photon annihilation rate reaches unity at $T_p \approx 2.85\,\mathrm{MeV}$, which is higher than our previous estimation $T_p \approx 2.3\,\mathrm{MeV}$ using the rate value at the low-energy limit. We note that this temperature difference corresponds to $\approx 5 \times 10^6\,\mathrm{K}$. When $T_p > 3\,\mathrm{MeV}$, the single-photon process overrides the two-photon process, which implies its significance in studying the ultrarelativistic plasmas widely encountered in astrophysics. Besides, even for a mildly relativistic plasma with $T_p \sim m$, the ratio amounts to almost 10^{-1}. This indicates the notable role of the single-photon annihilation as well as other triple processes in, e. g., equilibrium dynamics [104] of relativistic plasmas. As an example, another triple interaction is the three-photon decay of an ortho-Ps [92]. Notice that this decay rate is on the order of 10^{-3} of the two photon process.

Dividing the total rate per volume R_t by the total particle density ρ_t, the annihilation rate per particle can be obtained, the reciprocal of which gives the lifetime of the positron (electron) in the relativistic plasma, denoted by τ. Displayed in Fig. 4.15 is the temperature dependence of the positron (electron) lifetime determined by both single-photon annihilation and two-photon annihilation processes. For example, at $T_p \approx 1\,\mathrm{MeV}$, the particle lifetime would be about 0.4 fs due to the single-photon annihilation, but by the presence of the two-photon annihilation, it is shortened to 0.06 fs. For $T_p > 3\,\mathrm{MeV}$, the short lifetime is determined mainly by the single-photon process, and defines a time scale in which the dynamics in the equilibrium plasma occurs.

4.5 Concluding remarks

In this chapter, the single-photon e^+e^- annihilation via triple interaction was studied. The advantage of the laser-dressed QED approach was illustrated even in the external-field-free case, due to the reduced number of Furry-Feynman diagrams which need to be considered. Various kinematic regimes were examined from the low-energy limit to the general case, and the special characteristics of the radiation were identified. Total single-photon annihilation rates were obtained for relativistic e^+e^- plasmas in equilibrium, the extremely high density of which made the multi-particle correlation effects prominent.

It is interesting to note that single-photon annihilation in the presence of a second electron exhibits an interesting analogy in atomic physics. Free electrons typically recombine

with ions via photo-emission (inverse photo-effect). At high electron densities, however, the radiationless channel of three-body recombination dominates where the recombining electron transfers its energy excess to a nearby partner electron [110]. Single-photon annihilation in the presence of a second electron may be viewed as a three-body recombination with the QED vacuum. In both processes, the recoil absorbed by the assisting electron reduces the number of emitted photons by one.

Chapter 5

Summary and outlook

In this thesis, two relevant QED processes have been investigated: 1) the multi-photon trident e^+e^- pair production in intense laser fields, and 2) the single-photon e^+e^- pair annihilation via triple interaction. The research motivations for both processes are related with the remarkable advancement of high-intensity lasers. A strong laser participates in the first process directly. Its combination with relativistic electrons results in a Doppler-enhanced laser intensity approaching the Schwinger limit in the electron's rest frame. The second process is prominent in high-density e^+e^- samples, and the interest for it is stimulated by the development of prolific e^+e^- pair generation by targeting an intense laser pulse on a heavy metal foil.

The laser-dressed QED approach has been applied in developing theories for both processes. For the pair production in intense laser fields, the laser-dressed QED method allows the nonperturbative treatment of the laser-matter interaction. In the external-field-free pair annihilation process, it simplifies the analysis and program work by formally reducing the number of diagrams, which would require a separate treatment one by one otherwise.

The two processes are related also by a crossing symmetry. It can be seen from the Furry-Feynman diagrams that the outgoing e^+e^- pair in the pair production process is substituted by the incoming e^+e^- pair in the pair annihilation process. Due to the multi-photon nature of the laser-dressed pair production process, a resonance can occur, which is absent in the single-photon pair annihilation. The regularization method has been developed in a systematic way, and allows clear physical interpretations by evidently establishing its connection with the cascade theory.

For the pair production process, numerical calculations have been performed from the perturbative high-frequency regime to the quasi-static low-frequency regime. Various parameter domains for both the nonlinear Bethe-Heitler type (the direct process without resonances) and the nonlinear Breit-Wheeler type (the two-step process with resonances) have also been examined. It was found that a sizable e^+e^- pair production rate (of the order of the SLAC E-144 experiment) could be obtained by combining an already available $\sim 10^{21}\,\mathrm{W/cm^2}$ laser system with a $\sim 1\,\mathrm{GeV}$ electron beam, which can be generated by a sub-meter-scale laser-plasma-accelerator (LPA) [90]. The portability of such compact table-top electron accelerators, compared with the conventional large accelerator

beamlines, would make the trident pair production process more accessible to broad experimental studies in the future. Note that a meter-scale 10 GeV LPA as the aim of the BELLA Project (Berkeley, USA) [111] is also under development currently.

Other species of particles, such as $\mu^+\mu^-$ pairs, may also be produced in the collision of a very energetic electron and an intense laser pulse. Due to their heavier mass, lasers of higher intensity or higher frequency would be required. For example, $\mu^+\mu^-$ pair creation by two-photon absorption could be realized when a $\sim 1\,\mathrm{TeV}$ electron beam collides with an XFEL pulse of $\sim 10\,\mathrm{KeV}$. Nevertheless, the method developed here can be applied directly, with only one Furry-Feynman diagram involved since there are no indistinguishable particles in the final state.

For the pair annihilation process, various kinematic configurations of the three incoming particles have been examined carefully. It was indicated that, for certain collision geometries, e. g., in the case that a high-energetic electron (positron) collides with a e^+e^- pair of low center-of-mass energy, the radiation field of the single-photon annihilation exhibits special frequency, angular and polarization distributions, which would facilitate its detection. High-density e^+e^- samples of equilibrium relativistic e^+e^- plasmas have also been studied. It was found that in a mildly relativistic plasma (temperature $\sim m$), the single-photon annihilation process becomes already notable compared with other triple interactions, and for plasma temperatures above $3\,\mathrm{MeV}$, it prevails over the usual two-photon annihilation.

The distance of neighboring particles in equilibrium relativistic e^+e^- plasmas can be within a Compton wavelength. In principle, the dynamic collective effects also arise in such high-density samples. They can influence the particle dynamics, and modify the radiation from the single-photon process. This in turn makes this process a good probe in studying the correlation-related phenomena. Moreover, it might be interesting to explore whether QED processes of even higher order than triple interaction can also be relevant in high-density e^+e^- plasmas.

Appendix A

Threshold condition for the participating photon number

Energy-momentum conservation is manifested in Eq. (3.7) as $\delta(q + Nk - q' - q_+ - q_-)$, where $|N|$ is the number of photons absorbed ($N > 0$), or emitted ($N < 0$) in the process.

In the average rest frame of the projectile, where $q = (m_*, 0, 0, 0)$, a necessary condition for $q + Nk - q' - q_+ - q_- = 0$ is

$$N\omega \geq 4m_* \,, \tag{A.1}$$

as is proven in the following.

The condition $q + Nk - q' - q_+ - q_- = 0$ can be written in this frame as

$$\begin{aligned} N\omega + m_* =& q'^0 + q_+^0 + q_-^0 \,, \\ N\mathbf{k} =& \mathbf{q}' + \mathbf{q}_+ + \mathbf{q}_- \,. \end{aligned}$$

Therefore

$$\begin{aligned} (N\omega + m_*)^2 - (N\mathbf{k})^2 =& (q'^0 + q_+^0 + q_-^0)^2 - (\mathbf{q}' + \mathbf{q}_+ + \mathbf{q}_-)^2 \,, \\ 2N\omega m_* + m_*^2 =& 3m_*^2 + 2(q'^0 q_+^0 - \mathbf{q}' \cdot \mathbf{q}_+) + 2(q'^0 q_-^0 - \mathbf{q}' \cdot \mathbf{q}_-) + 2(q_+^0 q_-^0 - \mathbf{q}_+ \cdot \mathbf{q}_-) \,, \\ 2N\omega m_* + m_*^2 \geq& 3m_*^2 + 2m_*^2 + 2m_*^2 + 2m_*^2 \,, \\ N\omega \geq& 4m_* \,, \end{aligned}$$

where the inequality relations have been used, such as $q_+^0 q_-^0 - \mathbf{q}_+ \cdot \mathbf{q}_- \geq m_*^2$, which can be proved concisely for energies close to the threshold $q_+^0 \,, q_-^0 \sim m_*$ as follows

$$\begin{aligned} q_+^0 q_-^0 - \mathbf{q}_+ \cdot \mathbf{q}_- \geq& \sqrt{\mathbf{q}_+^2 + m_*^2}\sqrt{\mathbf{q}_-^2 + m_*^2} - |\mathbf{q}_+||\mathbf{q}_-| \\ \approx& m_*^2 (1 + \frac{\mathbf{q}_+^2}{2m_*^2})(1 + \frac{\mathbf{q}_-^2}{2m_*^2}) - |\mathbf{q}_+||\mathbf{q}_-| \\ =& m_*^2 + \frac{(|\mathbf{q}_+| - |\mathbf{q}_-|)^2}{2} \\ \geq& m_*^2 \,. \end{aligned}$$

A general proof is given below. Let $\Delta E = q_+^0 - q_-^0$ and $\Delta q = |\mathbf{q}_+| - |\mathbf{q}_-|$. Then

$$\begin{aligned}
q_+^0 q_-^0 - \mathbf{q}_+ \cdot \mathbf{q}_- \geq & q_+^0 q_-^0 - |\mathbf{q}_+||\mathbf{q}_-| \\
= & (q_-^0 + \Delta E) q_-^0 - (|\mathbf{q}_-| + \Delta q)|\mathbf{q}_-| \\
= & m_*^2 + \Delta E q_-^0 - \Delta q |\mathbf{q}_-| \\
= & m_*^2 + (\sqrt{\mathbf{q}_+^2 + m_*^2} - \sqrt{\mathbf{q}_-^2 + m_*^2})\sqrt{\mathbf{q}_-^2 + m_*^2} - (|\mathbf{q}_+| - |\mathbf{q}_-|)|\mathbf{q}_-| \\
= & m_*^2 + \frac{\mathbf{q}_+^2 - \mathbf{q}_-^2}{1 + \frac{\sqrt{\mathbf{q}_+^2 + m_*^2}}{\sqrt{\mathbf{q}_-^2 + m_*^2}}} - (|\mathbf{q}_+| - |\mathbf{q}_-|)|\mathbf{q}_-| \\
= & m_*^2 + \frac{|\mathbf{q}_+| - |\mathbf{q}_-|}{1 + \frac{\sqrt{\mathbf{q}_+^2 + m_*^2}}{\sqrt{\mathbf{q}_-^2 + m_*^2}}} (|\mathbf{q}_+| + |\mathbf{q}_-| - |\mathbf{q}_-|(1 + \frac{\sqrt{\mathbf{q}_+^2 + m_*^2}}{\sqrt{\mathbf{q}_-^2 + m_*^2}})) \\
= & m_*^2 + \frac{\Delta q |\mathbf{q}_+|}{1 + \frac{\sqrt{\mathbf{q}_+^2 + m_*^2}}{\sqrt{\mathbf{q}_-^2 + m_*^2}}} (1 - \frac{|\mathbf{q}_-|\sqrt{\mathbf{q}_+^2 + m_*^2}}{|\mathbf{q}_+|\sqrt{\mathbf{q}_-^2 + m_*^2}}) \\
= & m_*^2 + \frac{\Delta q |\mathbf{q}_+|}{1 + \frac{\sqrt{\mathbf{q}_+^2 + m_*^2}}{\sqrt{\mathbf{q}_-^2 + m_*^2}}} (1 - \frac{\sqrt{\mathbf{q}_+^2 \mathbf{q}_-^2 + m_*^2 \mathbf{q}_-^2}}{\sqrt{\mathbf{q}_+^2 \mathbf{q}_-^2 + m_*^2 \mathbf{q}_+^2}}) \\
\geq & m_*^2 .
\end{aligned}$$

The other two inequalities $q'^0 q_+^0 - \mathbf{q}' \cdot \mathbf{q}_+ \geq m_*^2$, $q'^0 q_-^0 - \mathbf{q}' \cdot \mathbf{q}_- \geq m_*^2$ can be proven in a similar way.

It can also be proven that, in the center of inertial frame where $N\mathbf{k} + \mathbf{q} = 0$, the threshold condition takes the form

$$N\omega \geq \frac{4}{3} m_* , \tag{A.2}$$

due to

$$\begin{aligned}
N\omega + q^0 = & q'^0 + q_+^0 + q_-^0 , \\
\mathbf{q} = & -N\mathbf{k} ,
\end{aligned}$$

and then

$$N\omega + \sqrt{N^2 \mathbf{k}^2 + m_*^2} \geq 3 m_* ,$$

which has the inequality (A.2) as its solution.

Naturally, the threshold condition also confirms that pair production can not take place with a net emission of laser photons ($N < 0$).

Appendix B

Integration techniques

The method to determine the integration regime follows mainly from Mork's work [57].

Energy-momentum conservation $\delta^{(4)}(q + Nk - q' - q_+ - q_-)$ in Eq. (3.7) determines the kinematics of the multi-photon trident pair production process. It can be used to simplify the integrations over the momentum space of the final particles $\int d^3\mathbf{q}' d^3\mathbf{q}_- d^3\mathbf{q}_+$. The following analysis is valid in the center of inertial frame, where $\mathbf{q} + N\mathbf{k} = 0$. The geometry is shown in Fig. B.1.

The momentum conservation $\delta^3(\mathbf{q}' + \mathbf{q}_- + \mathbf{q}_+)$ reduces the momentum integration by one particle, for example $\mathbf{q}_-$, while the energy conservation part $\delta((q^0 + Nk^0) - (q'^0 + q_+^0 + q_+^0))$ gives $(q^0 + Nk^0) - (q'^0 + q_+^0) = q_-^0 = \sqrt{\mathbf{q}'^2 + \mathbf{q}_+^2 - 2|\mathbf{q}'||\mathbf{q}_+| \cos\beta + m_*^2}$, where β is the angle between $\mathbf{q}'$ and $\mathbf{q}_+$. Without loss of generality, $\int d^3\mathbf{q}_+$ can be performed in a specially chosen coordinate system to simplify the calculation. With the coordinates illustrated in Fig. B.1, the integration takes the form

$$
\begin{aligned}
&\int d^3\mathbf{q}' d^3\mathbf{q}_- d^3\mathbf{q}_+ \delta^{(4)}(q + Nk - q' - q_+ - q_-) \\
&= \int_{-1}^{1} d\cos\theta \int_0^{2\pi} d\phi_1 \int \mathbf{q}'^2 d|\mathbf{q}'| \int_{-1}^{1} d\cos\beta \int_0^{2\pi} d\phi_2 \int \mathbf{q}_+^2 d|\mathbf{q}_+| \\
&\quad \times \frac{E_{\mathtt{tot}} - q'^0 - q_+^0}{|\mathbf{q}'||\mathbf{q}_+|} \delta(\cos\beta + \frac{E_{\mathtt{tot}}^2 + 2q'^0 q_+^0 + m_*^2 - 2E_{\mathtt{tot}}(q'^0 + q_+^0)}{2|\mathbf{q}'||\mathbf{q}_+|}) \\
&= \int_{-1}^{1} d\cos\theta \int_0^{2\pi} d\phi_1 \int_0^{2\pi} d\phi_2 \int \mathbf{q}'^2 d|\mathbf{q}'| \int \mathbf{q}_+^2 d|\mathbf{q}_+| \frac{E_{\mathtt{tot}} - q'^0 - q_+^0}{|\mathbf{q}'||\mathbf{q}_+|} \\
&= \int_{-1}^{1} d\cos\theta \int_0^{2\pi} d\phi_1 \int_0^{2\pi} d\phi_2 \int q'^0 dq'^0 \int q_+^0 dq_+^0 (E_{\mathtt{tot}} - q'^0 - q_+^0)\,,
\end{aligned}
\tag{B.1}
$$

where $E_{\mathtt{tot}}$ is the total energy $E_{\mathtt{tot}} = q^0 + Nk^0$, θ is the angle between $\mathbf{q}'$ and $\mathbf{k}$ (i. e. between $\mathbf{q}'$ and the z axis of the xyz coordinate system), ϕ_1 is the azimuth angle of $\mathbf{q}'$ in this frame, and ϕ_2 is the azimuth angle of $\mathbf{q}_+$ in the $x'y'z'$ coordinate system with $\mathbf{q}'$ along the z' axis.

The condition $|\cos\beta| \leq 1$ determines the boundaries for q_+^0. That results in $q_+^0 \in [q_{+l}^0, q_{+u}^0]$,

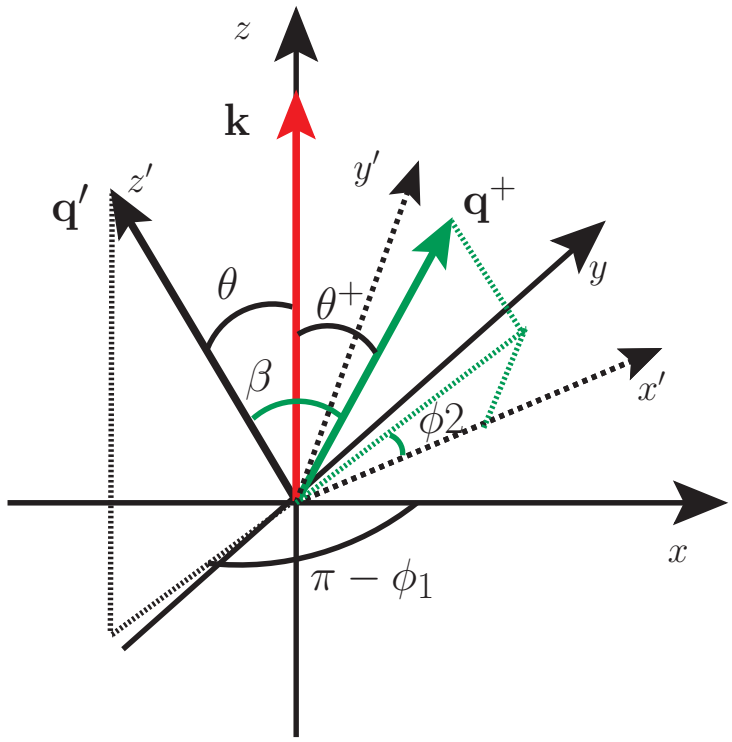

Figure B.1: The geometry of the multi-photon trident pair production in the center of inertial frame, where $\mathbf{q} + N\mathbf{k} = 0$, with $\mathbf{k} \parallel \hat{z}$. The integration of $\mathbf{q}'$ is performed via its solid angles (θ, ϕ_1) in the xyz coordinate system, while the integration of $\mathbf{q}^+$ is performed via its solid angles (β, ϕ_2) in the $x'y'z'$ coordinate system, which is chosen so that $\hat{z'} \parallel \mathbf{q}'$, $\hat{y'}$ is in the xy plane, $\hat{x'}$ is in the plane spanned by $\mathbf{k}$ and $\mathbf{q}'$, and the angle between $\hat{x'}$ and $\mathbf{k}$ is specified to be always $\leq 90°$. The polar angle θ^+ of $\mathbf{q}^+$ in the xyz coordinates can be obtained by $\cos\theta^+ = \cos\theta\cos\beta + \sqrt{(1-\cos^2\theta)(1-\cos^2\beta)}\cos\phi_2$.

with

$$q^0_{+l} = \frac{1}{2}\left(E_{\mathtt{tot}} - q'^0 - |\mathbf{q}'|\sqrt{1 - \frac{2m_*^2}{E_{\mathtt{tot}}(q^0 - q'^0)}}\right) , \tag{B.2}$$

$$q^0_{+u} = \frac{1}{2}\left(E_{\mathtt{tot}} - q'^0 + |\mathbf{q}'|\sqrt{1 - \frac{2m_*^2}{E_{\mathtt{tot}}(q^0 - q'^0)}}\right) . \tag{B.3}$$

The condition for a real $q^0_{+l/u}$, that is $1 - \frac{2m_*^2}{E_{\mathtt{tot}}(q^0 - q'^0)} \geq 0$, gives the upper limit for q'^0

$$q'^0_u = 2|\mathbf{q}| - q^0 , \tag{B.4}$$

which can be seen as follows

$$\begin{aligned} 1 - \frac{2m_*^2}{E_{\mathtt{tot}}(q^0 - q'^0)} &\geq 0 , \\ \frac{(q^0)^2 - 2m_*^2 + q^0|\mathbf{q}|}{q^0 + |\mathbf{q}|} &\geq q'^0 , \\ \frac{|\mathbf{q}|^2 - ((q^0)^2 - |\mathbf{q}|^2) + q^0|\mathbf{q}|}{q^0 + |\mathbf{q}|} &\geq q'^0 , \\ 2|\mathbf{q}| - q^0 &\geq q'^0 . \end{aligned}$$

Here $|\mathbf{q}|$ is the magnitude of the momentum of the initial electron. Due to the choice of the reference frame, it is also the magnitude of the energy and momentum of the colliding N laser photons, thus $E_{\mathtt{tot}} = q^0 + |\mathbf{q}|$. The lower boundary for q'^0 is m_*.

It can be proven that $q'^0_u \geq m_*$ and $q^0_{+l} \geq m_*$ automatically hold if the threshold condition Eq. (A.2) is satisfied.

Appendix C

The resonance condition

Without loss of generality, we discuss the resonance condition by analyzing the left diagram in Fig. 3.1. There the resonance condition is

$$k'^2 = (q - q' + nk)^2 = 0\,. \tag{C.1}$$

It is the same kinematic condition as that from the four-momentum conservation relation of the multi-photon Compton scattering, where the electron with initial laser-dressed momentum q is scattered to the final state of momentum q' by absorption of n photons with momentum k, and emits a photon with momentum $k' = q - q' + nk$.

Let θ be the angle between $\mathbf{q}'$ and $\mathbf{k}$ (since we consider a head-on collision, the angle between $\mathbf{q}'$ and $\mathbf{q}$ is $\pi - \theta$). Then from Eq. (C.1) we obtain

$$\cos\theta = \frac{(nk^0 + q^0)q'^0 - (m_*^2 + nk \cdot q)}{(n|\mathbf{k}| - |\mathbf{q}|)|\mathbf{q}'|}\,, \tag{C.2}$$

along with the well-known formula for the frequency of the emitted photon in a (multi-photon) Compton scattering [38]

$$\mathbf{k}'^0 = \frac{nk \cdot q}{(nk^0 + q^0) - (n|\mathbf{k}| - |\mathbf{q}|)\cos\theta'}\,, \tag{C.3}$$

where θ' is the angle between $\mathbf{k}'$ and $\mathbf{k}$. The frequency of the emitted photon is shifted by the presence of the laser field, as a result of the laser-dressed momentum q involved. This can be viewed explicitly in the average rest frame of the incoming electron ($\mathbf{q} = 0$), where Eq. (C.3) takes the form

$$\begin{aligned}\mathbf{k}'^0 =& \frac{n|\mathbf{k}|}{1 + \frac{n|\mathbf{k}|}{m_*}(1 - \cos\theta')} \\ =& \frac{n|\mathbf{k}|}{1 + \frac{n|\mathbf{k}|}{m\sqrt{1+\xi^2}}(1 - \cos\theta')}\,.\end{aligned} \tag{C.4}$$

In the limit $\xi \to 0$, $n = 1$, it reproduces the ordinary formula for Compton scattering.

It has been shown in Appendix B that the four-momentum conservation for the pair production process puts constraints on the range that the energy q'^0 can assume

$$q'^0 \leq 2|\mathbf{q}| - q^0 \,.$$

The on-shell condition (C.1) adds further restrictions, due to $|\cos\theta| \leq 1$ in Eq. (C.2). We show in the following that $k'^2 = (q - q' + nk)^2 = 0$ can be satisfied only when

$$1.\quad n_{min} \leq n \leq n_{max} \,, \tag{C.5a}$$

$$2.\quad q'^0_{lr} \leq q'^0 \leq 2|\mathbf{q}| - q^0 \,, \tag{C.5b}$$

where n_{min}, n_{max} are given in Eq. (C.13), and q'^0_{lr} is given in Eq. (C.10) in the center of inertia frame.

Notice that $k \cdot q = k^0 q^0 + |\mathbf{k}||\mathbf{q}|$ in the head-on collision. The requirement $|\cos\theta| \leq 1$ restricts q'^0 to the interval $q'^0_{lr} \leq q'^0 \leq q'^0_{ur}$ with

$$q'^0_{lr} = \frac{(nk^0 + q^0)(m_*^2 + n(k\cdot q)) - n(k\cdot q)|n|\mathbf{k}| - |\mathbf{q}||}{m_*^2 + 2n(k\cdot q)} \,, \tag{C.6a}$$

$$q'^0_{ur} = \frac{(nk^0 + q^0)(m_*^2 + n(k\cdot q)) + n(k\cdot q)|n|\mathbf{k}| - |\mathbf{q}||}{m_*^2 + 2n(k\cdot q)} \,. \tag{C.6b}$$

In the center of inertia frame where $\mathbf{q} = -N\mathbf{k}$, with N being the total number of photons absorbed in the pair production process, Eqs. (C.6) take the form

$$q'^0_{lr} = (nk^0 + q^0) - \frac{n(k\cdot q)[q^0 + k^0(n + |n - N|)]}{m_*^2 + 2n(k\cdot q)} \,, \tag{C.7a}$$

$$q'^0_{ur} = (nk^0 + q^0) - \frac{n(k\cdot q)[q^0 + k^0(n - |n - N|)]}{m_*^2 + 2n(k\cdot q)} \,. \tag{C.7b}$$

For simplicity in writing, designate $k \cdot q = \eta$ and $m_*^2 + 2N(k\cdot q) = \beta$, and then

$$k^0 = \frac{k\cdot q}{\sqrt{m_*^2 + 2N(k\cdot q)}} = \frac{\eta}{\sqrt{\beta}} \,,$$

$$q^0 = \sqrt{(Nk^0)^2 + m_*^2} = \frac{N\eta + m_*^2}{\sqrt{\beta}} \,. \tag{C.8}$$

Substituting Eqs. (C.8) into Eqs. (C.7), we get

If $n \geq N$,

$$q'^0_{lr} = \frac{1}{\sqrt{\beta}}[N\eta + m_*^2] \,, \tag{C.9a}$$

$$q'^0_{ur} = \frac{1}{\sqrt{\beta}}[(N + n - \frac{n\beta}{m_*^2 + 2n\eta})\eta + m_*^2] \,, \tag{C.9b}$$

and

If $n < N$,

$$q'^0_{lr} = \frac{1}{\sqrt{\beta}}[(N + n - \frac{n\beta}{m_*^2 + 2n\eta})\eta + m_*^2] \,, \tag{C.10a}$$

$$q'^0_{ur} = \frac{1}{\sqrt{\beta}}[N\eta + m_*^2] \,. \tag{C.10b}$$

Similarly, the general momentum boundaries ($q_l'^0 \leq q'^0 \leq q_u'^0$), given in Appendix B, can be rewritten by using β and η as

$$q_l'^0 = m_* \,, \tag{C.11a}$$

$$q_u'^0 = 2|\mathbf{q}| - q^0 = \frac{1}{\sqrt{\beta}}[N\eta - m_*^2] \,. \tag{C.11b}$$

The direct comparison of Eq. (C.9) and Eq. (C.11) shows that if $n \geq N$, then $q_{lr}'^0 > q_u'^0$, and therefore the resonance condition can not be satisfied under the general condition of the whole process. We only need to consider the case where $n < N$. Then it is already obvious that $q_{ur}'^0 > q_u'^0$, and the resonance can be possible if and only if $q_{lr}'^0 \leq q_u'^0$. This criterion leads to

$$\begin{aligned}
n + N - \frac{n(\frac{m_*^2}{\eta} + 2N)}{\frac{m_*^2}{\eta} + 2n} &\leq N - \frac{2m_*^2}{\eta} \,, \\
(\frac{m_*^2}{\eta} + n)^2 &\leq Nn \,, \\
(\sqrt{n} - \frac{\sqrt{N}}{2})^2 &\leq \frac{N}{4} - \frac{m_*^2}{\eta} \,, \\
\frac{\sqrt{N}}{2} - \sqrt{\frac{N}{4} - \frac{m_*^2}{\eta}} \leq \sqrt{n} &\leq \frac{\sqrt{N}}{2} + \sqrt{\frac{N}{4} - \frac{m_*^2}{\eta}} \,.
\end{aligned} \tag{C.12}$$

Notice that $\eta \geq \frac{4m_*^2}{N}$. The range of n can be determined as $n_{min} \leq n \leq n_{max}$ with

$$n_{min} = \text{Ceiling}[(\frac{\sqrt{N}}{2} - \sqrt{\frac{N}{4} - \frac{m_*^2}{\eta}})^2] \,, \tag{C.13a}$$

$$n_{max} = \text{Floor}[(\frac{\sqrt{N}}{2} + \sqrt{\frac{N}{4} - \frac{m_*^2}{\eta}})^2] \,. \tag{C.13b}$$

This gives the first resonance condition. Obviously $n_{min} \geq 1$ and $n_{max} \leq N - 1$.

The intersection of $[q_l'^0, q_u'^0]$ and $[q_{lr}'^0, q_{ur}'^0]$ gives the range of q'^0 in a resonance process. It is proved in the following that $q_{lr}'^0 \geq m_*$ always holds, so that the second resonance condition becomes $q'^0 \in [q_{lr}'^0, q_u'^0]$.

$$\begin{aligned}
(q_{lr}'^0)^2 - m_*^2 &= \frac{1}{\beta}[(N - \Delta)\eta + m_*^2]^2 - m_*^2 \\
&= \frac{\eta}{\beta}[\eta(N - \Delta)^2 - 2m_*^2\Delta] \\
&\geq \frac{\eta}{\beta}[\eta(N - \Delta_{max})^2 - 2m_*^2\Delta_{max}] \\
&= 0 \,,
\end{aligned} \tag{C.14}$$

with

$$\begin{aligned}\Delta &= \frac{2(N-n)n\eta}{m_*^2+2n\eta} \\ &= N + \frac{m_*^2}{\eta} - [(n+\frac{m_*^2}{2\eta}) + \frac{m_*^2}{2\eta}\frac{N+\frac{m_*^2}{2\eta}}{n+\frac{m_*^2}{2\eta}}] \\ &\leq N + \frac{m_*^2}{\eta} - 2\sqrt{\frac{m_*^2}{2\eta}(N+\frac{m_*^2}{2\eta})} \\ &< N\,, \end{aligned} \tag{C.15}$$

and $\Delta_{max} = N + \frac{m_*^2}{\eta} - 2\sqrt{\frac{m_*^2}{2\eta}(N+\frac{m_*^2}{2\eta})}$. It is worthwhile to notice that, for Δ taking the value of Δ_{max}, there should be $n = \sqrt{\frac{m_*^2}{2\eta}(N+\frac{m_*^2}{2\eta})} - \frac{m_*^2}{2\eta}$. Since n is an integer, the right-hand side of this equation should also be an integer, which is in general not the case. Therefore, most of the time, it is an absolute inequality $q_{lr}'^0 > m_*$.

Substituting q'^0 by q_-^0 in (C.5), the resonance condition for the right diagram in Fig. 3.1 is obtained.

Appendix D

Resonance and cascade process

We show that in the limit $\epsilon \to 0$ the pair production amplitude corresponding to the second term of the propagator in Eq. (3.42) can be transformed to an amplitude of a cascade process, where a real photon produced by the laser-dressed spontaneous radiation subsequently participates in a laser-dressed photon-photon pair production.

As indicated in the discussions about Eq. (3.30), the interference of the exchange diagrams is not important in a resonance problem, and the two diagrams in Fig. 3.1 can be considered independently. We only need to consider, for example, the left diagram in Fig. 3.1. What we obtain will be naturally applicable for the right diagram as well. The photon propagator in momentum space is given by

$$\frac{1}{k'^2 + i\epsilon} = \frac{k'^2}{k'^4 + \epsilon^2} + \frac{-i\epsilon}{k'^4 + \epsilon^2}\,, \tag{D.1}$$

with k' the momentum of the intermediate photon and $i\epsilon$ the regulator. The amplitudes of the left diagram with the first and second term of the propagator are denoted by S'_{fi} and S''_{fi}, respectively

$$\begin{aligned} S'_{fi} = &-i\alpha \int d^4x \int d^4y \bar{\Psi}_{q',s'}(x)\gamma_\mu \Psi_{q,s}(x) \\ &\times \int \frac{d^4k'}{(2\pi)^4} \frac{-4\pi g^{\mu\nu}(k'^2)}{k'^4 + \epsilon^2} e^{ik'(x-y)} \bar{\Psi}_{q_-,s_-}(y)\gamma_\nu \Psi_{q_+,s_+}(y)\,, \end{aligned} \tag{D.2}$$

and

$$\begin{aligned} S''_{fi} = &-i\alpha \int d^4x \int d^4y \bar{\Psi}_{q',s'}(x)\gamma_\mu \Psi_{q,s}(x) \\ &\times \int \frac{d^4k'}{(2\pi)^4} \frac{-4\pi g^{\mu\nu}(-i\epsilon)}{k'^4 + \epsilon^2} e^{ik'(x-y)} \bar{\Psi}_{q_-,s_-}(y)\gamma_\nu \Psi_{q_+,s_+}(y)\,. \end{aligned} \tag{D.3}$$

With the relation [52]

$$\lim_{\epsilon \to 0} \frac{\epsilon}{x^2 + \epsilon^2} = \pi\delta(x)\,, \tag{D.4}$$

Eq. (D.3) as $\epsilon \to 0$ turns out to be

$$S''_{fi}(\epsilon \to 0) = \alpha \int d^4x \int d^4y \bar{\Psi}_{q',s'}(x)\gamma_\mu \Psi_{q,s}(x) \int \frac{d^3\mathbf{k}'}{(2\pi)^3} \times \int \frac{dk'^0}{(2\pi)} 4\pi^2 g^{\mu\nu}\delta(k'^2) e^{ik'(x-y)} \bar{\Psi}_{q_-,s_-}(y)\gamma_\nu \Psi_{q_+,s_+}(y)\,. \tag{D.5}$$

Substituting

$$\delta(k'^2) = \delta((k'^0)^2 - \mathbf{k}'^2) = \frac{\delta(k'^0 - |\mathbf{k}'|)}{2|k'^0|} + \frac{\delta(k'^0 + |\mathbf{k}'|)}{2|k'^0|} \tag{D.6}$$

into Eq. (D.5), carrying out the integration of k'^0, and using reversely the completeness relation of the photon polarization vectors $\sum_{\text{polarizations}} \epsilon^*_\mu \epsilon_\nu = -g^{\mu\nu}$, the amplitude takes the form

$$\begin{aligned} S''_{fi}(\epsilon \to 0) =& \frac{\alpha}{2} \int \frac{V d^3\mathbf{k}'}{(2\pi)^3} \sqrt{\frac{2\pi}{Vk'^0}} \int d^4x \bar{\Psi}_{q',s'}(x)\gamma_\mu \Psi_{q,s}(x) e^{i\tilde{k}'x} \\ & \times g^{\mu\nu} \sqrt{\frac{2\pi}{Vk'^0}} \int d^4y \bar{\Psi}_{q_-,s_-}(y)\gamma_\nu \Psi_{q_+,s_+}(y) e^{-i\tilde{k}'y} \\ =& \sum_{\text{polarizations}} \frac{1}{2} \int \frac{V d^3\mathbf{k}'}{(2\pi)^3} \sqrt{\frac{2\pi}{Vk'^0}} \int d^4x \bar{\Psi}_{q',s'}(x)(-ie)\epsilon^*_\mu \gamma_\mu \Psi_{q,s}(x) e^{i\tilde{k}'x} \\ & \times \sqrt{\frac{2\pi}{Vk'^0}} \int d^4y \bar{\Psi}_{q_-,s_-}(y)(-ie)\epsilon_\nu \gamma_\nu \Psi_{q_+,s_+}(y) e^{-i\tilde{k}'y} \\ =& \frac{1}{2} \sum_{\text{polarizations}} \int \frac{V d^3\mathbf{k}'}{(2\pi)^3} S_{e\to e+k'} S_{k'\to e^+e^-}\,, \end{aligned} \tag{D.7}$$

where $\tilde{k}' = (|\mathbf{k}'|, \mathbf{k}')$, $k'^0 = |\mathbf{k}'|$, and the normalization factor of a real photon $\sqrt{\frac{2\pi}{Vk'^0}}$ appears automatically. In fact, only the first term of Eq. (D.6) contributes, and gives the real photon energy-momentum relation. The second term, which leads to a highly oscillating factor $e^{i(q^0_+ + q^0_- + |\mathbf{k}'|)y^0}$ in the temporal integration of y, drops out. The result is a product of two amplitudes: $S_{e\to e+k'} = \sqrt{\frac{2\pi}{Vk'^0}} \int d^4x \bar{\Psi}_{q',s'}(x)(-ie)\epsilon^*_\mu \gamma_\mu \Psi_{q,s}(x) e^{i\tilde{k}'x}$ is the amplitude of laser-dressed photon emission, and $S_{k'\to e^+e^-} = \sqrt{\frac{2\pi}{Vk'^0}} \int d^4y \bar{\Psi}_{q_-,s_-}(y)(-ie)\epsilon_\nu \gamma_\nu \Psi_{q_+,s_+}(y) e^{-i\tilde{k}'y}$ is that of laser-dressed pair production. The two individual processes are connected by a real photon, which is produced by the first process, and takes part in the second. All possible states of this intermediate photon should be taken into account, as is the case due to the polarization sum and momentum integration, with $\frac{V d^3\mathbf{k}'}{(2\pi)^3}$ being the number of states within the momentum range $d^3\mathbf{k}'$. Up to a factor $\frac{1}{2}$, Eq. (D.7) gives the amplitude of a cascade process, where the output of the previous step is the input of the next. The factor $\frac{1}{2}$ is related to the fact that in the cascade process, the intermediate photon (particle) propagates forward in time, and therefore has a positive energy.

As displayed in Eq. (3.30) and the related discussions, the interference of the two diagrams in Fig. 3.1 does not contribute to the formally divergent part of the probability, and can

be neglected in a resonance problem as long as ϵ is small enough. This allows the separate calculation of the two diagrams. Similarly, although in general $|S'_{fi}+S''_{fi}|^2 \neq |S'_{fi}|^2+|S''_{fi}|^2$, it can be treated in a resonance problem as $|S'_{fi}+S''_{fi}|^2 \to |S'_{fi}|^2+|S''_{fi}|^2$. This can be seen as follows. Eq. (3.29) shows that the dominant part of the probability takes the form

$$R = \frac{\alpha^2 m^4}{(2\pi)^3 q^0} \sum_N \sum_n \Lambda_{N,n} \,, \tag{D.8}$$

where $\Lambda_{N,n}$ contains the integrations over final momenta

$$\begin{aligned} \Lambda_{N,n} = & \int \frac{d^3\mathbf{q}'}{q'^0} \int \frac{d^3\mathbf{q}_+}{q_+^0} \int \frac{d^3\mathbf{q}_-}{q_-^0} \delta(q+Nk-q'-q_+-q_-) \\ & \times |\frac{1}{(q-q'+nk)^2+i\epsilon}|^2 F_{N,n}(q,k,q',q_+,q_-) \,, \end{aligned} \tag{D.9}$$

with $F_{N,n}(q,k,q',q_+,q_-)$ designating the real function of the trace product

$$\begin{aligned} F_{N,n}(q,k,q',q_+,q_-) = & \sum_{\text{spins}} |M^\mu(q,q'|n) M_\mu(q_+,q_-|N-n)|^2 \\ = & Tr[\frac{\not{p}_- + m}{2m} \Gamma_{\mu n}(q_-,q_+) \frac{\not{p}_+ - m}{2m} \bar{\Gamma}_{\nu n}(q_-,q_+)] \\ & \times Tr[\frac{\not{p}' + m}{2m} \Gamma_n^\mu(q,q') \frac{\not{p} + m}{2m} \bar{\Gamma}_n^\nu(q,q')] \,. \end{aligned} \tag{D.10}$$

Since the absolute squares of the propagator and the other parts of the amplitude are separated, the propagator-related part of the integrand in Eq. (D.9) can be viewed as

$$\begin{aligned} \Lambda'_{N,n} = & \big(|\frac{(q-q'+nk)^2}{(q-q'+nk)^4+\epsilon^2}|^2 + |\frac{-i\epsilon}{(q-q'+nk)^4+\epsilon^2}|^2\big) F_{N,n}(q,k,q',q_+,q_-) \\ = & \sum_{\text{spins}} |\frac{(q-q'+nk)^2 M^\mu(q,q'|n) M_\mu(q_+,q_-|N-n)}{(q-q'+nk)^4+\epsilon^2}|^2 \\ & + \sum_{\text{spins}} |\frac{-i\epsilon M^\mu(q,q'|n) M_\mu(q_+,q_-|N-n)}{(q-q'+nk)^4+\epsilon^2}|^2 \,. \end{aligned} \tag{D.11}$$

Hence the contributions to the probability from the two parts of the propagator can be accounted for separately.

Notice that in $S''_{fi}(\epsilon \to 0)$, from the temporal integrations of x and y, both $S_{e\to e+k'}$ and $S_{k'\to e^+e^-}$ contain a δ function of energy, which gives a factor of interaction time T in each of the squared amplitudes. Therefore, the probability $|S''_{fi}(\epsilon \to 0)|^2 \sim T^2$, and the differential rate $R''(\epsilon \to 0) = \frac{|S''_{fi}(\epsilon\to 0)|^2}{T} \sim T$. The total rate obtained by integrating over all the possible final states maintains its proportionality to T. $R''(\epsilon \to 0)$ is formally divergent for an infinite interaction time, for example, as is the case when the cascade process takes place in an infinitely extended laser field, without regard to finite lifetimes of particles in a laser field.

Next we will bring the formula for $R''(\epsilon \to 0)$ into the form that will be used in Appendix E to determine the regulator.

Let us start from Eq. (D.5) (or sum over the polarizations in Eq. (D.7)). Inserting the Volkov wave functions, and carrying out the space-time integrations, the square of the amplitude is given by

$$\begin{aligned}
|S''_{fi}(\epsilon\to 0)|^2 =&\Big|\alpha\int d^4x\int d^4y\bar{\Psi}_{q',s'}(x)\gamma_\mu\Psi_{q,s}(x)\\
&\times\int\frac{d^3\mathbf{k}'}{(2\pi)^3}\int\frac{dk'^0}{(2\pi)}4\pi^2 g^{\mu\nu}\delta(k'^2)e^{ik'(x-y)}\bar{\Psi}_{q_-,s_-}(y)\gamma_\nu\Psi_{q_+,s_+}(y)\Big|^2\\
=&\Big|\alpha\int d^4x\int d^4y\bar{\Psi}_{q',s'}(x)\gamma^\mu\Psi_{q,s}(x)\\
&\times\int\frac{d^3\mathbf{k}'}{(2\pi)^3}\int\frac{dk'^0}{(2\pi)}4\pi^2\frac{\delta(k'^0-|\mathbf{k}'|)}{2|k'^0|}e^{ik'(x-y)}\bar{\Psi}_{q_-,s_-}(y)\gamma_\mu\Psi_{q_+,s_+}(y)\Big|^2\\
=&\alpha^2\Big|\sum_N\sum_n\int\frac{(2\pi)^6d^3\mathbf{k}'}{2|\mathbf{k}'|}\frac{m^2}{V^2\sqrt{q^0q'^0q_+^0q_-^0}}\delta(\tilde{k}'+(N-n)k-q_--q_+)\\
&\times\delta(q+nk-q'-\tilde{k}')M^\mu(q,q'|n)M_\mu(q_+,q_-|N-n)\Big|^2\,,
\end{aligned}\tag{D.12}$$

where $M^\mu(q,q'|n)$ and $M_\mu(q_+,q_-|N-n)$ are given in Eq. (3.8). Evaluating the square leads to

$$\begin{aligned}
|S''_{fi}(\epsilon\to 0)|^2 =&\frac{m^4\alpha^2(2\pi)^{12}}{4V^4q^0q'^0q_+^0q_-^0}\sum_{N_1}\sum_{N_2}\sum_{n_1}\sum_{n_2}\int\frac{d^3\mathbf{k}'}{|\mathbf{k}'|}\int\frac{d^3\mathbf{k}''}{|\mathbf{k}''|}\\
&\times\delta(q+n_1k-q'-\tilde{k}')\delta(q+N_1k-q'-q_--q_+)\\
&\times\delta(q+n_2k-q'-\tilde{k}'')\delta(q+N_2k-q'-q_--q_+)\\
&\times M^\mu(q,q'|n_1)M_\mu(q_+,q_-|N_1-n_1)\\
&\times M^{\nu*}(q,q'|n_2)M^*_\nu(q_+,q_-|N_2-n_2)\\
=&\frac{m^4\alpha^2(2\pi)^8}{4V^4q^0q'^0q_+^0q_-^0}\sum_{N}\sum_{n_1}\sum_{n_2}\int\frac{d^3\mathbf{k}'}{|\mathbf{k}'|}\int\frac{d^3\mathbf{k}''}{|\mathbf{k}''|}\\
&\times\delta(q+n_1k-q'-\tilde{k}')\delta(q+n_2k-q'-\tilde{k}'')\delta(q+Nk-q'-q_--q_+)VT\\
&\times M^\mu(q,q'|n_1)M_\mu(q_+,q_-|N-n_1)\\
&\times M^{\nu*}(q,q'|n_2)M^*_\nu(q_+,q_-|N-n_2)\,,
\end{aligned}\tag{D.13}$$

where the square of the δ function is replaced by the rule $(2\pi)^4\delta^4(0)=VT$ [81,109]. This factor of T would be canceled when computing the rate $R''(\epsilon\to 0)=\frac{|S''_{fi}(\epsilon\to 0)|^2}{T}$.

As discussed for Eq. (3.30), in a resonance problem, the sum in Eq. (D.13) with $n_1\neq n_2$

does not lead to divergence. The dominant part is that with $n_1 = n_2$. Therefore,

$$\begin{aligned}
R''(\epsilon \to 0) \approx & \frac{m^4\alpha^2(2\pi)^8}{4V^3 q^0 q'^0 q_+^0 q_-^0} \sum_N \delta(q + Nk - q' - q_- - q_+) \\
& \sum_n \int \frac{d^3\mathbf{k}'}{|\mathbf{k}'|} \int \frac{d^3\mathbf{k}''}{|\mathbf{k}''|} \delta(q + nk - q' - \tilde{k}')\delta(\tilde{k}' - \tilde{k}'') \\
& \times |M^\mu(q, q'|n) M_\mu(q_+, q_-|N - n)|^2 \\
= & \frac{m^4\alpha^2(2\pi)^8}{4V^3 q^0 q'^0 q_+^0 q_-^0} \sum_N \delta(q + Nk - q' - q_- - q_+) \\
& \sum_n \frac{1}{(q^0 + nk^0 - q'^0)^2} \delta(q^0 + nk^0 - q'^0 - |\mathbf{q} + n\mathbf{k} - \mathbf{q}'|) \frac{T}{2\pi} \\
& \times |M^\mu(q, q'|n) M_\mu(q_+, q_-|N - n)|^2 , \qquad \text{(D.14)}
\end{aligned}$$

where T arises again by the replacement rule $2\pi\delta(0) = T$ [81]. As drawn from the experience with the cascade theory, T is the characteristic time of the process. We will refer to Eq. (D.14) in the next appendix.

Appendix E

The regulator

In the analysis of the SLAC experiment, it was found that the pair production was largely dominated by the two-step process (cascade process). In fact, since $\frac{R_{\text{resonance}}}{R_{\text{non-resonance}}} \sim T$, this will in principle always hold for relatively long interaction times (e.g., $T \gtrsim \frac{m}{eE}$ in the quasistatic regime where the laser wavelength is long, $\omega \ll m$ [78]). In the following, we first determine the value of the regulator ϵ by taking reference to the cascade theory. Then the quantitative analysis is applied on the comparison of the rates contributed from the two parts of the propagator. Finally, some remarks are added on the parameter-independent method [86], which is also widely used in the literature.

It is natural to require that

$$\lim_{\epsilon \to 0} R'' = R''(\epsilon \to 0)\,, \tag{E.1}$$

where $\lim_{\epsilon \to 0} R''$ means first calculating the rate with a finite ϵ and afterwards taking the limit $\epsilon \to 0$, while $R''(\epsilon \to 0)$ is computed with the δ function limit of the propagator from the beginning, as given in Eq. (D.14). In fact, if R'' is a well-defined function without poles and divergences, Eq. (E.1) holds true automatically. Since in the derivation of $R''(\epsilon \to 0)$, the formal divergence is rendered finite by the general replacement rule $2\pi\delta(0) = T$ with a well-defined physical quantity T as the interaction time of the process, the requirement (E.1) nontrivially determines the relation between the finite values of ϵ and T. This will be shown below.

Let us start from Eq. (D.3). Instead of taking ϵ to the limit, we perform the calculation directly by inserting the Volkov wave functions, carrying out all the integrations, and obtaining the rate $R'' = \frac{|S''_{fi}|^2}{T}$ with a finite ϵ. Notice that here T comes from the square of the δ function of the total energy-momentum conservation, independent of the treatment of the propagator, as shown in Eq. (D.13). Neglecting the terms with $n_1 \neq n_2$, as in the

treatment done in Eq. (D.14), we obtain

$$\begin{aligned}
R'' =&\frac{4m^4\alpha^2(2\pi)^6}{V^3q^0q'^0q_+^0q_-^0}\sum_N\delta(q+Nk-q'-q_--q_+)\\
&\sum_n\frac{\epsilon^2}{((q-q'+nk)^4+\epsilon^2)^2}|M^\mu(q,q'|n)M_\mu(q_+,q_-|N-n)|^2\\
=&\frac{4m^4\alpha^2(2\pi)^6}{V^3q^0q'^0q_+^0q_-^0}\sum_N\delta(q+Nk-q'-q_--q_+)\\
&\sum_n\int dx\delta(x-(q-q'+nk)^2)\frac{\epsilon^2}{(x^2+\epsilon^2)^2}\\
&\times|M^\mu(q,q'|n)M_\mu(q_+,q_-|N-n)|^2\\
\simeq&\frac{4m^4\alpha^2(2\pi)^6}{V^3q^0q'^0q_+^0q_-^0}\sum_N\delta(q+Nk-q'-q_--q_+)\\
&\sum_n\frac{1}{2|q^0-q'^0+nk^0|}\delta((q^0-q'^0+nk^0)-|\mathbf{q}+n\mathbf{k}-\mathbf{q}'|)\frac{\pi}{2\epsilon}\\
&\times|M^\mu(q,q'|n)M_\mu(q_+,q_-|N-n)|^2\,,
\end{aligned}\tag{E.2}$$

where the following approximation has been made for small ϵ

$$\begin{aligned}
\int dx\delta(x-(q-q'+nk)^2)\frac{\epsilon^2}{(x^2+\epsilon^2)^2}\simeq&\delta((q-q'+nk)^2)\int dx\frac{\epsilon^2}{(x^2+\epsilon^2)^2}\\
\simeq&\delta((q-q'+nk)^2)\frac{\pi}{2\epsilon}\,.
\end{aligned}\tag{E.3}$$

Due to the requirement (E.1), for ϵ small enough, Eq. (D.14) and Eq. (E.2) should yield the same result. Comparing the two equations term by term, this requires

$$\frac{m^4\alpha^2(2\pi)^8}{4V^3q^0q'^0q_+^0q_-^0}\frac{1}{(q^0+nk^0-q'^0)^2}\frac{T}{2\pi}=\frac{4m^4\alpha^2(2\pi)^6}{V^3q^0q'^0q_+^0q_-^0}\frac{1}{2|q^0-q'^0+nk^0|}\frac{\pi}{2\epsilon}\,,$$

which leads to the relation

$$\epsilon=\frac{2|q^0-q'^0+nk^0|}{T}=\frac{2(q^0-q'^0+nk^0)}{T}\,,\tag{E.4}$$

with the energy of the intermediate photon $k'^0=q^0-q'^0+nk^0>0$ fulfilled by the resonance condition (C.5). This means that the propagator is regularized as

$$\frac{1}{(q-q'+nk)^2+i\epsilon}=\frac{1}{(q-q'+nk)^2+\frac{2i(q^0-q'^0+nk^0)}{T}}=\frac{1}{(q-q'+nk+i\frac{1}{T}\hat{n})^2}\,,\tag{E.5}$$

with a time-like unit vector $\hat{n}=(1,0,0,0)$. The result, with an imaginary modification of the energy, is consistent with the Breit-Wigner method (see Eq. (3.43)). The derivations shown here have a further advantage of revealing in a rigorous way the relation between our method and the cascade theory, as well as between the regulator and the characteristic time of the process. This facilitates the generalization of this method to more complicated cases, where there are competing mechanisms in determining the interaction time.

Evaluating the two parts

The two parts in the rate regarding the two terms in the propagator will be treated in the following. It is found that both have comparable contributions. This conclusion holds true generally under only the requirement that ϵ should be small. Therefore, it does not support the interpretation that the two parts come from the contributions of the direct and the two-step process separately. We emphasize that, in our thesis, the two-step process is defined as the process with the parameters set to fulfill the resonance condition (C.5), and the direct process is that with the resonance condition not being satisfied.

The general form of the rate has been given in Eq. (D.8) and Eq. (D.9), where $\Lambda_{N,n}$ can be calculated as

$$\begin{aligned}\Lambda_{N,n} = &\int \frac{d^3\mathbf{q}'}{q'^0}\int \frac{d^3\mathbf{q}_+}{q_+^0}\int \frac{d^3\mathbf{q}_-}{q_-^0}\int dx\delta(x-(q-q'+nk)^2)\\ &\times\delta(q+Nk-q'-q_+-q_-)F_{N,n}(q,k,q',q_+,q_-)\\ &\times(\frac{x^2}{(x^2+\epsilon^2)^2}+\frac{\epsilon^2}{(x^2+\epsilon^2)^2})\,,\end{aligned} \tag{E.6}$$

with $F_{N,n}(q,k,q',q_+,q_-)$ being a real continuous function without poles. The five δ functions can be used to reduce the ten integrals to five. Keeping the integration over x, and letting Φ denote the other four remaining integral variables, Eq. (E.6) can be written as

$$\begin{aligned}\Lambda_{N,n} &= \int dx\int d^4\Phi\, F_{N,n}(x,\Phi)(\frac{x^2}{(x^2+\epsilon^2)^2}+\frac{\epsilon^2}{(x^2+\epsilon^2)^2})\\ &= \int dx\widetilde{F}_{N,n}(x)(\frac{x^2}{(x^2+\epsilon^2)^2}+\frac{\epsilon^2}{(x^2+\epsilon^2)^2})\,,\end{aligned} \tag{E.7}$$

where $\widetilde{F}_{N,n}(x)=\int d^4\Phi\, F_{N,n}(x,\Phi)$ is a continuous function of x. The integration is mainly determined in a small vicinity around $x=0$, if ϵ is small. Therefore, due to the mean value theorem,

$$\Lambda_{N,n}\cong\widetilde{F}_{N,n}(0)\int dx(\frac{x^2}{(x^2+\epsilon^2)^2}+\frac{\epsilon^2}{(x^2+\epsilon^2)^2})\,. \tag{E.8}$$

The integration in Eq. (E.8) yields

$$K_1(l)=\int_{-l\epsilon}^{l\epsilon}dx\frac{x^2}{(x^2+\epsilon^2)^2}=\frac{-l+(1+l^2)\arctan(l)}{\epsilon(1+l^2)}\,, \tag{E.9a}$$

$$K_2(l)=\int_{-l\epsilon}^{l\epsilon}dx\frac{\epsilon^2}{(x^2+\epsilon^2)^2}=\frac{l+(1+l^2)\arctan(l)}{\epsilon(1+l^2)}\,. \tag{E.9b}$$

$K_1(l)$, $K_2(l)$ are both monotonically increasing functions, and converge quickly to $\frac{\pi}{2\epsilon}=K_1(\infty)=K_2(\infty)$. For example, when $l=50$, we obtain

$$\frac{K_1(l)}{K_1(\infty)}=\frac{2}{\pi}(\arctan(l)-\frac{1}{1/l+l})>0.97\,, \tag{E.10a}$$

$$\frac{K_2(l)}{K_2(\infty)}=\frac{2}{\pi}(\arctan(l)+\frac{1}{1/l+l})>0.99\,. \tag{E.10b}$$

Therefore,

$$\Lambda_{N,n} \cong \frac{\pi}{\epsilon}\widetilde{F}_{N,n}(0)\,. \tag{E.11}$$

For the relation (E.11) to be true, the only requirement is that the ϵ should be small, so that the integration can be determined within a range $x \in [-L\epsilon, L\epsilon]$ with $K_{1,2}(L) \approx \frac{\pi}{2\epsilon}$, while $L\epsilon \ll 1$ still holds.

Physically speaking, since the intermediate photon has an energy uncertainty $\sim \frac{1}{T}$ due to the finite interaction time, it is impossible to distinguish completely the contribution of the on-shell photon from that of the off-shell photon in a resonance problem. The crucial conclusion is that, if Eq. (D.7), which allows a clear interpretation as a cascade process, is used for the calculation for small ϵ with the $\epsilon - T$ relation (E.4), the final result should be multiplied by a factor of 2, to take into account the contribution related to the other half of the propagator.

The Breit-Wigner method is not an ab-initio treatment, and a parameter should be introduced in to regulate the divergence. By requiring that the total rate should be proportional to the characteristic time of the process within which it takes place, as indicated also from the cascade theory, we have found the explicit form of the correspondence between the regulator and the characteristic time. This may add some insights into the understanding of the process. For example, as discussed in section 3.3.1, in the SLAC experiment, the characteristic time is the duration the electron spent in the laser pulse. But if a smaller impact angle is applied, so that the duration is longer than the lifetime of the electron via laser-dressed spontaneous decay, then the characteristic time is the reciprocal of the rate of the laser-dressed spontaneous radiation. Since this rate is dependent on the laser intensity as $\Gamma_{\text{decay}} \sim \alpha\xi^2\omega$, it would alter the ξ dependence of the rate found for the case with an intensity-independent characteristic time. Therefore, in a resonance problem, the experimental conditions can have unconventional influences over the results.

Remarks on an alternative approach

The parameter-independent procedure is another widely used method in dealing with resonance divergences. It is given in the literature [86] that

$$R = \lim_{\epsilon\to 0}\int dx \frac{f(x)}{|x+i\epsilon|^2} = \int dx f(x)(PV\frac{1}{x})^2 + \pi^2 f(0)\delta(0)\,, \tag{E.12}$$

with the relation below applied

$$\frac{1}{x} = \lim_{\epsilon\to 0}\frac{1}{x+i\epsilon} = \lim_{\epsilon\to 0}(\frac{x}{x^2+\epsilon^2} + \frac{-i\epsilon}{x^2+\epsilon^2}) = PV\frac{1}{x} - i\pi\delta(x)\,, \tag{E.13}$$

where PV denotes the principal value integral. In our problem, comparing with Eq. (D.8) and Eq. (E.7), $x = k'^2$ and the concrete form of the positive function $f(x)$ reads

$$f(x) = \frac{\alpha^2 m^4}{(2\pi)^3 q^0}\sum_N\sum_n \widetilde{F}_{N,n}(x)\,. \tag{E.14}$$

In the parameter-independent approach, $\delta(0)$ represents the divergent part, and can be rendered finite by a certain replacement procedure. Comparing with Eq. (E.11), it can be found that if the replacement is performed by $\delta(0) = \frac{1}{\pi\epsilon}$, the value of $\pi^2 f(0)\delta(0)$ gives the same total rate as that obtained from our method. Notice that the dimension of the replacement is $[T^2]$, since x as well as ϵ in Eq. (E.12) has a dimension of $[T^{-2}]$.

When Volkov states in the presence of a laser pulse of finite duration are used, the $\delta(0)$ part becomes finite automatically, without the need for replacement rules. Mathematically more rigorous at first sight, this method ignores, however, physical properties arising from the finite lifetime of Volkov states due to laser-dressed spontaneous radiation, for example, or vacuum polarization effects.

The conventional evaluation of the part with the square of the principal value is a bit subtle. According to [86], it is evaluated as

$$
\begin{aligned}
&\int dx f(x)(PV\frac{1}{x})^2 \\
=&\lim_{h\to 0}\int dx f(x)(PV\frac{1}{x}PV\frac{1}{x+h}) \qquad (*)\\
=&\lim_{h\to 0}\lim_{\epsilon_1\to 0}\lim_{\epsilon_2\to 0}\int dx f(x)(\frac{x}{x^2+\epsilon_1^2}\frac{x+h}{(x+h)^2+\epsilon_2^2}) \\
=&\lim_{h\to 0}\lim_{\epsilon_1\to 0}\lim_{\epsilon_2\to 0}\int dx f(x)(\frac{1}{h}(\frac{x}{x^2+\epsilon_1^2}-\frac{x+h}{(x+h)^2+\epsilon_2^2})+\frac{\epsilon_1^2(x+h)-\epsilon_2^2 x}{h(x^2+\epsilon_1^2)((x+h)^2+\epsilon_2^2)}) \\
=&\lim_{h\to 0}\lim_{\epsilon_1\to 0}\lim_{\epsilon_2\to 0}\int dx\frac{1}{h}(\frac{xf(x)}{x^2+\epsilon_1^2}-\frac{xf(x-h)}{x^2+\epsilon_2^2})+\lim_{h\to 0}\lim_{\epsilon_1\to 0}\lim_{\epsilon_2\to 0}\int dx f(x)\frac{\epsilon_1^2(x+h)-\epsilon_2^2 x}{h(x^2+\epsilon_1^2)((x+h)^2+\epsilon_2^2)} \\
=&\lim_{h\to 0}\lim_{\epsilon_1\to 0}\lim_{\epsilon_2\to 0}\int dx\frac{1}{h}(\frac{xf(x)}{x^2+\epsilon_2^2}-\frac{xf(x-h)}{x^2+\epsilon_2^2})+\lim_{h\to 0}\lim_{\epsilon_1\to 0}\lim_{\epsilon_2\to 0}\int dx\frac{xf(x)}{h}\frac{\epsilon_2^2-\epsilon_1^2}{(x^2+\epsilon_1^2)(x^2+\epsilon_2^2)} \\
=&\lim_{h\to 0} PV\int dx\frac{1}{h}(\frac{f(x)}{x}-\frac{f(x-h)}{x}) \\
=&PV\int dx\frac{\frac{d}{dx}f(x)}{x} \\
=&PV\int dx\frac{\frac{d}{dx}(f(x)-f(0))}{x} \\
=&PV\int dx\frac{f(x)-f(0)}{x^2}\,. \qquad (E.15)
\end{aligned}
$$

In this way, the last principal value integral is finite in a parameter-independent manner. However, a subtlety arises in this transformation. Since $f(x)$ is positive definite, the initial integrand as well as the result of the integration should always be positive definite, but in the last expression, the integrand and the integration are not positive definite anymore. Suppose that $f(x)$ is a well-defined analytical function with a finite maximum at $x = 0$, the integral turns out to be negative, and we cannot refer to it as a rate. The problem may come from the altering of the order of doing the limitings in the step marked by $(*)$. For the $(*)$ expression to be positive definite, the limiting of h should be taken ahead of the principal value integration, otherwise for any finite h, the integration in the region

$x \in (-h, 0)$ is negative. This region does not become immaterial with $h \to 0$, since it is in the vicinity of the pole. On the other hand, if the limiting order is changed to be $\lim_{\epsilon_1 \to 0} \lim_{\epsilon_2 \to 0} \lim_{h \to 0}$, then the second terms in the fourth and fifth lines in Eq. (E.15) contain ill-defined integrals.

In calculations using the parameter-independent method, the principal value integration by using Eq. (E.15) gives a small number compared with that from the divergent part in the resonance case. If the replacement of $\delta(0) = \frac{1}{\pi\epsilon}$ is applied as mentioned before, the results from this method and ours are approximately the same.

Appendix F

Method of discrete basis elements

Noting that R_s in Eq. (4.49) is a well-behaved continuous function without poles, it is possible to apply the basis method. That is to divide the parameter space into a set of discrete elements, $\Delta_{i,j,k} = O(E_i, \theta_j, E_k)$, $i,\ j,\ k = 1, 2, 3, \cdots$, with $O(x, y, z)$ designating a neighborhood of (x, y, z), and obtain the basis set of rates

$$R_{i,j,k} = R_s(E_i, \theta_j, E_k), \qquad i,\ j,\ k, = 1, 2, 3, \ldots . \tag{F.1}$$

For every parameter combination $(E^+, E^-, \theta^-, E_p, \theta, \phi)$ encountered in the 6-dimensional integration of Eq. (4.49), there is one corresponding parameter combination $(E_b^-, \theta_b^r, E_{p,b})$ via Eqs. (4.52, 4.53, 4.54). If $(E_b^-, \theta_b^r, E_{p,b}) \in \Delta_{i,j,k}$, the rate is evaluated by using Eq. (4.56), that is

$$R_s(E^+, E^-, \theta^-, E_p, \theta, \phi) \to \frac{m E_b^- E_{p,b}}{E^+ E^- E_p} R_{i,j,k} \,. \tag{F.2}$$

Since the rate for definite particle energies is independent of the temperature, the same basis set can be applied in cases of different temperatures.

The size of the basis set required, however, strongly depends on the temperature. We introduce a cut-off energy E^c defined as the minimum energy satisfying

$$\frac{\rho_t^c(T_p)}{\rho_t(T_p)} \simeq \frac{2 g_F \int_m^{E^c} \frac{d^3p}{(2\pi)^3} n_F(E, T_p)}{0.37 T_p^3} > 0.97 \sim 0.9^{\frac{1}{3}} \,. \tag{F.3}$$

Then $E^c(T_p)$ can be obtained numerically for any specific temperature T_p, and an approximate relation is found

$$E^c \sim 6\, T_p \,, \qquad \text{for } T_p > m \,. \tag{F.4}$$

If we consider a head-on collision of a positron and an electron, both taking the energy E^c, then in the rest frame of the positron, the electron's energy is

$$E^{c'} \simeq 2\gamma^c E^c \sim \frac{2(E^c)^2}{m} \sim \frac{80 T_p^2}{m} \,. \tag{F.5}$$

Therefore, the smallest basis set $\{R_{i,j,k}|\ i=1,\cdots,N_1;\ j=1,\cdots,N_2;\ k=1,\cdots,N_3\}$ should fulfill the relation $N_1=N_3=\frac{E^{c'}}{dE}$, with dE denoting the energy interval of the parameter space element. The total size becomes

$$N_1N_2N_3\sim\frac{7\times10^3T_p^4}{m^2dE^2}N_2\,. \tag{F.6}$$

Due to the symmetry of the two electrons, the equality $R_{i,j,k}=R_{k,j,i}$ holds, which indicates that one half of the basis set with elements $\{R_{i,j,k}|E_i\geq E_k\}$ contains the full information of the whole basis set. Besides, this symmetry can also be used in Eq. (4.49), for example, the integration of E_p can be performed with the boundary $\int_m^{E^-}dE_p$, and the final result should be multiplied by a factor 2 since the two electrons are distinguished. Although the size of the basis set can be reduced to almost half, it is still large and increases with a fourth order dependence on the temperature.

Nevertheless, we found that for large momenta, the evaluation of the rate has a trend to merge. More precisely, as shown in Fig. F.1, for a given θ and $E_l\geq E_s>2\,\mathrm{MeV}$, $R_s(E_l,\theta,E_s)$ has a very weak dependence on E_l, and decreases with the increase of E_s in a way that fits very well to

$$R_s\sim\frac{a}{E_s^d}\,, \tag{F.7}$$

where the fitting parameters a and d are functions of θ. The values of a and d are listed in Table F.1. It is found that, the larger θ is, the larger a is, while the smaller d is. It indicates that R_s not only increases monotonically with the increase of θ, but also decreases less rapidly with E_s when θ is larger. These features are manifested in Fig. F.2.

Table F.1: Fitting parameters for different θ.

θ	0°	15°	30°	45°	60°	75°	90°	105°	120°	135°	150°	165°	180°
$a(\times10^{16})$	39.6	40.5	43.9	53.5	70.2	90.4	112	135	158	180	198	208	211
d	2.28	2.25	2.13	1.83	1.40	1.02	0.75	0.58	0.48	0.41	0.37	0.36	0.36

The basis set used in our calculation is

$$\begin{aligned}\{R_{i,j,k},\, i\geq k|R_{i,j,k}=R_s(E_l,\,\theta,E_s),\ E_l=m+(i-1)dE,\ \theta=(j-1)d\theta,\\ E_s=m+(k-1)dE,\ i=1,\cdots,N_1;\ j=1,\cdots,N_2;\ k=1,\cdots,i\}\,,\end{aligned} \tag{F.8}$$

with $dE=0.2\,\mathrm{MeV}$, $d\theta=15^\circ$, $N_1=\frac{8\,\mathrm{MeV}}{dE}+1=41$, $N_2=\frac{180^\circ}{d\theta}+1=13$, and the size is $\frac{N_1(N_1+1)N_2}{2}=10660$. To calculate $R_s(E_l,\theta,E_s)$ with $E_l\geq8.511\,\mathrm{MeV}\geq E_s$, we resort to $R_s(E_l,\theta,E_s)\to R_{N_1,j,k}$, where $j=\mathrm{int}(\frac{\theta}{d\theta})+1$ and $k=\mathrm{int}(\frac{E_s-m}{dE})+1$, with $\mathrm{int}(x)$ giving the closest integer to x. If $E_l\geq E_s>8.511\,\mathrm{MeV}$, the fitting functions of Eq. (F.7) are applied.

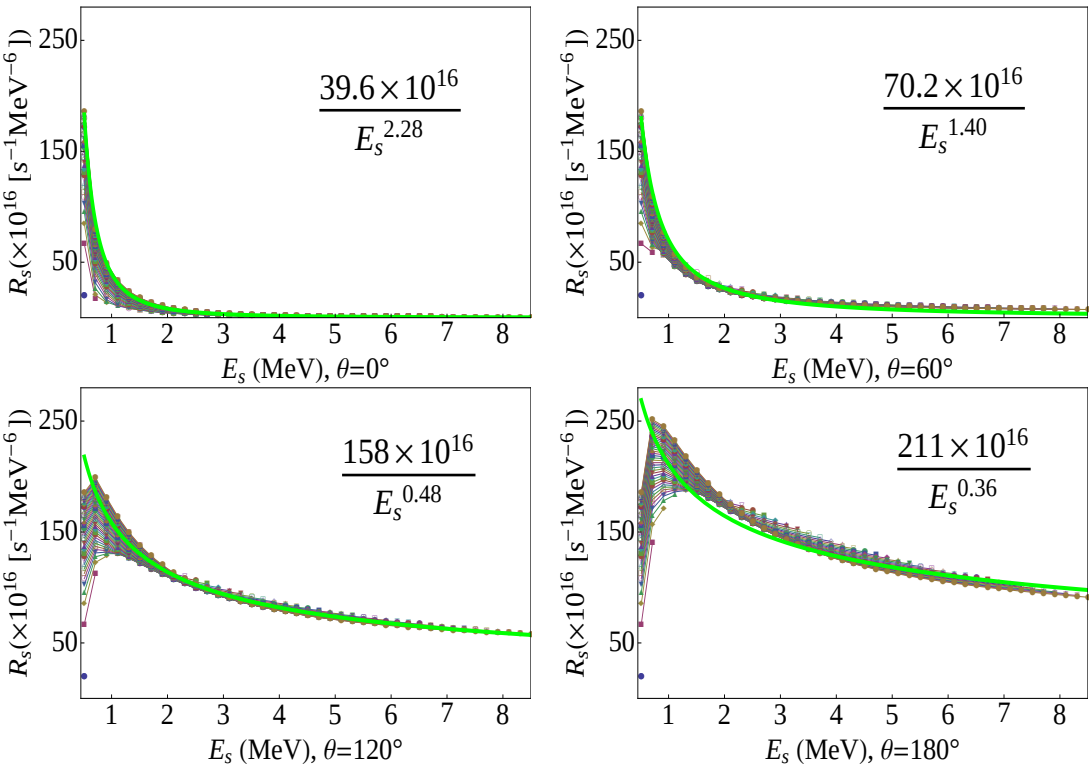

Figure F.1: The basis set $\{R_{i,j,k},\, i \geq k | R_{i,j,k} = R_s(E_l,\, \theta,\, E_s)\}$ defined as in (F.8) is displayed for fixed j (i. e. for fixed θ). Each thin line connects the dots, which have x coordinate as $E_s = m + (k-1)dE$ with various k, and y coordinate as $R_{i,j,k} = R_s(E_l,\, \theta,\, E_s)$ of fixed i (E_l) and j (θ). The formulas in the form of $R_s = aE_s^{-d}$ are the fitting functions for each angle, plotted as the thick green lines. The unit of R_s is taken to be $R_s = \frac{R[s^{-1}]}{\rho^2[MeV^6]}$.

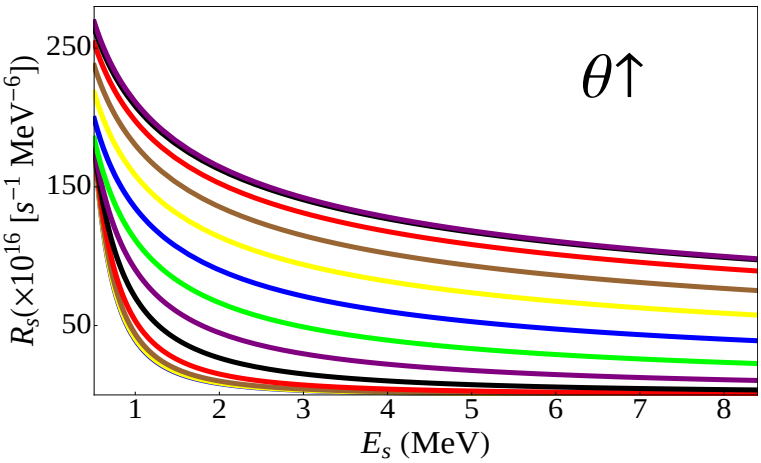

Figure F.2: The lines from the bottom to the top represents the fitting functions in steps of 15°, all in the form of $f(E_s) = aE_s^{-d}$ with angle-dependent parameters a and d given in Table F.1, as angles increase from 0° to 180°.

Bibliography

[1] E. Schrödinger, Annalen der Physik (Leipzig) **79**, 361 (1926).

[2] W. Heisenberg, Z. Phys. **43**, 172 (1927).

[3] P. A. M. Dirac, Proc. R. Soc. Lond. A **117**, 610 (1928).

[4] W. E. Lamb Jr. and R. C. Retherford, Phys. Rev. **72**, 241 (1947).

[5] G. Gabrielse, D. Hanneke, T. Kinoshita, M. Nio, and B. Odom, Phys. Rev. Lett. **97**, 030802 (2006).

[6] F. Sauter, Z. Phys. **69**, 742 (1931).

[7] J. Schwinger, Phys. Rev. **82**, 664 (1951).

[8] O. Klein, Z. Phys. **53**, 157-165 (1929).

[9] J. Esberg *et al.*, Phys. Rev. D **82**, 072002 (2010).

[10] D. Strickland and G. Mourou, Opt. Commun. **56**, 219 (1985).

[11] T. Brabec and F. Krausz, Rev. Mod. Phys. **72**, 545 (2000).

[12] N. Bloembergen, Rev. Mod. Phys. **71**, S283 (1999).

[13] F. Krausz and M. Ivanov, Rev. Mod. Phys. **81**, 163 (2009).

[14] G. R Mocken and C. H. Keitel, J. Phys. B **37**, L275 (2004); S. Chelkowski, A. D. Bandrauk, and P. B. Corkum, Phys. Rev. Lett. **93**, 083602 (2004); T. J. Bürvenich, J. Evers, and C. H. Keitel, Phys. Rev. Lett. **96**, 142501 (2006); A. Shahbaz *et al.*, Nucl. Phys. A **821**, 106 (2009); T. Ditmire *et al.*, Nature (London) **386**, 54 (1997); K. W. D. Ledingham, P. McKenna, and R. P. Singhal, Science **300**, 1107 (2003).

[15] C. Bula *et al.*, Phys. Rev. Lett. **76**, 3116 (1996).

[16] V. Yanovsky *et al.*, Opt. Express **16**, 2109 (2008); for current information, see http://www.engin.umich.edu/research/cuos/.

[17] See http://www.hiper-laser.org/ for current information.

[18] See the proposal on the Extreme Light Infrastructure (ELI) available on http://www.eli-laser.eu.

[19] For current information see http://xfel.desy.de.

[20] L. Young *et al.*, Nature **466**, 56 (2010).

[21] F. Grüner *et al.*, Appl. Phys. B **86**, 431 (2007).

[22] H. R. Reiss, J. Math. Phys. **3**, 59 (1962); Phys. Rev. Lett. **26**, 1072 (1971).

[23] A. I. Nikishov and V. I. Ritus, Zh. Eksp. Teor. Fiz. **46**, 776 (1964) [Sov. Phys. JETP **19**, 529 (1964)].

[24] V. P. Yakovlev, Zh. Eksp. Teor. Fiz. **49**, 318 (1965) [Sov. Phys. JETP **22**, 223 (1966)].

[25] E. Brezin and C. Itzykson, Phys. Rev. D **2**, 1191 (1970).

[26] V. S. Popov, Pisma Zh. Eksp. Teor. Fiz. **13**, 261 (1971) [JETP Lett. **13**, 185 (1971)].

[27] D. Burke *et al.*, Phys. Rev. Lett. **79**, 1626 (1997); C. Bamber *et al.*, Phys. Rev. D **60**, 092004 (1999).

[28] G. Breit and J. A. Wheeler, Phys. Rev. **46**, 1087 (1934).

[29] H. A. Bethe and W. Heitler, Proc. Roy. Soc. London A **146**, 83 (1934).

[30] H. Chen *et al.*, Phys. Rev. Lett. **102**, 105001 (2009); H. Chen *et al.*, Phys. Rev. Lett. **105**, 015003 (2010); see also C. Müller and C. H. Keitel, Nature Photon. **3**, 245 (2009).

[31] B. Shen and J. Meyer-ter-Vehn, Phys. Rev. E **65**, 016405 (2001).

[32] M. H. Thoma, Rev. Mod. Phys. **81**, 959 (2009).

[33] J. Estrada, T. Roach, J. N. Tan, P. Yesley, and G. Gabrielse, Phys. Rev. Lett. **84**, 859 (2000); C. M. Surko and R. G. Greaves, Phys. Plasmas **11**, 2333 (2004); L. V. Jørgensen *et al.*, Phys. Rev. Lett. **95**, 025002 (2005); P. Perez and A. Rosowsky, Nucl. Instrum. Meth. Phys. Res. A **532**, 523 (2004); S. C. Wilks *et al.*, Astroph. Space Sci. **298**, 347 (2005).

[34] D. B. Cassidy *et al.*, Phys. Rev. Lett. **95**, 195006 (2005); D. B. Cassidy and A. P. Mills Jr., Nature **449**, 195 (2007); D. B. Cassidy and A. P. Mills Jr., Phys. Rev. Lett. **100**, 013401 (2008).

[35] H. Kang *et al.*, Phys. Rev. Lett. **104**, 203001 (2010).

[36] C. Cohen-Tannoudji, *Atoms in Electromagnetic Fields* (World Scientific, Singapore, 1994).

[37] D. M. Volkov, Z. Phys. **94**, 250 (1935).

[38] L. S. Brown and T. W. B. Kibble, Phys. Rev. **133**, A705 (1964).

[39] W. H. Furry, Phys. Rev. **81**, 115 (1951).

[40] V. A. Lyulka, Zh. Eksp. Teor. Fiz. **67**, 1638 (1974) [Sov. Phys. JETP **40**, 815 (1974)].

[41] J. Bös, W. Brock, H. Mitter, and Th. Schott, J. Phys. A **12**, 2573 (1979).

[42] V. P. Oleinik, Zh. Eksp. Teor. Fiz. **52**, 1049 (1967) [Sov. Phys. JETP **25**, 697 (1967)].

[43] R. V. Karapetyan and M. V. Fedorov, **75**, 816 (1978) [Sov. Phys. JETP **48**, 412 (1978)].

[44] E. Lötstedt, U. D. Jentschura, and C. H. Keitel, Phys. Rev. Lett. **98**, 043002 (2007).

[45] V. I. Ritus, Trudy FIAN **111**, 5 (1979) [J. Rus. Laser Res. **6**, 497 (1985)].

[46] C. Müller, K. Z. Hatsagortsyan, and C. H. Keitel, Phys. Rev. D **74**, 074017 (2006).

[47] C. Müller, K. Z. Hatsagortsyan, and C. H. Keitel, Phys. Rev. A **78**, 033408 (2008).

[48] G. Dattoli *et al.*, J. Math. Anal. App. **184**, 201 (1994).

[49] J. Gao, F. Shen, and J. G. Eden, Phys. Rev. A **61**, 043812 (2000).

[50] L. Gao, X. Li, P. Fu, R. R. Freeman, and D. S. Guo, Phys. Rev. A **61**, 063407 (2000).

[51] H. Hu and J. Yuan, Phys. Rev. A **78**, 063826 (2008).

[52] M. E. Peskin and D. V. Schroeder, *An Introduction to Quantum Field Theory* (World Publishing Corp., Beijing, 2006).

[53] V. I. Ritus, Zh. Eksp. Teor. Fiz. **57**, 2176 (1969) [Sov. Phys. JETP **30**, 1181 (1970)].

[54] N. B. Narozhny, Phys. Rev. D **20**, 1313 (1979).

[55] L. N. Ivanov and T. V. Zueva, Physica Scripta. **43**, 374 (1991).

[56] F. Hebenstreit and R. Alkofer, Phys. Rev. D **78**, 061701(R) (2008).

[57] K. J. Mork, Phys. Rev. **160**, 1065 (1967).

[58] A. Di Piazza, A. I. Milstein, and C. H. Keitel, Phys. Rev. A **76** (2007), 032103.

[59] C. Müller, A. B. Voitkiv, and N. Grün, Phys. Rev. Lett. **91**, 223601 (2003); Phys. Rev. A 67, 063407 (2003); Phys. Rev. A **70**, 023412 (2004).

[60] H. K. Avetissian, A. K. Avetissian, G. F. Mkrtchian, and Kh. V. Sedrakian, Nucl. Instrum. Methods Phys. Res. A **507**, 582 (2003).

[61] P. Sieczka, K. Krajewska, J. Z. Kaminski, P. Panek, and F. Ehlotzky, Phys. Rev. A **73**, 053409 (2006).

[62] A. I. Milstein, C. Müller, K. Z. Hatsagortsyan, U. D. Jentschura, and C. H. Keitel, Phys. Rev. A **73**, 062106 (2006).

[63] K. Krajewska and J. Z. Kaminski, Laser Phys. **18**, 185 (2008).

[64] M. Yu. Kuchiev and D. J. Robinson, Phys. Rev. A **76**, 012107 (2007).

[65] C. Müller, A. B. Voitkiv, and N. Grün, Phys. Rev. Lett. **91**, 223601 (2003).

[66] A. Di Piazza, E. Lötstedt, A. I. Milstein, and C. H. Keitel, Phys. Rev. Lett. **103**, 170403 (2009).

[67] S. J. Müller and C. Müller, Phys. Rev. D **80**, 053014 (2009).

[68] K. Krajewska and J. Z. Kaminski, Phys. Rev. A **82**, 013420 (2010).

[69] A. Ringwald, Phys. Lett. B **510**, 107 (2001).

[70] R. Alkofer, M. B. Hecht, C. D. Roberts, S. M. Schmidt, and D. V. Vinnik, Phys. Rev. Lett. **87**, 193902 (2001).

[71] N. B. Narozhny, S. S. Bulanov, V. D. Mur, and V. S. Popov, JETP Lett. **80**, 382 (2004).

[72] A. Bell and J. Kirk, Phys. Rev. Lett. **101**, 200403 (2008).

[73] F. Hebenstreit, R. Alkofer, G. V. Dunne, and H. Gies, Phys. Rev. Lett. **102**, 150404 (2009).

[74] T. Cheng, Q. Su, and R. Grobe, Europhys. Lett. **86**, 13001 (2009).

[75] M. Yu. Kuchiev, Phys. Rev. Lett. **99**, 130404 (2007).

[76] T.-O. Müller and C. Müller, Phys. Lett. B **696**, 201 (2011).

[77] C. Müller, C. Deneke, and C. H. Keitel, Phys. Rev. Lett. **101**, 060402 (2008).

[78] V. I. Ritus, Nucl. Phys. B **44**, 236 (1972).

[79] C. Bula and K. T. McDonald, E-144 Internal Note 970114 (1997) [see also arXiv:hep-ph/0004117].

[80] T. Koffas and A. C. Melissinos, E-144 Internal Note 980410 (1998) [see http://www.slac.stanford.edu/exp/ e144/notes/notes.html].

[81] W. Greiner and J. Reinhardt, *Quantum Electrodynamics* (Springer, Berlin-Heidelberg, 2009).

[82] S. P. Roshchupkin, Laser Phys. **6**, 837 (1996).

[83] O. I. Denisenko and S. P. Roshchupkin, Laser Phys. **9**, 1108 (1999).

[84] S. P. Roshchupkin, Sov. J. Nucl. Phys. **41**, 796 (1985).

[85] E. Lötstedt, *Laser-assisted second-order relativistic QED processes: Bremsstrahlung and pair creation modified by a strong electromagnetic wave field* (doctoral thesis, Ruperto-Carola University of Heidelberg, 2008).

[86] V. N. Baier, V. M. Katkov, and V. M. Strakhovenko, *Electromagnetic Processes at High Energies in Oriented Single Crystals* (World Scientific, Singapore, 1998).

[87] Y. I. Salamin, S. X. Hu, K. Z. Hatsagortsyan, and C. H. Keitel, Phys. Rep. **427**, 41 (2006); M. Marklund and P. K. Shukla, Rev. Mod. Phys. **78**, 591 (2006).

[88] H. R. Reiss, Eur. Phys. J. D **55**, 365 (2009).

[89] D. Charalambidis *et al.*, New J. Phys. **10**, 025018 (2008).

[90] W. P. Leemans *et al.*, Nature Phys. **2**, 696 (2006).

[91] In a similar setup, Thomson scattering was observed [H. Schwoerer *et al.*, Phys. Rev. Lett. **96**, 014802 (2006)].

[92] C. G. Fischer, M. H. Weber, C. L. Wang, S. P. McNeil, and K. G. Lynn, Phys. Rev. B **71**, 180102 (2005).

[93] W. E. Kauppila, E. G. Miller, H. F. M. Mohamed, K. Pipinos, T. S. Stein, and E. Surdutovich, Phys. Rev. Lett. **93**, 113401 (2004).

[94] J. Laverock, T. D. Haynes, M. A. Alam, and S. B. Dugdale, Phys. Rev. B **82**, 125127 (2010).

[95] K. W. Broda and W. R. Johnson, Phys. Rev. A **6**, 1693 (1972); P. M. Bergstrom, L. Kissel and R. H. Pratt, Phys. Rev. A **53**, 2865 (1996).

[96] J. K. Daugherty and R. W. Bussard, Astrophys. J. **238**, 296 (1980).

[97] A. M. Frolov and V. H. Smith Jr., Phys. Rev. A **49**, 3580 (1994).

[98] K. W. Chan and R. E. Lingenfelter, ApJ. **405**, 614 (1993).

[99] S. Weinberg, *Cosmology* (Oxford University Press, New York, 2008).

[100] Ya. N. Istomin and D. N. Sobyanin, Astron. Lett. **33**, 660 (2007).

[101] V. V. Usov, Phys. Rev. Lett. **80**, 230 (1998).

[102] E. Churazov, R. Sunyaev, S. Sazonov, M. Revnivtsev, and D. Varshalovich, Mon. Not. R. Astron. Soc. **357**, 1377 (2005).

[103] I. Kuznetsova, D. Habs, and J. Rafelski, Phys. Rev. D **78**, 014027 (2008).

[104] A. G. Aksenov, R. Ruffini, and G. V. Vereshchagin, Phys. Rev, Lett. **99**, 125003 (2007).

[105] K. G. Lynn, D. N. Lowy and I. K. Mackenzie, J. Phys. C: Solid St. Phys. **13**, 919 (1980).

[106] V. B. Berestetskii, E. M. Lifshitz, and L. P. Pitaevskii, *Relativistic Quantum Theory* (Pergamon Press, Oxford, 1971).

[107] M.-C. Chu and V. Pönisch, Phys. Rev. C **33**, 2222 (1986).

[108] S. I. Kryuchkov, J. Phys. B: At. Mol. Opt. Phys. **27**, L61 (1994).

[109] J. D. Bjorken and S. D. Drell, *Relativistic Quantum Mechanics* (McGraw-Hill, New York, 1964).

[110] P. Beiersdorfer, Annu. Rev. Astron. Astrophys. **41**, 343 (2003).

[111] For current information see http://loasis.lbl.gov/.

Acknowledgment

I would like to express my deepest thankfulness to Dr. Carsten Müller for his continuous guidance and support with never-ceasing passion and patience. Without his devotion to the subject, this thesis would have been impossible. I am deeply indebted to his positive influence on me in science as well as in my personal self-development. I also would like to express my sincere gratitude to Professor Christoph H. Keitel for letting me work in his friendly and inspiring group, and for his crucial suggestions, continuous encouragement and support during my PhD study. I owe special thanks to Professor Jianmin Yuan for helping me pursue my dream, and always being patient, understanding and supportive to me.

Thanks to Erik Lötstedt for stimulating discussions on the resonance problem and teaching me the program he worked out of generalized Bessel functions. Thanks to Antonino Di Piazza for informative discussions on the cascade theory and radiative corrections. Thanks to Heiko Bauke for drawing my attention to the Monte Carlo integration method. I appreciate the discussions with Sven Ahrens about his survey on laser facilities. Special regards to Sebastian Meuren, who is always ready to help, for reading my thesis and giving his very helpful suggestions.

I am grateful to my colleagues, who are all so nice and together provide the very active atmosphere of our group. From everyone I have got some help with respect to my work or social life, and just name a few here: Qurrat-ul-Ain, Ni Cui, Jicai Liu, Hector Castaneda, Sahra Müller, Felix Mackenroth, Benjamin Galow, Ben King, Octavian Postavaru, Markus Kohler, Anis Dadi, Sandra Schmid, Wen-Te Liao, Jacek Zatorski .... I would like to express my regards to Peter Brunner who was always very nice and patient when I asked him for help with the computer facilities. My gratitude also goes to the secretary ladies Vera Beyer and Sibel Babacan, whose kind help has made my life much more enjoyable.

I extend my acknowledgement to Professor Chi-Sing Lam for inspiring discussions and his sincere caring. Thanks to Professor Hsiang-Shun Chou for all his help and especially for teaching me Buddhist wisdom.

Last, but not least, my mother and father, whom I am deeply indebted to. Their love is so deep and their support is so important to me that I can never appreciate it enough. And thanks to my boyfriend Hao Zhang for his support and understanding. I feel very lucky to be with you.

Thank you!